Performance of the ATLAS Hadronic Endcap Calorimeter and The Physics of Electroweak Top Quark Production at ATLAS

by

Dugan Clive O'Neil

B.Sc., University of New Brunswick, 1994

M.Sc., University of Alberta, 1996

A Dissertation Submitted in Partial Fulfillment of the
Requirements for the Degree of

DOCTOR OF PHILOSOPHY

in the Department of Physics and Astronomy.

We accept this dissertation as conforming
to the required standard.

Dr. M Lefebvre, Supervisor (Department of Physics and Astronomy)

Dr. R. Keeler, Departmental Member (Department of Physics and Astronomy)

Dr. M. Roney, Departmental Member (Department of Physics and Astronomy)

Dr. C. Qian, Outside Member (Department of Chemistry)

Dr. G. Azuelos, External Examiner (Département de Physique, Université de Montréal)

Supervisor: Dr. M. Lefebvre

ABSTRACT

The Large Hadron Collider (LHC) and the ATLAS experiment are currently under construction with first collisions expected in 2005. The performance of detector components built to the final ATLAS design specifications are evaluated in particle beams. In addition, detailed simulations are performed to estimate the sensitivity of the ATLAS experiment to various physical processes. This thesis is divided into two parts, with contributions to each of these types of performance studies. First, an analysis of the performance of the Hadronic Endcap Calorimeter (HEC) yields a pion energy resolution of $\sigma/E = 78 \pm 2\%/\sqrt{E_o(\mathrm{GeV})} \oplus 5.0 \pm 0.3\%$ and an intrinsic electromagnetic to hadronic response ratio (e/h) of 1.6±0.1. Second, simulation studies have been performed to estimate the sensitivity of ATLAS to the measurement of $|V_{tb}|$ and the polarization of the top quark from electroweak top production. Estimates from three independent channels yield statistical precisions of 0.5%, 2.2% and 2.8% after three years of low luminosity ($10^{33}\mathrm{cm}^{-2}\mathrm{s}^{-1}$) LHC data-taking. The precision of the top polarization measurement from the highest rate electroweak channel is 1.6% after only 1 year of data-taking.

Examiners:

Dr. M. Lefebvre, Supervisor (Department of Physics and Astronomy)

Dr. R. Keeler, Departmental Member (Department of Physics and Astronomy)

Dr. M. Roney, Departmental Member (Department of Physics and Astronomy)

Dr. C. Qian, Outside Member (Department of Chemistry)

Dr. G. Azuelos, External Examiner (Département de Physique, Université de Montréal)

Contents

List of Figures

Acknowledgments

One of the things I enjoyed the most about my time as a Ph.D. student was the opportunity to collaborate with some great people.

Many have contributed to the testbeam results presented in this thesis. First and foremost I would like to thank my partner-in-crime Matt Dobbs. He's a good lad. We went through every step of the data analysis together from testbeam shifts to writing up the results as a note. Thanks to Kevin Graham for jumping in and backing up our data when we were in need. Thanks to my colleagues from Munich: Andrei Kiryunin, Horst Oberlack, Peter Schacht, Hasko Stenzel and Dieter Striegel for teaching me about calorimetry and how to run a testbeam. There are many more people to thank, in order to save some trees I will simply list some names: Rob Davis, Sepp Huber, Leonid Kurchaninov, Peter Loch, Andrei Minaenko and Pavol Strizenec.

In my single top analysis I worked most closely with Chip Brock and Beatriz González Piñeiro. Chip provided guidance and organized the work plan for the whole single top effort. Beatriz and I were in the trenches together exchanging phone calls and email to work out analysis details. Thanks goes out to John Parsons for his willingness to carefully proofread everything I wrote about single top. There are several patient people who helped me understand the theory behind single top: Greg Mahlon, Charles Picciotto, Tim Tait and Scott Willenbrock. Many others helped out and once again I will resort to simply listing their names: Marina Cobal-Grassmann, Ilias Efthymiopoulos, Kevin Graham, Rashid Mehdiyev, Pierre Savard and Sergei Slabospitsky.

Besides research, there are other things that need to be done to get a Ph.D.. Thanks to Richard Keeler for proofreading the thesis and for his detailed comments. Thanks to Ian Lawson for allowing me to steal his LaTeX style file and for various other TeX-assistance. Thanks to Laura Stumpf for being my study-buddy in all of my courses.

You may have noticed that I have not thanked Michel yet. That's because he was involved in absolutely everything and gets a paragraph all to himself. Michel Lefebvre has been my supervisor as an undergraduate summer student and as a Ph.D. student. He is a top-notch supervisor, a good friend and the reason I became a particle physicist. Thanks Michel.

Finally, I'd like to thank my wife Melanie. She doesn't get mad when I travel to CERN and leave her alone for weeks at a time. She doesn't get mad when I stay up late fixing the labelling on a figure in PAW. She bakes me cookies. She is my best bud.

To Bill and Sondra O'Neil, my mom and dad, thanks for everything...

Chapter 1

Introduction

The Standard Model embodies our current understanding of particles and their interactions. The next generation of hadron collider experiments planned at CERN[1] has the potential to make precision tests of the model and to search for signatures of physics beyond the Standard Model.

ATLAS is a general-purpose experiment scheduled to take data at the Large Hadron Collider (LHC) at CERN beginning in 2005. Work is currently underway to test the performance of detector components built to the final ATLAS design specifications. In addition, detailed simulations are performed to estimate the sensitivity of the ATLAS experiment to various physical processes of interest. This thesis is divided into two parts, presenting contributions to each of these types of performance studies.

The ATLAS detector has moved from the design phase to the construction phase. This presents the first opportunity to test detector components built to the final ATLAS design specifications. The ATLAS Hadronic Endcap Calorimeter (HEC) is a copper-liquid argon sampling calorimeter which will operate in the endcap regions of the ATLAS detector. Its design is unique in that it will be the first large-scale copper-liquid argon calorimeter. Also, as with many ATLAS sub-detectors, the large physical size of the calorimeter is, in itself, a unique feature of the device. Modules of the ATLAS HEC have been tested in particle beams at CERN in the summer

[1] CERN is the European Laboratory for Particle Physics in Geneva, Switzerland.

of 1998. A detailed analysis of the performance of these modules, including energy resolution, response and intrinsic e/h ratio, is presented herein.

ATLAS offers a unique opportunity to study the properties of the top quark. The LHC is often referred to as a "top factory" due to the high rate of top-pair production via the strong interaction anticipated at LHC energies. However, top production via the electroweak interaction promises to provide a probe of top properties not accessible through $t\bar{t}$ production. Specifically, it can be used to examine the properties of the W-t-b vertex by measuring the Cabibbo-Kobayashi-Maskawa (CKM) matrix element $|V_{tb}|$ and by measuring the polarization of the top quark. Simulation studies designed to estimate the sensitivity of the ATLAS experiment to $|V_{tb}|$ and top polarization have been performed and are described in this work. These are the first studies to consider the separation of individual electroweak top channels for the purposes of making independent measurements of $|V_{tb}|$ at the LHC. In particular, two significant sources of electroweak top production, which have been ignored at LHC energies in previous theoretical studies, are examined in detail.

The following sections of this introductory chapter present a brief overview of the Standard Model of particle physics as well as some basic features of the design of both ATLAS and the LHC. Details of either the Standard Model or detector design which are particularly relevant to parts of the analysis are expanded upon within the relevant chapters. Chapter 2 details the analysis of data from Hadronic Endcap Calorimeter beam tests performed in April 1998. Chapter 3 describes the sensitivity of the ATLAS experiment to the properties of top quarks produced in electroweak interaction. Finally, Chapter 4 presents some brief conclusions drawn from these studies.

1.1 The Standard Model

The current Standard Model of particle physics is built on the successes of three theories. The first is Quantum Electrodynamics (QED), the theory which describes the electromagnetic (EM) interaction. The success of QED has led to its use as a

model for theories describing the other interactions in the Standard Model. The next theory in the historical progression of the Standard Model is the theory of electroweak interactions first proposed by Glashow, Weinberg and Salam in the late 1960's and referred to as the Glashow-Weinberg-Salam model [1–3]. It incorporates the successful theory of QED and provides a description of the weak force in terms of the exchange of massive vector bosons. The fact that the masses of these vector bosons were successfully predicted from the theory before the particles were discovered is considered one of the major triumphs of the model. The third theory which makes up the Standard Model is Quantum Chromodynamics (QCD). This is the quantum field theory describing the interactions of quarks through the strong "colour" field.

The three theories which make up the Standard Model are each gauge theories. As such, each theory is invariant under local gauge transformations. This means that they are invariant under transformations applied independently at each space-time point. The fact that the Standard Model is composed of three gauge theories implies that it is built up from three gauge symmetries. These symmetries correspond to the three fundamental forces relevant to particle physics, namely the strong, the weak, and the electromagnetic force. The Standard Model gauge group is the product group $SU_c(3) \times SU_L(2) \times U_Y(1)$, with the $SU_c(3)$, $SU_L(2)$, and $U_Y(1)$ component groups being associated with the colour (c), weak, and hypercharge (Y) symmetries. The subscript L on the $SU_L(2)$ group indicates that the charged weak interaction involves coupling only to the chiral-left component of the fermion. Each force is mediated by one or more gauge bosons. The gauge bosons corresponding to the $SU_c(3)$ group (and hence the strong force) are the 8 massless gluons. The massive W^+, W^- and Z bosons carry the weak force and the massless photon carries the electromagnetic force. The combination of weak and electromagnetic forces is represented by the $SU_L(2) \times U_Y(1)$ groups. See Table 1.1 for a list of the known gauge bosons and their properties.

One of the most important unanswered questions of the Standard Model is the

Fermions (spin = 1/2)					
Leptons			Quarks		
Flavour	Charge	Mass (GeV)	Flavour	Charge	Mass (GeV)
ν_e	0	$<1.5\times10^{-8}$	u	+2/3	$(1.5\text{-}5)\times10^{-2}$
e^-	-1	5.11×10^{-4}	d	-1/3	$(3\text{-}9)\times10^{-2}$
ν_μ	0	$<1.9\times10^{-4}$	c	+2/3	1.1-1.4
μ^-	-1	0.11	s	-1/3	0.6-1.7
ν_τ	0	$<1.8\times10^{-2}$	t	+2/3	174.3±5.1
τ^-	-1	1.78	b	-1/3	4.1-4.4

Bosons (spin = 1)		
Flavour	Charge	Mass (GeV)
$W^\pm$	± 1	80.43±0.06
Z^0	0	91.188±0.007
γ	0	0
g	0	0

Table 1.1: Fermions and bosons of the Standard Model.

origin of mass. In gauge theories the gauge bosons must be massless. Therefore a mechanism is needed by which the massive vector bosons of the Standard Model ($W^\pm$ and Z^0) can acquire mass without violating local gauge invariance. It is widely believed that this problem can be solved by invoking the Higgs mechanism, which requires the onset of spontaneous symmetry breaking of the local $SU_L(2) \times U_Y(1)$ gauge symmetry, and provides a mass generation mechanism for both of the SU(2) weak gauge bosons and the observed massive quarks and leptons. It also predicts the existence of a massive scalar particle known as the Higgs boson. The best experimental verification of the existence of the Higgs mechanism would be the discovery of the Higgs boson. The discovery of this particle is one of the most important quests in particle physics and is one of the major reasons for the building of the Large Hadron Collider (LHC) to be discussed in the following sections.

According to the Standard Model, all matter is composed of spin - 1/2 particles known as fermions. The fermion content of the Standard Model is divided into quarks and leptons, each of which appear to come in three families. Leptons are fermions that interact under the weak, but not the strong interactions, while the

quarks are fermions that interact under the strong and electroweak interactions. Quarks interact via the strong interaction and they cannot be observed in isolation. Individual quarks will hadronize, through the creation of quark-antiquark pairs and the formation of relatively stable mesons such as pions. If the energy of the quark is high enough this hadronization will form a "jet" of particles. Jets are the observable objects associated with bare quarks (or gluons) in high energy physics experiments. The listing of fermions (leptons and quarks) is presented in Table 1.1.

The predictions of the Standard Model have been tested and verified to unprecedented precision by experiments at CERN, SLAC, Fermilab and other laboratories. However, there are several inadequacies of the Standard Model, such as: the origin of mass is unverified; the interactions are not unified; an explanation for why there are only three families does not exist; there are many (19) free parameters in the model[2] [4]; gravitation is absent from the model; and it provides no dark matter candidate.

1.2 The Large Hadron Collider (LHC)

The Large Hadron Collider (LHC) is a proton-proton collider being built at CERN with first physics data expected in 2005. The world's highest energy collider, it will use two counter-rotating 7 TeV beams to provide experiments with an unprecedented physics reach. This section reviews the physics goals and presents the important design parameters of the LHC.

1.2.1 Proton-Proton Collisions

Protons are composed of three valence quarks and a sea of virtual quarks and gluons. These constituents of the proton are known as partons. Each proton-proton collision may be viewed as an interaction of many partons. Each parton carries only a fraction of the total momentum of the proton. This means that, on average, the total energy

[2]There are 19 parameters if ν's are massless, they are: 3 coupling constants, 2 parameters of the Higgs potential, 9 fermion masses, 3 mixing angles and 1 phase in the Kobayashi-Maskawa matrix, and the vacuum parameter of QCD (θ_{QCD}).

available in an individual collision of partons is much less than the total momentum of the proton[3]. Therefore, in an individual proton-proton collision which yields the hard-scatter of two partons, significant energy is lost to the soft-scattering of the other partons. These soft-scatter particles are produced mainly in the forward regions of detectors (small angles from the beam axis) and are responsible for a higher radiation dose in these regions. Moreover, only a small fraction of events will actually contain a hard-scatter interaction. Events which contain only soft-scatter interactions are known as minimum bias events. Minimum bias events dominate the total LHC cross-section of $\sim$70 mb. A useful feature of minimum bias events is that charged particles from these events are distributed approximately uniformly in rapidity. Rapidity is described in Section 1.3.1.

Figure 1.1 shows a schematic picture of a proton-proton collision in which the proton is represented by three valence quarks. One of the quark-pairs undergoes a hard-scatter interaction while the other pairs are deflected at a small angle to the beam.

1.2.2 The Physics of the LHC

The LHC will provide a wide range of opportunities for physics studies. Precision measurements of Standard Model parameters, the search for the Higgs boson and the search for physics beyond the Standard Model are all part of the LHC experimental programme.

The most prominent physics question expected to be addressed by the LHC experiments relates to the nature of mass. In the Standard Model mass in generated via the Higgs mechanism, which will result in the production of a particle known as the Higgs boson. Direct searches have excluded a Higgs boson with mass below approximately 90 GeV [5] and theory requires that it not be heavier than $\sim$1 TeV making the entire allowed mass range accessible at the LHC. The most promising

[3]A valence quark carries, on average, approximately 15% of the proton momentum. The probability that a colliding parton will have a given fraction of the proton momentum can be calculated from its parton distribution function (pdf).

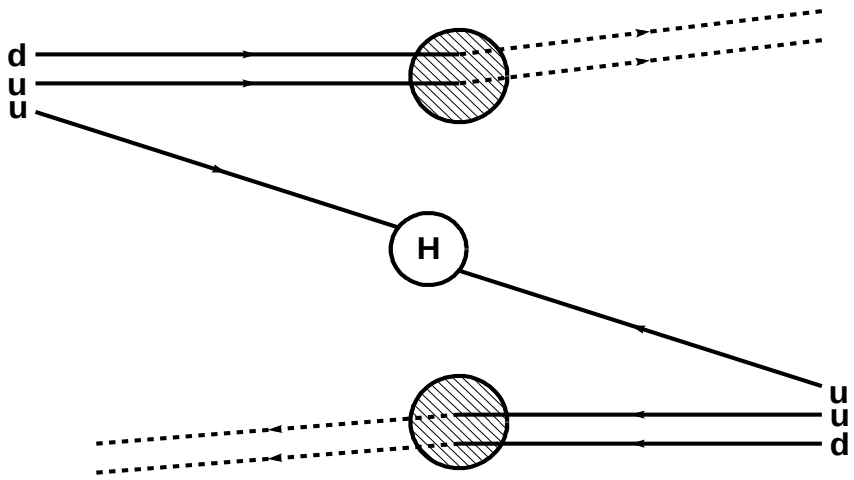

Figure 1.1: Schematic picture of a proton-proton collision. Solid lines represent incoming quarks, dashed lines are outgoing quarks, dark circles represent a vertex at which an interaction occurs. The H is the heavy particle (Higgs boson?) resulting from a hard-scatter interaction between two quarks. The circle surrounding the H hides the complex interaction which would be required to produced a Higgs boson. The other quarks (sometimes referred to as spectator quarks) are deflected through a small angle by their interactions.

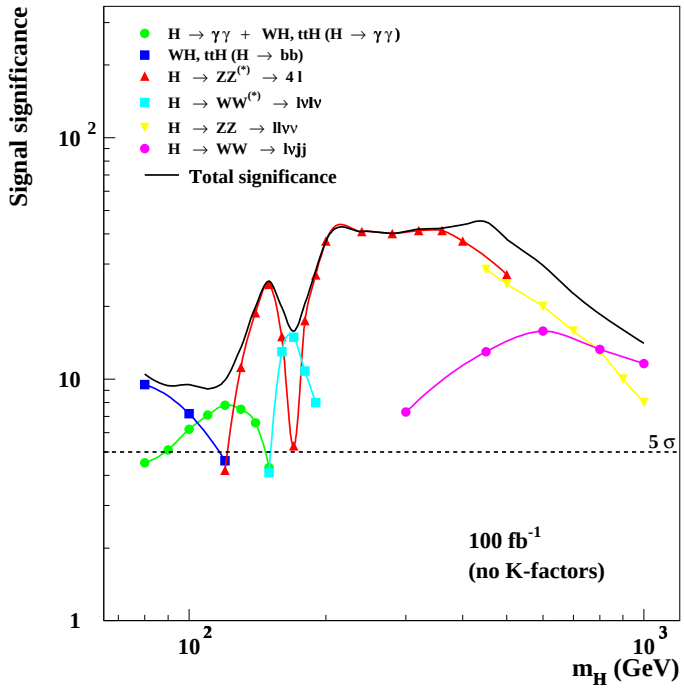

Figure 1.2: Statistical significance of the Higgs boson signal in various channels over the allowed mass range.

channel for Higgs discovery depends on the assumed mass of the Higgs. Figure 1.2 presents the discovery potential for the Higgs boson at the ATLAS detector as calculated from simulation.

Another major goal of the LHC is search for evidence of physics beyond the Standard Model. One of the best theoretically motivated sources of physics beyond the Standard Model is supersymmetry. If supersymmetry exists at the electroweak scale copious production of as yet unseen squarks and gluinos is expected at the LHC. Their decays would lead to a variety of signatures involving multi-jets, leptons, photons, heavy flavours and missing transverse energy (E_t^{miss})[4]. Assuming supersymmetry exists, the main challenge is not to discover it at the LHC, which should

[4]Since the protons collide along the z-axis of the detector, the vector sum of the momenta transverse to this axis should be zero when all particles produced in the collision are taken into account. This constraint can be used to deduce the transverse momentum of undetected particles in an event. This is called a measurement of missing transverse energy.

be straightforward, but rather to make a precision measurement of the properties of supersymmetric particles. In addition to supersymmetry it will also be possible to search for other indications of physics beyond the Standard Model such as technicolour, new gauge bosons, leptoquarks, right-handed neutrinos and monopoles.

The LHC has a significant potential for performing high-precision top quark measurements. The high rate of top quark production, 8 million $t\bar{t}$ pairs per year at "low" luminosity ($10^{33}cm^{-2}s^{-1}$), will allow precise measurements of the top mass and detailed studies of other top quark properties. The potential to study the W-t-b vertex through electroweak top production is presented in more detail in Chapter 3.

Though it is not designed as a dedicated b-factory, the LHC will nonetheless produce 10^{12} $b\bar{b}$ pairs per year at low luminosity. The available statistics will be limited only by the rate at which data can be recorded. This allows a very wide programme of b-quark physics to be performed at the LHC, both at the planned b-physics experiment (LHC-B) and at the general-purpose experiments (ATLAS and CMS). The topics of study envisioned for the LHC include the measurement of CP-violation, of B_S^0 mixing and rare decays.

The LHC will be an important source of gauge boson production. Three hundred million single W events are expected per year, leading to a statistical error on the W mass measurement of only 2 MeV. One of the challenges of the LHC experiments will be to understand sources of systematic error well enough to make a W mass measurement with a total precision less than 20 MeV. The large rate of gauge boson pair production at the LHC also allows critical tests of the triple gauge-boson couplings to be performed.

A large variety of QCD processes can be studied at the LHC. These studies will be performed in a new energy regime with high statistical precision. Precise constraints on the parton distribution functions, the search for evidence of quark compositeness, jet and photon physics are a few of the areas in which new results are expected.

A more complete description of the physics programme of an LHC experiment

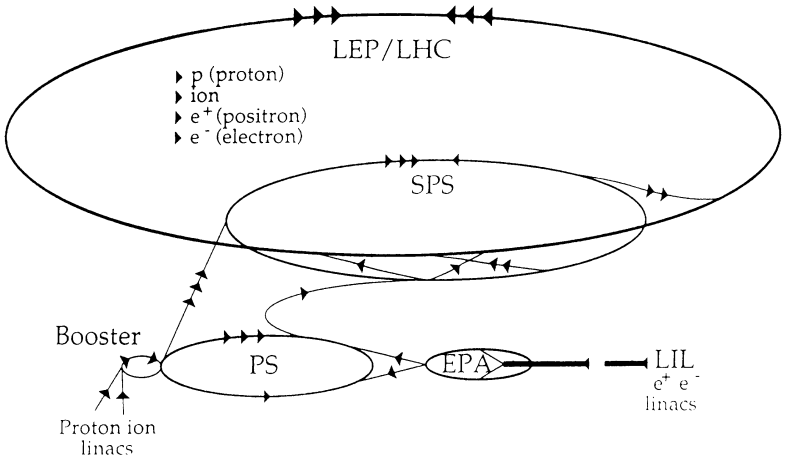

Figure 1.3: The LHC injector complex and main LHC ring are pictured here. The energies of each injection stage are as follows: linacs (50 MeV), PS booster (1.4 GeV), PS (26 GeV), SPS (450 GeV).

can be found in the recently completed ATLAS Detector and Physics Performance Technical Design Report [6] and in an upcoming CERN yellow book on the physics of the LHC.

1.2.3 Design of the LHC

The LHC must satisfy stringent design requirements in order to deliver the high luminosity[5] beams required for the physics programmes of its experiments. These requirements include a proton-proton centre of mass energy of 14 TeV and a peak luminosity of 10^{34} cm^{-2} s^{-1}.

The LHC will be installed in the 27 km circumference LEP tunnel (after the removal of the LEP ring). The injector complex consists of 50 MeV linacs, the 1.4 GeV PS booster, the 26 GeV PS (proton synchrotron) and the 450 GeV SPS. The injector complex and LHC main ring are shown in Figure 1.3.

In addition to operating as a proton-proton collider, the LHC will be able to operate as a heavy ion collider (Pb-Pb) with a centre of mass energy of 1250 TeV

[5]Luminosity is the number of particles per square cm per second crossing at an interaction point. It can be calculated via $L = f_n \frac{N_1 N_2}{A}$ where N_1 and N_2 are the number of particles in each bunch, A is the cross-sectional area of the beam and f_n is the revolution frequency.

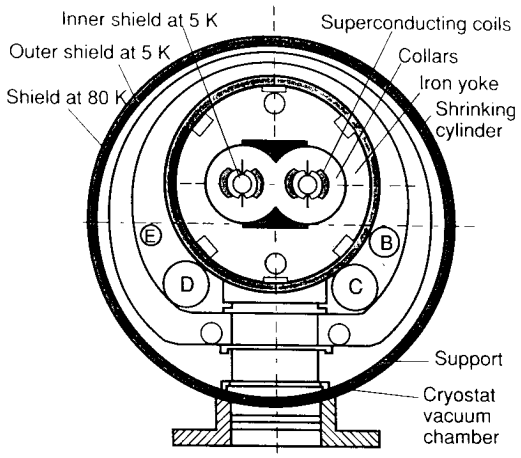

Figure 1.4: The cross-section of an LHC standard two-in-one dipole in its cryostat.

and a peak luminosity of 10^{27} cm^{-2} s^{-1}. This is a factor of 30 higher energy than the Relativistic Heavy Ion Collider (RHIC) at Brookhaven Laboratory. Also, the rebuilding of the LEP ring above the LHC ring would allow high energy e-p collisions to take place. The energy of these collisions would be 1.5 TeV, a factor of 5 higher than the energies currently available at the HERA collider at the DESY laboratory.

Since the LHC will initially collide beams of like-charged protons, two separate beam-lines are necessary to allow the two proton beams to circulate in opposite directions. CERN has decided to accomplish this by using a magnet design that combines the two guide fields into a single magnet as shown in Figure 1.4. This option was chosen over two separate magnets primarily due to space restrictions in the LEP tunnel. In order to meet the LHC energy requirements, these 14.2 metre dipole magnets must be superconducting (cooled with superfluid Helium) with a field strength of $\approx$8.3 Tesla. In all, 1296 dipole magnets will be required for the LHC. Beam focusing will be accomplished using 3.1 metre, 6.9 Tesla superconducting quadrupole magnets along with several other elements providing higher order corrections.

In order to maintain high luminosity, bunch lengths (the longitudinal spread of a bunch of particles being used in a collision) must be kept short. Short bunch lengths

energy	14 TeV
dipole field	8.33 T
coil aperture	56 mm
aperture separation	194 mm
luminosity	10^{34} cm^{-2} s^{-1}
injection energy	450 GeV
circulating current	0.54 A
bunch separation	25 ns
bunch spacing	7.5 m
particles/bunch	10^{11}
energy loss/turn	6.7 keV
luminosity lifetime	10 hours
beam separation in arcs (1.9K)	194 mm
stored energy per beam	350 MJ

Table 1.2: The design parameters of the LHC.

keep degradation in luminosity caused by beam crossing angle to a minimum. Short bunch lengths will be obtained at the LHC with RF cavities operating at 400 MHz needing a voltage of 8 MV at injection and 16 MV in collision. There will be eight of these superconducting cavities per beam (each beam has a separate RF system). Table 1.2 summarizes the LHC performance parameters.

The high luminosity environment provided by the LHC has implications for the design of detectors which use it. It mandates the use of radiation-hard materials in detector construction, limiting the technologies considered. It also produces a significant source of noise known as pileup. The small bunch separation which will be employed at the LHC (25 ns) means that detectors must use fast readout to avoid sampling events from several different bunch-crossings simultaneously. When events from more than one bunch-crossing are measured together they are said to have "piled-up" in the detector. Another source of pileup noise relevant at high luminosity is due to the high number of particles/bunch needed for the LHC. In addition to a possible hard-scatter event of interest, on average, 23 minimum bias events will be produced per bunch-crossing at design luminosity[6]. On average, these

[6]This number may be approximately calculated by multiplying the total LHC cross-section of 70 mb by the design luminosity of 10^{34} cm^{-2} s^{-1}. This yields an average of 18 events per bunch-crossing assuming a 25 ns bunch spacing. A more detailed knowledge of the the LHC bunch structure is required to obtain 23 events per crossing.

minimum bias events will produce an extra 3500 charged particles in the detector for each bunch-crossing [6].

1.3 The ATLAS Experiment

ATLAS is a detector designed to exploit the physics potential of the LHC. It is a general-purpose experiment designed to perform well in the high luminosity environment produced by the LHC. The necessity to withstand several years in a high radiation environment while providing data for a widely varied physics programme defines the design of the detector. Detailed reviews of the design of the ATLAS detector can be found in the ATLAS Technical Proposal [7] and in the technical design reports of its sub-detector groups. The goal of this section is to give a brief overview of some important aspects of the design of ATLAS.

As with most detectors in high energy physics ATLAS is composed of several sub-detectors. Figure 1.5 shows a cut-away view of the ATLAS detector exposing many of its important components. The inner detector, muon system and calorimetry are clearly visible. Each of these systems will be described briefly below.

1.3.1 Coordinate System

In order to understand the detector descriptions that follow some familiarity with the coordinate system used in ATLAS (and other hadron collider experiments) is required. The ATLAS coordinate system is a spherical system defined in terms of the z direction[7] (beam axis) a polar angle measured from this axis (θ) and an azimuthal angle (ϕ). In practice the polar angular coordinate is not expressed in terms of θ, but rather in terms of pseudorapidity defined as:

$$\eta = -\ln\left(\tan\frac{\theta}{2}\right). \tag{1.1}$$

In the limit of massless particles pseudorapidity is equivalent to rapidity, which offers distinct advantages as a measure of the polar angle. Under a change of reference

[7]The positive z-direction forms a right-handed coordinate system with an x-axis which points towards the centre of the LHC ring and a y-axis which points upwards.

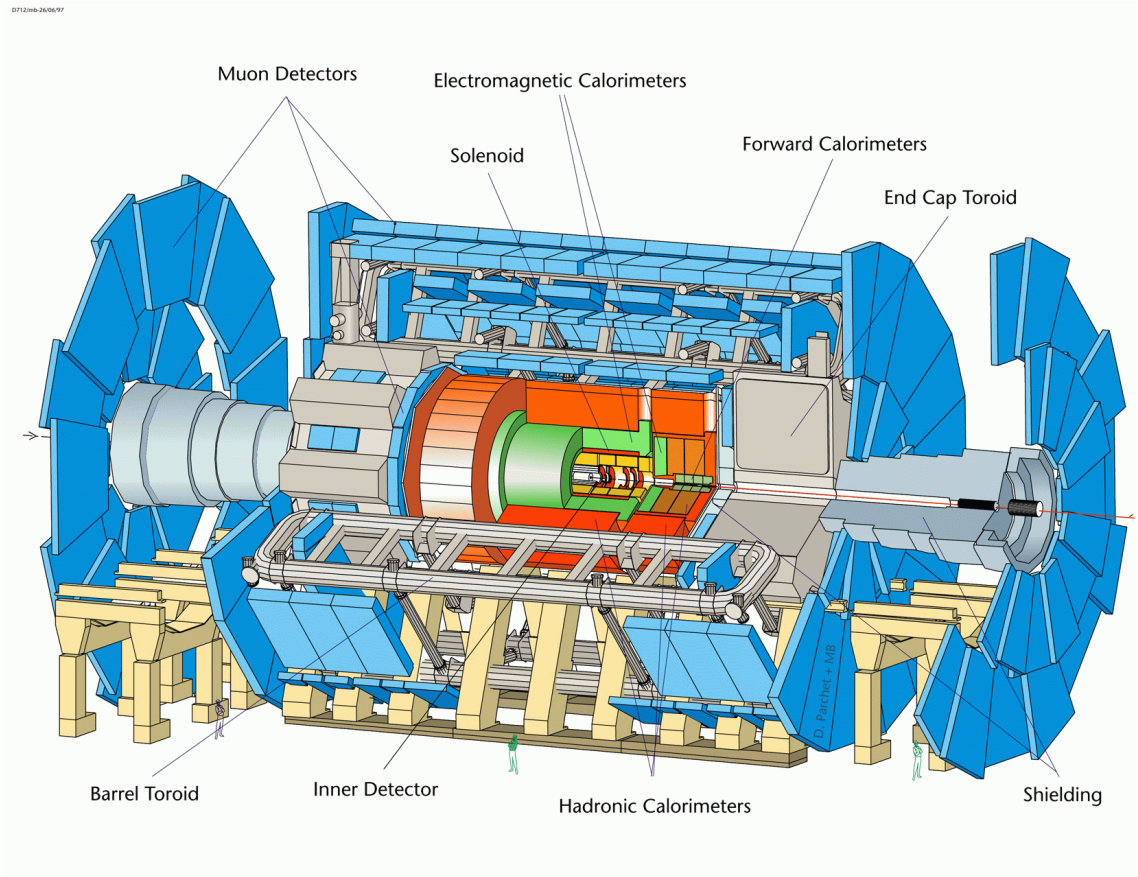

Figure 1.5: A cut-away view of the ATLAS detector.

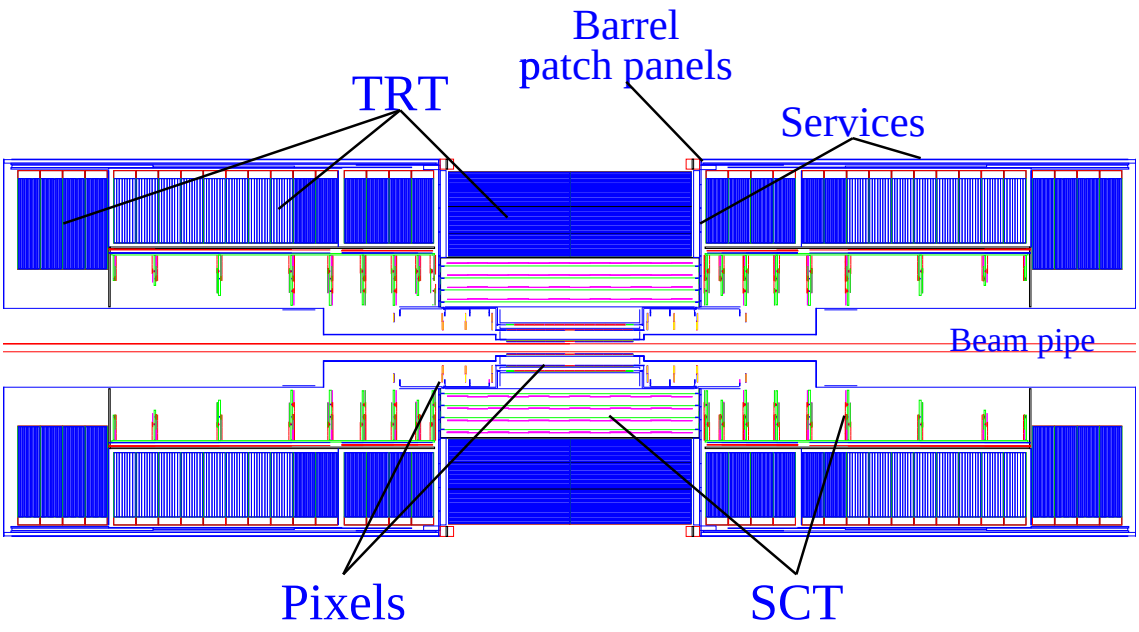

Figure 1.6: Cut-away view of the ATLAS inner detector.

frame (boost) along the z-direction the rapidity differential is invariant, making it particularly useful in measurements of longitudinally boosted systems (ie. interactions which do not occur at rest in the lab frame). Also, as mentioned previously, the distribution of charged particles from minimum bias events are distributed approximately uniformly in pseudorapidity. Physically this means that detector cells of equal size in pseudorapidity contain an approximately equal particle multiplicity.

1.3.2 The ATLAS Inner Detector

The task of the inner detector is to reconstruct the tracks and vertices in events with high efficiency [8]. It will contribute to electron, photon and muon identification and supply an important extra signature for short-lived particle decay vertices. The role of the inner detector in tagging b-jets is particularly important in b and top physics studies. A diagram of the ATLAS inner detector is presented in Figure 1.6.

The acceptance of the inner detector covers the pseudorapidity region from -2.5 to 2.5, matching the region of high granularity in the calorimetry. It combines high resolution detectors at inner radii with continuous tracking elements at outer radii,

System	Position	Area (m^2)	Resolution $\sigma(\mu m)$	Channels (10^6)	η range
Pixels	1 removable barrel layer	0.2	R-ϕ=12,z=66	16	$\pm$2.5
	2 barrel layers	1.4	R-ϕ=12,z=66	81	$\pm$1.7
	4 endcap disks on each side	0.7	R-ϕ=12,z=77	43	1.7-2.5
Silicon Strips	4 barrel layers	34.4	R-ϕ=16,z=580	3.2	$\pm$1.4
	9 endcap wheels on each side	26.7	R-ϕ=16,z=580	3.0	1.4-2.5
TRT	Axial barrel straws		170(per straw)	0.1	$\pm$0.7
	Radial endcap straws		170(per straw)	0.32	0.7-2.5

Table 1.3: Design parameters of the ATLAS inner detector.

all contained in a solenoidal magnet with a central field of 2 Tesla. It is composed of 2 major types of components: the semiconductor tracking (SCT) and the straw tube tracker (TRT). The semiconductor tracking is further divided into pixels and strips. Highest granularity around the vertex is achieved using semiconductor pixel detectors. Further from the vertex silicon microstrip technology is used. Outside of the SCT detectors are straw tubes which provide the possibility of continuous track following with much less material at a lower cost than semiconductor detectors. A summary of the performance and η coverage of the elements of the inner detector are shown in Table 1.3.

1.3.3 ATLAS Muon System

The quality of the muon measurement has been one of the guiding design criteria for the ATLAS experiment [7]. High momentum final state muons are among the most promising and robust signatures of physics at the Large Hadron Collider [9]. On this basis ATLAS has decided to use a high resolution muon spectrometer with stand alone triggering and momentum measurement capabilities over a wide range of transverse momentum, η and ϕ. A cut-away view of the ATLAS muon system is presented in Figure 1.7.

The ATLAS muon system uses three air-core superconducting toroid magnets

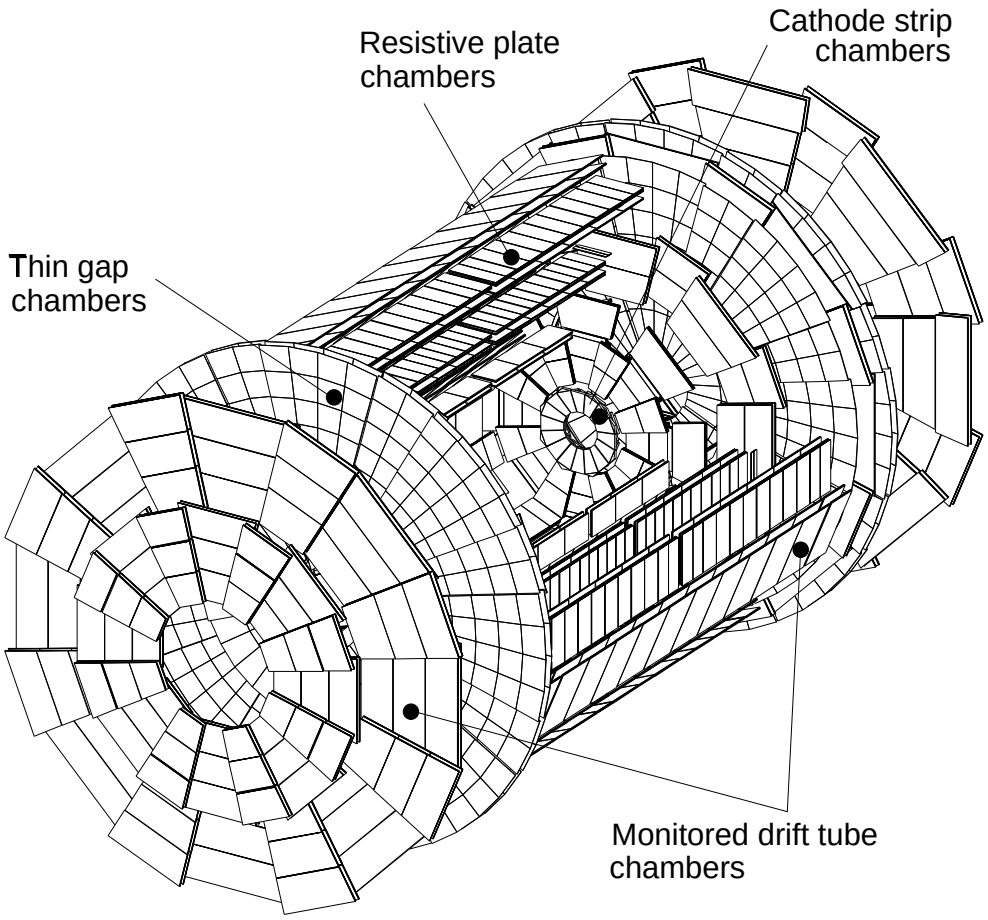

Figure 1.7: Cut-away view of the ATLAS muon spectrometer. It is approximately 26 m in length and has a diameter of 20 m.

to produce a large volume field with an open structure that minimizes multiple scattering contributions to the momentum resolution. For precision measurements of muon tracks in the principal bending direction of the magnetic field Monitored Drift Tube (MDT) chambers are used except in the high-flux inner regions of the endcap where Cathode Strip Chambers (CSC) are used. There are separate sets of chambers employed for triggering. In the barrel region there are three stations of Resistive Plate Chambers (RPC) and in the endcap three stations of Thin Gap Chambers (TGC) expressly for the purpose of triggering. A complete description of the technology employed in these different chamber types is beyond the scope of this work but can be found in the Muon Spectrometer Technical Design Report [9].

1.3.4 ATLAS Calorimetry

Calorimetry plays a central role in ATLAS. ATLAS calorimeters are designed to provide fast signals used to decide whether to read out the detector (known as triggering) and to provide precision measurements of electrons, photons, jets and missing transverse energy [10]. Two different types of calorimeter technology are used in ATLAS: liquid argon calorimeters are used for all of the electromagnetic calorimetry, the endcap hadronic and forward calorimeters while scintillating plates are used for the barrel hadronic calorimeter. Liquid argon calorimetry, in particular the design of the Hadronic Endcap Calorimeter (HEC) is presented in Chapter 2. Detailed designs of the other liquid argon calorimeters are available in the ATLAS Liquid Argon Technical Design Report [10] while details of the barrel hadronic calorimeter are available in the ATLAS Tile Calorimeter Technical Design Report [11]. A cut-away view of the ATLAS calorimetry is presented in Figure 1.8.

Several unique calorimeter geometries are employed in ATLAS. The barrel and endcap electromagnetic calorimeters use lead plates bent into an "accordion" shape which allows readout towers to point towards the interaction region. A major advantage of this design is that it allows calorimeter readout with minimal dead space (it is a hermetic design) [12]. The forward calorimeter uses a structure of rods and

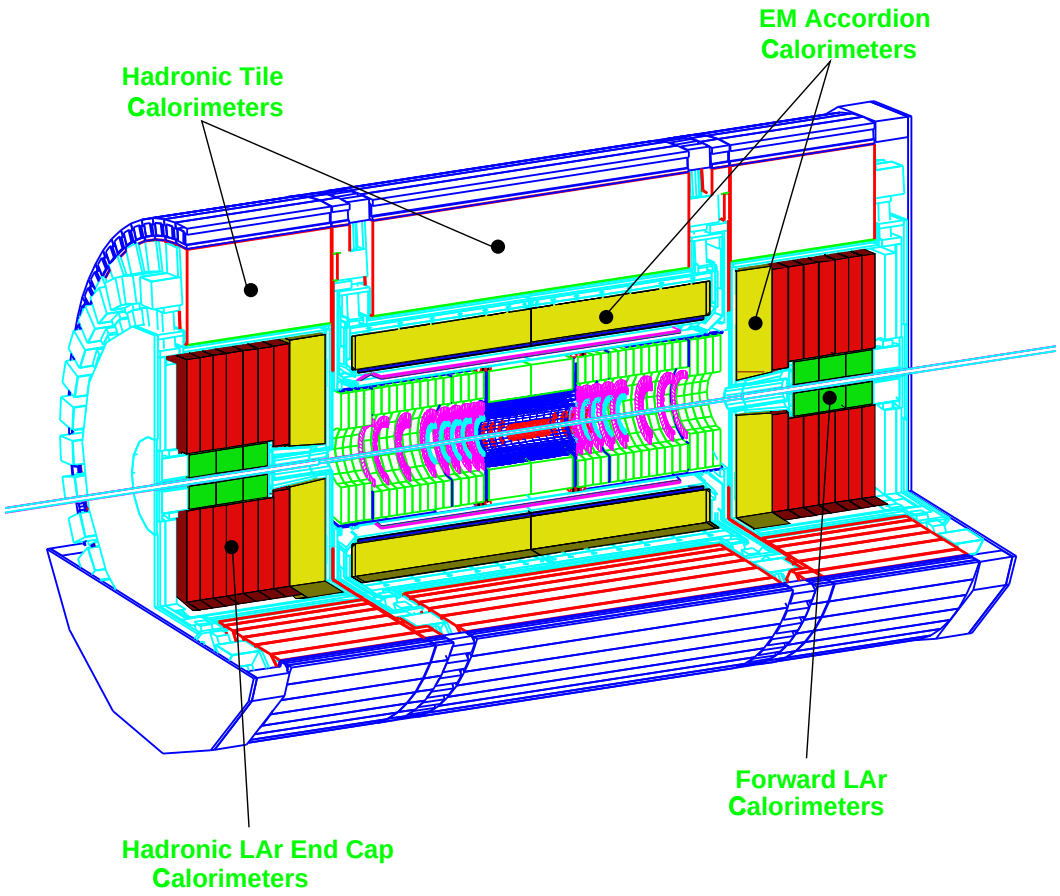

Figure 1.8: Cut-away view of the ATLAS calorimetry. The calorimetry system is more than 12 m long and has a radius of 8 m.

tubes to create very thin cylindrical liquid argon gaps. These thin gaps are needed to provide a short drift time in the gap, thereby controlling charge build-up problems which could occur in the high-radiation forward region of ATLAS. Finally, the tile calorimeter, which will be used as the barrel hadronic calorimeter, uses scintillating tiles which are aligned with the particle direction. This design allows hadronic showers to be measured (sampled) in a homogeneous manner.

Chapter 2

Performance of the ATLAS Hadronic Endcap Calorimeter

Calorimetry is an important aspect of most detectors in high energy physics. This chapter will briefly summarize the general principles of calorimetry and of the physical processes exploited by the technique. After introducing calorimetry, a detailed analysis of the performance of modules of the ATLAS Hadronic Endcap Calorimeter (HEC) is presented.

2.1 Shower Processes

Electromagnetic Showers

When an electron of sufficient energy ($>\sim$10 MeV) interacts with matter via the electromagnetic force its primary mechanism of energy loss is through photon emission via bremsstrahlung. This is illustrated in Figure 2.1 for electrons interacting in lead. If the photon emitted via bremsstrahlung is sufficiently energetic it will produce an e^+e^- pair, each of which may be capable of emitting a photon via bremsstrahlung. In this manner a single incident particle can create a "shower" of particles when it interacts with matter. This is referred to as an electromagnetic shower. A very simplified drawing of an electromagnetic shower is shown in Figure 2.2. The shower continues to grow until the energy of showering electrons falls much below the "critical energy" (E_c). E_c is defined as the energy at which energy

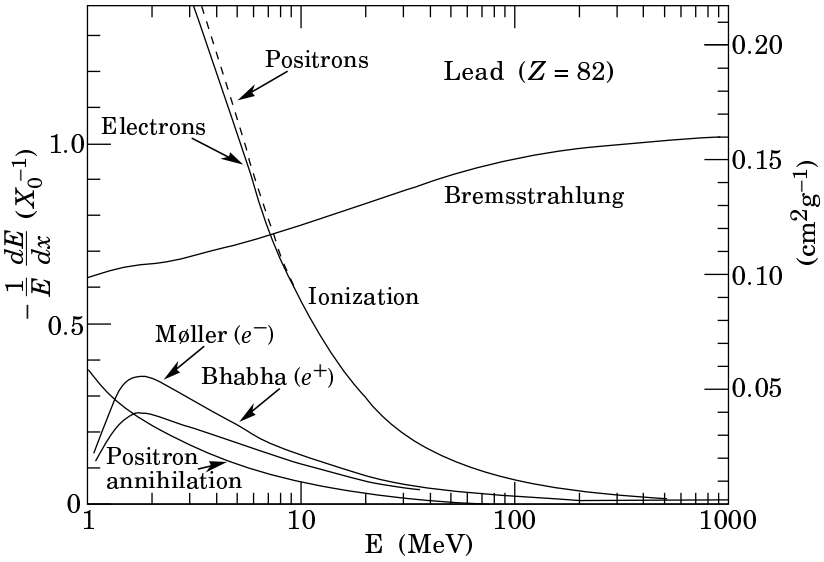

Figure 2.1: Fractional energy loss per radiation length for electrons interacting in lead. This figure is taken from [13] where it is Figure 24.4.

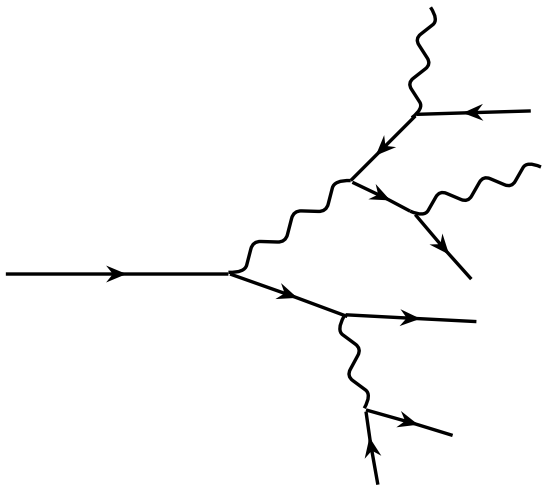

Figure 2.2: Schematic view of an electromagnetic shower. Lines with arrows represent electrons and positrons, wavy lines represent photons. This diagram is redrawn from [14].

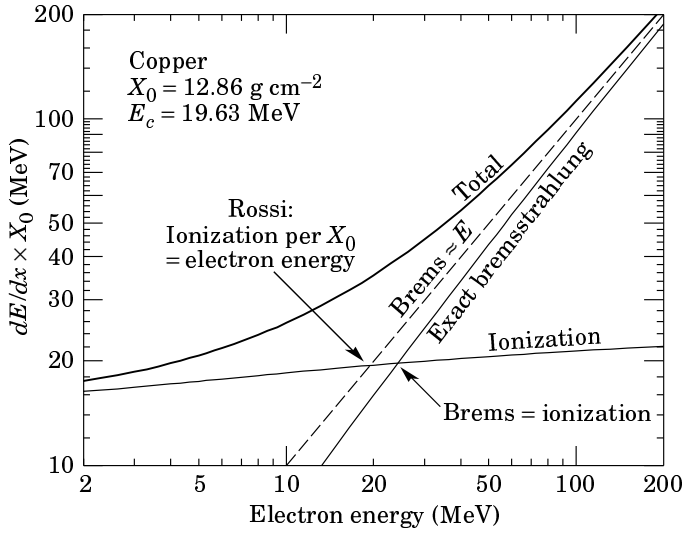

Figure 2.3: Two definitions of the critical energy are shown. This figure is taken from [13] where it is Figure 23.6.

loss via ionization is equal to energy loss via bremsstrahlung. Therefore, below this energy bremsstrahlung is no longer the dominant energy loss mechanism for electrons and the shower dies. A plot illustrating the definition of E_c in copper is shown in Figure 2.3.

The longitudinal development of an EM shower in a given material is governed by the radiation length of that material [15]. The radiation length, X_o, is defined as the distance over which the energy of an electron is reduced by a factor of 1/e due to radiation loss only

$$E = E_o e^{-\frac{x}{X_o}} \tag{2.1}$$

where x is the distance traveled in the material, E is the energy remaining and E_o is the initial energy of the electron. An approximate formula for the calculation of the radiation length in a given material is given by

$$X_o \simeq 180 \frac{A}{Z^2} \rho \tag{2.2}$$

where X_o is in cm if ρ (the material density) is in g/cm^3, Z is the atomic number and A is the atomic weight associated with the element. The photon conversion length

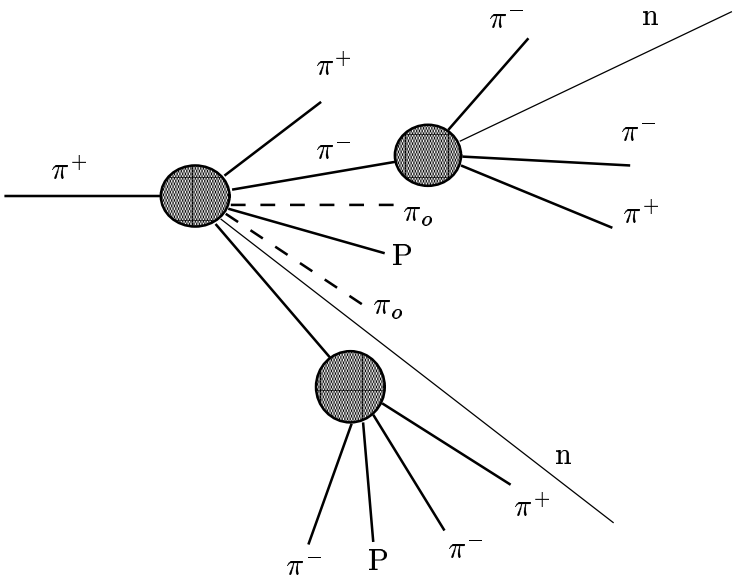

Figure 2.4: Simplified diagram of an hadronic shower. EM showers created by π_o interactions are not shown.This diagram is redrawn from [14].

(X_p), the average distance a high energy photon will traverse before converting to an e^+e^- pair, is related to the radiation length by $X_p = (9/7)X_o$.

The natural scale for the transverse development of electromagnetic showers is given by the Molière Radius which is defined as

$$R_m = \frac{21\text{MeV}}{E_c} X_o \tag{2.3}$$

where E_c is the "critical" energy and X_o is the radiation length. Roughly 95% of a shower is contained laterally in a cylinder of radius $2R_m$ [16].

Hadronic Showers

Hadronic showers can occur when particles interact with matter via the strong force. A simple schematic of an hadronic shower is shown in Figure 2.4. These showers are different in character from EM showers and the theory of their development will be detailed below.

Hadronic showers can be thought of as consisting of 2 components; the purely hadronic part of the shower and the electromagnetic part of the shower. Electro-

magnetic sub-showers will be formed within hadronic showers by the creation of neutral pions (π_o) which decay almost exclusively to two photons. Approximately 1/3 of an hadronic shower will actually be electromagnetic due to neutral pion emission. The behaviour of the EM portion of an hadronic shower will be governed by the physics described in the previous section. Though the average electromagnetic fraction of hadronic showers is $\sim 1/3$, the event-to-event fluctuation of this fraction is large. It also exhibits a weak energy dependence which has been parameterized by Wigmans [17] as

$$f_{\pi_o} = k \log \frac{E}{E_h} \tag{2.4}$$

where E is the incident particle energy, α is a constant which is usually taken to be $\sim$0.1, f_{π_o} is the fraction of the shower which is electromagnetic in character and E_h is the scale energy for the process (assumed to be 1 GeV for pions). A second, more recent proposal has been put forth by Groom [18] which replaces the logarithmic energy dependence with a power law dependence

$$f_{\pi_o} = 1 - \left(\frac{E}{E_h}\right)^{m-1} \tag{2.5}$$

where m is a constant which has been experimentally measured to be 0.8-0.9 (typically 0.83). In either parameterization the EM fraction rises with energy. This is due to the fact that higher energy hadrons undergo more interactions with matter and hence have a greater opportunity to produce π_o's. The transfer of energy from the hadronic to electromagnetic sectors is a one-way process, the decay products of π_o's will not start hadronic showers. Once a π_o has been produced the energy it carries is deposited via electromagnetic showers.

The purely hadronic part of hadronic showers is difficult to model. One of the reasons for this difficulty is the number of processes which contribute to energy loss in an hadronic shower. There are more than 300 processes which contribute approximately equally (more than 0.1% each) to the total cross-section of the interaction [17,19]. Theoretical modeling of low energy QCD processes is not well enough developed to produce precise, reliable predictions for all of these processes. Since

no detailed theoretical description exists which reliably reproduces the data, phenomenological descriptions have been developed. One such model is spallation [17]. This model assumes that an hadronic shower progresses in two distinct stages; a fast stage and a slow stage.

The fast stage of spallation occurs when a high energy hadron interacts with matter via collisions with nucleons within the nucleus. The struck nucleons may be ejected from the nucleus with enough energy to enter another nucleus and eject further nucleons or nuclear fragments. This process is known as a fast intranuclear cascade and it occurs on a time-scale of $\simeq 10^{-22}$ seconds [17, 20].

The slow stage of the shower occurs via de-excitation of the nuclei created in the intra-nuclear cascade. This is referred to as the shower evaporation step. Nucleons and photons are emitted in successive evaporation steps until the excitation energy is less than the binding energy of one nucleon.

Just as the intrinsic distance scale for EM showers is set by the radiation length of a particular material, the intrinsic length scale for hadronic showers in a material is given by its nuclear interaction length (λ_o). The probability that a particle will interact after traversing a distance x in a material is given by:

$$1 - e^{-\frac{x}{\lambda_o}} \tag{2.6}$$

The nuclear interaction length in a particular material can be roughly calculated by:

$$\lambda_o \simeq 35\frac{A^{1/3}}{\rho} \tag{2.7}$$

for protons (it is slightly higher for pions) [14] where λ_o is in cm if ρ is in g/cm^3. The depth necessary for shower containment scales logarithmically with energy and the depth of shower maximum occurs at [14] (in units of λ_o)

$$t_{\max} = 0.2 \ln E(\text{GeV}). \tag{2.8}$$

Hadronic showers tend to be much broader than EM showers even though their cores are relatively narrow. The transverse radius for 95% containment is approxi-

mately 1 interaction length roughly independent of energy [15]. However, the fluctuations in the lateral spread of hadronic showers are large.

2.2 Calorimetry

The primary purpose of a calorimeter is to measure the energy of incident particles. One aspect of showers which makes them very amenable to measurement is that the number of particles in the shower is directly proportional to the energy of the incident particle. For EM showers the number of particles tends to be very high ($\sim$1000 at shower maximum) minimizing the statistical fluctuation on the measurement. Therefore, a detector designed to measure particle multiplicity, track length or related quantities can be used to make high-precision measurements of energy with a relatively straightforward calibration.

Among particle detectors calorimeters possess certain unique features. Unlike techniques in which particle momentum is measured by its deflection in a magnetic field, calorimeters are designed to completely contain a particle and its decay products. This provides calorimetry with the ability to measure the energy of neutral particles which interact with matter in the detector. A second feature of calorimeters which gives them an advantage in high energy physics experiments is that the energy resolution provided by calorimeters improves with increasing energy. Magnetic deflection techniques degrade with increasing particle energy.

There are two fundamentally different types of calorimeters; homogeneous and sampling. This section will focus on sampling calorimetry as this is the type used in ATLAS.

Sampling Calorimetry

Sampling calorimeters are shower detectors designed to exploit the properties of EM and hadronic showers. They are designed to take many separate measurements ("samples") of the shower throughout its development. A sampling calorimeter is constructed of alternating layers of absorber and "active" medium. The absorber

is usually either a high-Z material, in the case of an EM calorimeter, or a dense material with a large interaction length, in the case of an hadronic calorimeter, which is responsible for producing showers and enabling full containment calorimeters to be built within a reasonable physical size. The active medium is where the actual measurement of the properties of the shower takes place.

Two important aspects of this design are sampling frequency and sampling fraction. Sampling frequency describes the number of samples per unit depth while sampling fraction describes the fraction of the total shower energy which is sampled. In general, a higher sampling fraction and frequency will lead to a better intrinsic resolution in a sampling calorimeter.

The material of the absorber is chosen based on its physical characteristics in relation to shower development. For example, the radiation length of a given material is a vital characteristic in determining its value as an absorber in an EM calorimeter, while the nuclear interaction length is the scale of importance for hadronic calorimeter absorbers. Of course, practical considerations such as mechanical properties, availability and cost are also important in this choice.

The choice of active medium also plays an important role in calorimeter design. Different types of active media exploit different physical processes in order to measure energy. Plastic scintillator detectors make use of molecular excitation and subsequent photon emission to detect showers while ionization-induced currents are used in gases and liquids. In ATLAS all of the endcap calorimetry makes use of liquid argon ionization calorimetry. This technique will be the focus of the descriptions that follow.

The liquid Argon ionization calorimetry technique is based on detecting currents induced by the motion of ionization electrons in an applied electric field. The electrons are produced by the passage of charged particles through the argon creating electron-ion pairs (see Figure 2.5). The size of the total current collected in this manner is proportional to the energy deposited in argon by a particle passing through the gap. The detailed design of the ATLAS Hadronic Endcap liquid argon

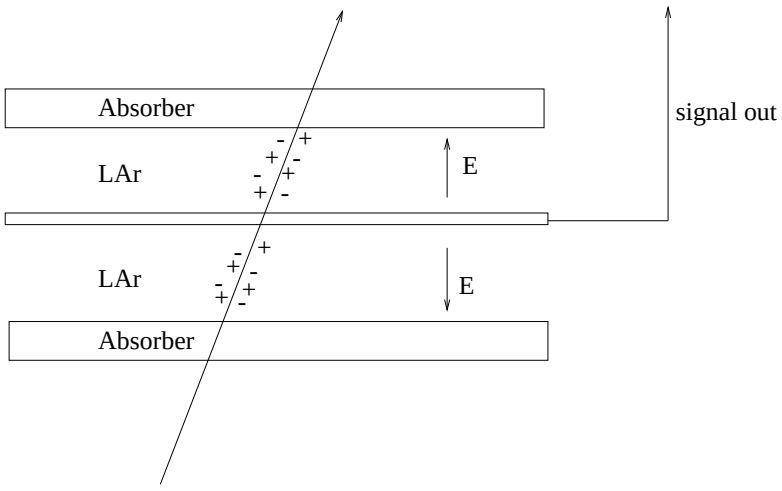

Figure 2.5: Schematic drawing of a liquid argon (LAr) ionization chamber. Shown is a single particle traversing the LAr gap, producing free charges. The drifting electrons then induce a signal on the central readout plane.

calorimeter will be presented in Section 2.3.

Energy Resolution

The precision with which the energy of a particle can be measured in a calorimeter is known as its energy resolution. For a given energy of particle incident on a calorimeter, the measured energy follows a normal distribution for fully contained showers. The width of this distribution divided by its mean is the resolution at that energy.

The energy dependence of the energy resolution of a sampling calorimeter can be parameterized as

$$\frac{\sigma}{E} = \frac{A}{\sqrt{E_o}} \oplus B \oplus \frac{C}{E} \tag{2.9}$$

where E is the measured energy, E_o is the true original particle energy and $\oplus$ represents addition in quadrature. The first term in this expression is referred to as the sampling term and is primarily determined by the intrinsic sampling fraction and frequency of the calorimeter for EM calorimeters and by intrinsic shower fluctuations in hadronic calorimeters. The second term is referred to as the constant term. Some influences on the constant term are mechanical imperfections, incomplete shower

containment and non-compensation[1]. The third term is present to take into account the effect of electronic noise on the resolution. From this form it can be seen that calorimeter performance improves with energy. At high energies the constant term will dominate the resolution. Note that, in this parameterization, the sampling and noise terms are divided by different energies. The sampling term is scaled by the incoming particle energy since the development of the shower is sensitive to the energy of the particle. For example, in an hadronic shower, the fraction of energy deposited via electromagnetic sub-showers depends on the initial energy of the incident particle. The contribution of electronic noise to the width of the energy distribution does not depend on energy. It is convenient to divide its contribution to the resolution by the same energy which is used to define the overall resolution. Since it is often possible to perform an independent measurement of C this allows its contribution to the overall resolution to be subtracted in a straightforward manner. Since E_o is usually not known a priori, many analyses parameterize the energy resolution solely in terms of E.

This parameterization is well tested and well accepted for calorimeters measuring electromagnetic showers. However, for hadronic showers this parameterization does not work as well. It has been suggested [17] that the $E^{1/2}$ scaling of the sampling term is not quite correct for hadronic showers. Also, the dominant contribution to intrinsic hadronic resolution is different from that of intrinsic EM resolution. This dominant contribution comes from statistical fluctuations in the shower. In particular, fluctuations in the fraction of shower energy which is produced electromagnetically (via π_o production) in the hadronic shower may make a large contribution to the resolution [15]. This effect can be minimized by designing a "compensating" calorimeter. The issue of compensation is addressed in the next section.

[1] Compensation is described in the following section.

e/h - Compensation

A compensating calorimeter is one that has an equal response to electromagnetic and hadronic energy. For most calorimeters the hadronic response will be smaller than the electromagnetic response. This is conventionally expressed as e/h > 1. The reason for this difference in response is that a large fraction of the energy of the purely hadronic part of hadronic showers is not detected in the calorimeter. In Section 2.1 spallation in hadronic showers is described as consisting of two stages. The first stage, fast intranuclear cascade, produces invisible energy loss through binding energy losses and the production of low energy neutrons. The second stage of the shower, shower evaporation, is virtually invisible to the calorimeter as the particles produced are often short range and so do not exit the absorber or are lost to saturation effects in the active medium [15].

Compensation can be achieved either through software or hardware means. Software compensation relies on fine segmentation of the calorimeter with which it is possible to isolate "hot spots" of electromagnetic activity. Since electromagnetic and hadronic shower components can be partially separated, different weights can be applied to each calorimeter cell to bring the effective e/h to 1. This technique is being successfully used by the H1 collaboration (also liquid argon ionization calorimetry) [21]. Compensation can also be achieved through appropriate choices of material for the absorber and active medium. Clearly, if e/h$>$1, materials which suppress the EM response or enhance the hadronic response will improve the e/h ratio. A common strategy for hardware compensation is choosing uranium as the absorber material. A uranium absorber can enhance the hadronic response of a calorimeter by producing many more neutrons in a typical shower than a lower-Z absorber would. If the active medium is chosen to be proton-rich (eg. scintillating plastic) these neutrons can be detected and will enhance the hadronic response.

As mentioned in the previous section non-compensation has a detrimental effect on calorimeter resolution. It has effects on both the sampling and constant terms of the calorimeter resolution. It makes a contribution to the sampling term due to the

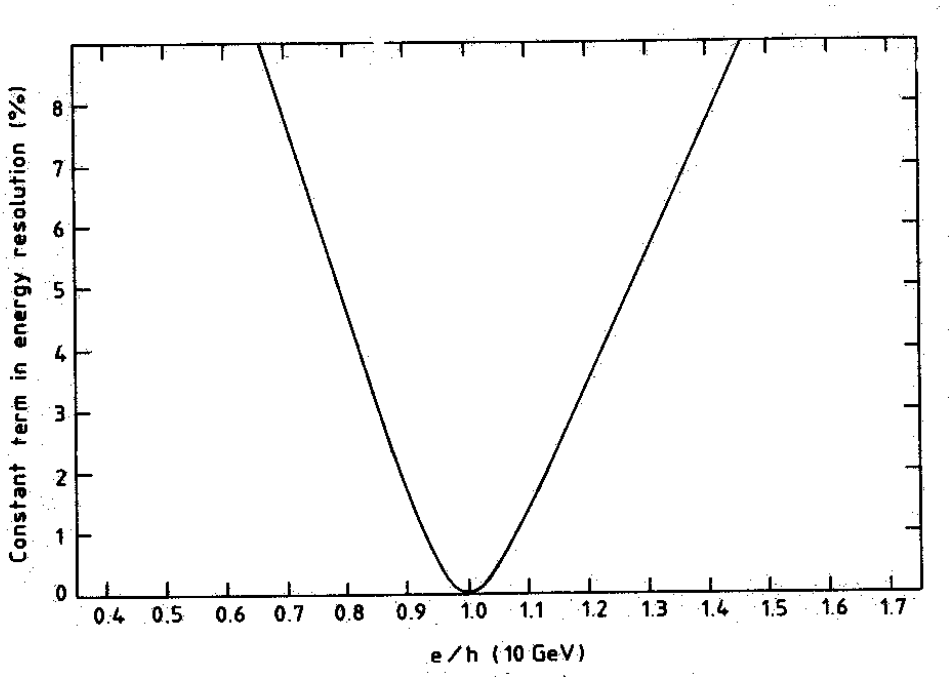

Figure 2.6: Dependence of constant term of resolution on e/h ratio. Taken from Wigmans [17] where e/h was calculated at 10 GeV incident energy.

event-to-event fluctuations in the electromagnetic component of hadronic showers. If the EM and hadronic responses are different the effect of this fluctuation on the sampling term is amplified. The constant term also depends on e/h, Figure 2.6 (taken from [17]) shows the dependence of the constant term on the intrinsic e/h ratio. This clearly shows that the optimum value of e/h is 1.

2.3 Design of the Hadronic Endcap

Hadronic calorimetry is essential in performing many of the physics studies envisioned for ATLAS. The ATLAS Hadronic Endcap Calorimeter (HEC) is designed to meet several physics measurement goals while maintaining good performance in the high radiation forward region of ATLAS.

Design Goals and Requirements

The primary functions of hadronic calorimetry at ATLAS are to perform jet reconstruction and E_t^{miss} measurement. Jet identification and measurement, jet-jet mass reconstruction and forward jet identification are essential for many physics studies. E_t^{miss} measurements are valuable for many physics measurements and searches including the search for supersymmetric particles.

The jet energy resolution goals set by the above physics requirements are

$$\frac{\Delta E}{E} = \frac{(50 \text{ to } 100)\%}{\sqrt{E\text{GeV}}} \oplus (3 \text{ to } 10)\% \tag{2.10}$$

where the $50\%/\sqrt{E}$ requirement and 3% constant term apply to $|\eta| < 3$ and the overall resolution for jets is determined by the combined performance of the electromagnetic and hadronic calorimeters. Simulations and beam test results of current designs indicate that these goals can be met in the ATLAS environment [22].

These physics goals impose strict requirements on many aspects of the design of the Hadronic Endcap Calorimeter [22]. For instance, in order to meet the forward jet tagging requirements for heavy Higgs boson and other searches the ATLAS calorimetry must extend to $|\eta| = 5$. This means that the HEC, which extends to $|\eta| = 3.2$, and the forward calorimetry must operate in a high radiation environment, mandating the use of radiation-hard electronics for the readout. Other constraints on the readout design for the HEC come from pileup noise. Pileup from several bunch-crossings must be controlled by using fast readout. However, the effect of pileup noise must be balanced against higher electronic noise produced by fast readout. Another constraint arises from the potential for jets of very high energy to be present in the endcap region and the need to identify muons for b-jet tagging. This sets high standards for dynamic range of the detector and the electronics. Also, the total thickness required for full shower containment is about 10 interaction lengths (λ). Without this depth, leakage of particles from hadronic showers would degrade the jet resolution and serve as a significant background for the muon chambers located outside of the calorimetry.

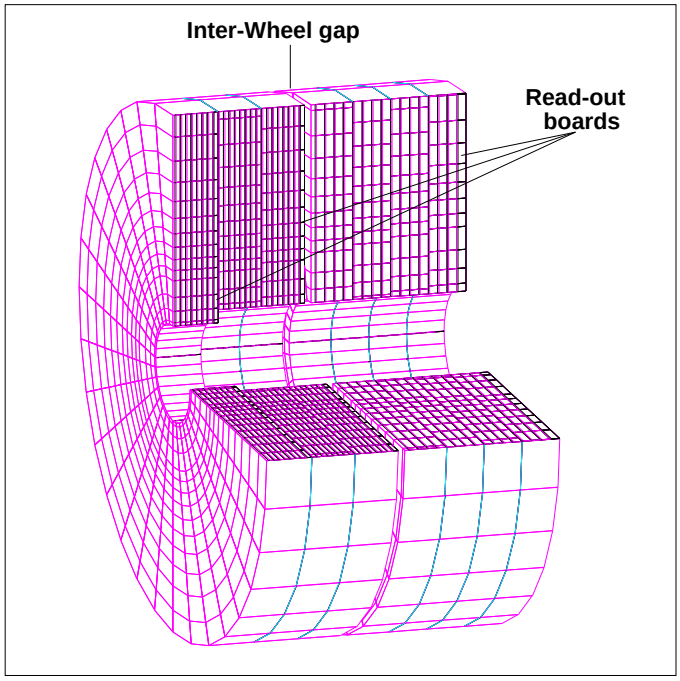

Figure 2.7: The structure of the hadronic endcap is shown. The two wheels, as well as the inter-wheel gap are clearly shown. Each wheel extends 2 m in radius from the beam axis.

Design of the Hadronic Endcap Calorimeter

The ATLAS Hadronic Endcap Calorimeter is located at either end of the ATLAS tracking volume ($1.5 < |\eta| < 3.2$). It is a sampling calorimeter which is composed of copper absorbers with liquid argon as the active medium. This technology was chosen to produce a radiation resistant detector with a simple mechanical design capable of covering the large area occupied by this sub-detector in a cost-effective way [10]. Each endcap is divided into two wheels as shown in Figure 2.7. The first wheel is constructed of a 12.5 mm thick front plate followed by 24 plates which are each 25 mm thick. The second wheel is constructed of a 25 mm front plate followed by 16 plates which are each 50 mm thick. The liquid argon gaps are 8.5 mm thick in both wheels. The thicker plates in the rear wheels were chosen based on cost and space constraints. For the purposes of readout each wheel is divided into 2 separate units in depth. One full HEC wheel will consist of 32 pie-shaped modules. The

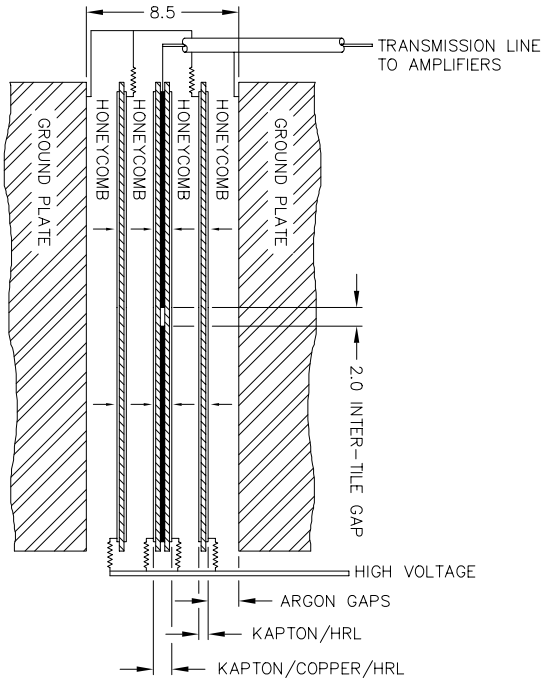

Figure 2.8: Schematic of the arrangement of the readout structure in the 8.5 mm inter-plate gap.

readout segmentation will be $2\pi/64$ in ϕ and 0.05-0.1 in pseudorapidity.

The readout structure within a liquid argon gap is presented in Figure 2.8. The 8.5 mm liquid argon gap contains three boards which divide the gap into 4 sub-gaps. The central board is the "PAD board" which contains the segmented readout electrodes. The outer boards are part of the electrostatic transformer structure (EST) [23] which optimizes signal-to-noise ratio while reducing the high-voltage requirement and ionization pile-up. The EST structure also has the advantage of limiting high-voltage sparks and shorts [10].

2.4 Hadronic Endcap Beam Tests

Hadronic Endcap modules built to the final ATLAS design specifications have been tested in particle beams at CERN in April and August of 1998. The tested modules consist of four phi segments (2 per module) totaling 1/16 of one endcap. Smaller scale prototype modules have previously been tested in 1996 and 1997 [24]. How-

ever, the modules tested in 1998 are the first built to the final ATLAS design specifications and, unlike previous prototypes, contain 10 nuclear interaction lengths providing near full longitudinal containment of hadronic showers. Also, better lateral containment is achieved by these modules than by any previous modules. This document refers only to the 1998 tests.

The construction of the ATLAS Hadronic Endcap modules was completed in spring 1998. In April 1998, data were recorded for pion, electron and muon beams with energies ranging from 20 to 180 GeV. This work focuses on the energy scans that were performed at several impact positions to assess the energy response and resolution of the calorimeter and on the calculation of its intrinsic e/h.

In Section 2.4.1 an overview of the experimental setup is presented. The data samples (runs) are briefly described in section 2.4.2. Sections 2.4.4 and 2.4.5 concentrate on determining the response and resolution of the calorimeter to electrons and pions respectively. Section 2.4.6 presents measurements of the intrinsic e/h of the detector. Finally, Section 2.5 presents the conclusions.

2.4.1 Beam Test Setup

The HEC modules were installed in the former H1 cryostat[2] in the H6 beamline of the SPS at CERN. The cryostat was filled with liquid argon maintained at 90.7±0.1 K. Trigger counters and multi-wire proportional chambers installed in the beamline (see Figure 2.9) provided trigger and particle position information.

Trigger Detectors

Event selection (triggering) was done with the aid of several detectors in front and behind the cryostat. Refer to Figure 2.9 for the locations of the various detectors in the beam test setup. $B1$ is a scintillating detector upstream from the cryostat where the beam leaves the beam pipe after being bent by the last dipole magnet, Bend9. $F1$ and $F2$ are scintillating detectors which effectively define the transverse size of

[2]H1 is an experiment currently taking data at the HERA collider. It also makes use of liquid argon ionization calorimetry and its beam test cryostat is used for the HEC tests.

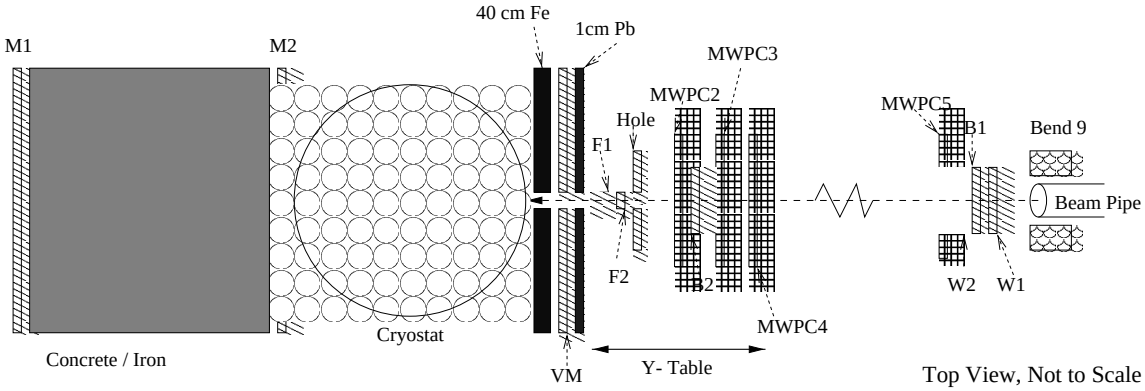

Figure 2.9: Setup of the HEC beam tests. The items in the diagram are: bend 9: final bending magnet; W1,B1,B2,W2: beam counters; MWPC: multiwire proportional counters (beam chambers); F1,F2: finger counters which define transverse size of the beam; VM: muon veto; M1,M2: muon counters.

the beam for triggered events. They are mounted on a motorized table (y-table) which can be displaced in the vertical direction. VM is a planar array of scintillating detectors located close to the front of the cryostat with an aperture in the center coinciding with the cryostat window. *hole* is a scintillating detector mounted on the y-table with a small aperture in its center. $M1$ and $M2$ each form a planar array of scintillating detectors behind the cryostat for muon identification.

The HEC Modules

Though the Hadronic Endcap is constructed to provide a semi-pointing geometry in pseudorapidity, space constraints within the test cryostat prevented the modules from being positioned in their proper pointing orientation (see Figure 2.10). For this reason, an hadronic shower deposited energy in a larger number of cells than it would in the proper pointing orientation. This necessitated the use of a larger group (cluster) of cells, which increased the electronic noise contribution to the energy resolution.

For the 1998 beam tests the calorimeter was electronically divided into three longitudinal readout segments. The first segment ($z = 1$) consists of 8 liquid argon (LAr) gaps each separated by 2.5 cm of copper. The second segment ($z = 2$) consists of 16 LAr gaps also separated by 2.5 cm of copper. The third segment

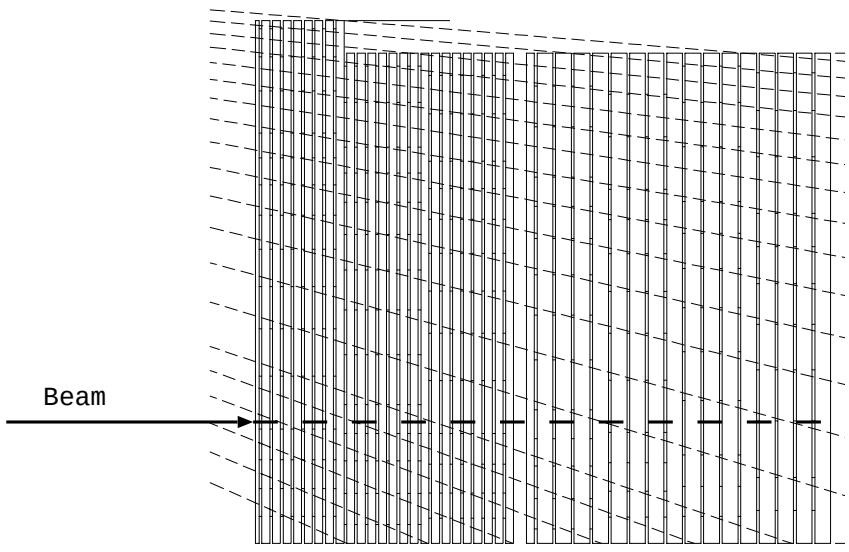

Figure 2.10: Orientation of the beam with respect to the calorimeter. The thick line represents the incident (non-pointing) particle beam. The thin dashed lines are drawn at constant pseudorapidity from the ATLAS interaction point, such that a particle traveling in a straight line from the vertex would follow this trajectory. The readout cells are positioned in a "semi-pointing" manner which follows these pseudorapidity lines in a stepped fashion. The total height of the module is 1.63 m.

($z = 3$) consists of 16 gaps each separated by 5 cm of copper[3]. A readout cell is defined as a pointing tower spanning a longitudinal readout segment. The change in sampling fraction in the second wheel of the calorimeter necessitates the application of a factor of two to the measured energy in cells in the third longitudinal segment relative to cells in the first two segments.

The two tested modules are identical with the exception of the high resistive coating which implements the high voltage distribution within the gaps. One module uses a Carbon Loaded Paint (CLP) as a resistive coating, while the other uses a Carbon Loaded Kapton (CLK) resistive coating. In the final ATLAS design the CLK resistive coating will be employed in all modules.

During the April 1998 beam period, module 2 suffered from minor high voltage problems in its third readout segment, requiring 1 subgap in each of the first 8 gaps to be disconnected from high voltage, while one subgap in each of the second 8 gaps had its high voltage reduced by $\frac{1}{3}$. As will be shown in the sections to follow, the resolution of module 2 is completely recoverable by using simple multiplicative depth constants to offset the effective change in sampling fraction due to HV problems.

Readout and Calibration

The readout of the HEC beam test modules is similar to the one in the final ATLAS design. Signal is read out from fast analog to digital converters (flash ADCs) every 25 ns. Details of signal reconstruction are presented in Section 2.4.3. This design allows experience to be gained with HEC readout and signal reconstruction which can be directly applied to the ATLAS readout.

The calibration required to convert ADC counts to the current produced in a liquid argon readout cell (composed of many argon gaps) is produced using a stand-alone calibration system. Calibration pulses of known charge, produced in external calibration generators, are used to inject a known current into the signal lines connected to the readout pads. A function relating injected current to ADC units is

[3]In ATLAS the third depth will be divided into two 8-gap readouts. This design decision was made primarily for muon detection and was not implemented until after the 1998 tests.

Position	Impact Cell	x (mm)	y (mm)
Module 1			
D	5	-100	+83
H	3	-100	-67
Module 2			
E	78	+100	+83
I	76	+100	-67

Table 2.1: Beam impact positions for 1998 HEC beam tests are defined.

constructed. It is parameterized in terms of a 3rd order polynomial with different constant coefficients for each readout cell. The coefficients of the polynomial's quadratic terms typically have a negligible effect. This implies that the function is almost linear. The main goal of this procedure is to calibrate the gain of each readout cell. This calibration corrects cell-to-cell differences in the gain. The procedure also allows energy in ADC units to be converted to energy in units of current (nA) produced in the gap by ionization.

2.4.2 Beam Test Data Samples

Energy scans at 4 impact positions for electron and pion beams are analyzed. These positions are labeled D, E, H, & I, and are presented in Table 2.1 where x is measured from the center of the cryostat and y is measured from the beam's nominal impact position. Figure 2.11 shows the geometrical layout of the impact positions.

Impact positions D & E (H & I) belong to different modules but are identical in every other way. Positions D & E differ from positions H & I in that the pads are traversed by a tie rod which holds the layers of the calorimeter in place.

The signal from each readout cell for each event is recorded every 25 ns for a total of 400 ns providing 16 time slices. Figure 2.12 shows an average signal shape from a data sample. The first 4 time slices are read before the signal begins, while the signal maximum typically occurs in the 8th time slice. The energy deposited in each cell is reconstructed from the signal maximum. In the analyses that follow optimal filtering is used to determine this maximum unless stated otherwise. This

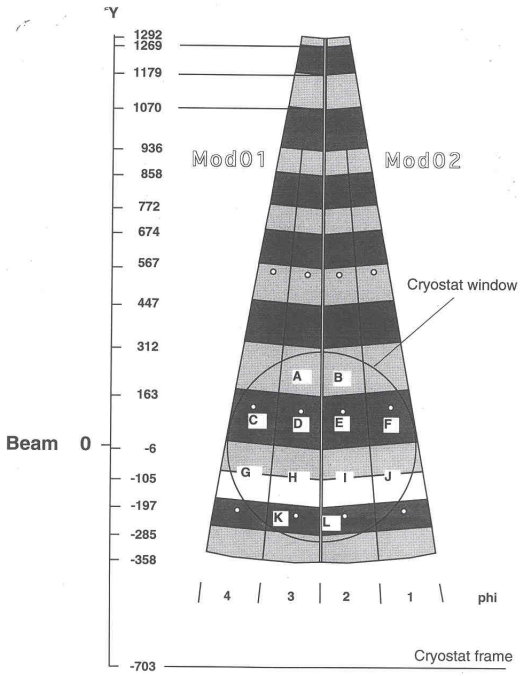

Figure 2.11: The geometric layout of impact positions D, E, H, & I on the front face of HEC modules. The y-axis units are mm.

and other maximum finding methods are described in Section 2.4.3.

The pedestals for each cell are determined from the first four time slices averaged over all events within the run [4], as shown in Figure 2.12. On an event by event basis the average of the first 4 time slices is observed to be stable over the duration of a run.

2.4.3 Signal Reconstruction

Since the standard HEC beam test readout contains 16 time slices for each channel for each event, it is necessary to define a method for reconstructing the maximum signal. Two different methods of signal reconstruction have been compared in detail (see [25]). The first is a simple cubic interpolation using 4 time slices near the maximum. This is one of the methods available in the `hec_adc` beam test software

[4]The use of run pedestals in lieu of event pedestals (defined as the average of the first 4 time slices for each event) provides higher statistics and hence a more precise knowledge of the pedestals for each cell.

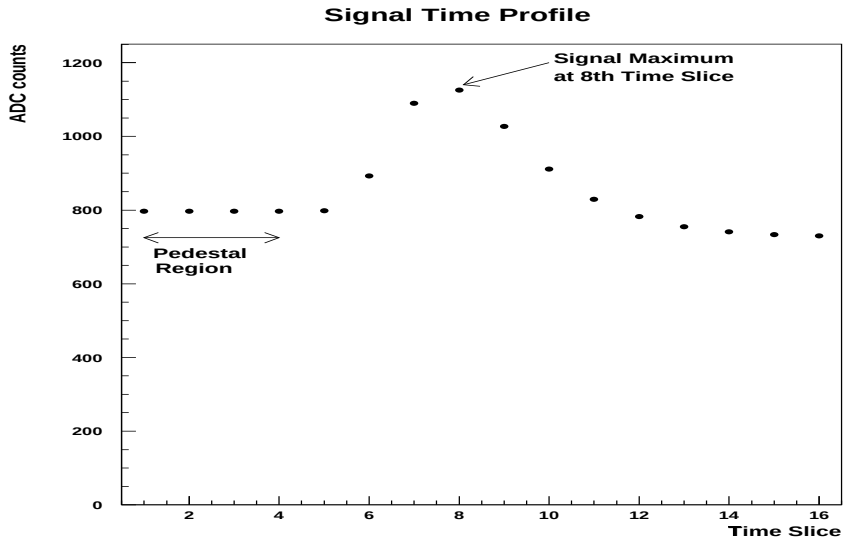

Figure 2.12: Sample signal time profile (average signal for run 7355, 180 GeV pions, impact position D) showing the pedestal region (time slices 1-4) and the signal maximum which typically occurs at time slice 8. The time slices correspond to 25 ns bins.

package and is described in detail in [26]. The second method, also available in the `hec_adc` package, uses an optimal filtering technique to perform the reconstruction. This technique, as explained in references [27, 28], uses the autocorrelation function of the time slices to maximize the signal to noise ratio for the determination of the time origin and amplitude of the signal. Throughout this analysis (unless stated otherwise) the optimal filtering signal reconstruction method is used[5].

2.4.4 Performance for Electrons

In the work that follows, the performance of the Hadronic Endcap Calorimeter modules is evaluated using electron data. Electron runs were obtained at 20, 40, 60, 80, 100, 119.1 GeV incident beam energy. The emphasis of this analysis is on obtaining the energy resolution and linearity of the HEC for electrons, and to evaluate the electromagnetic energy scale of the calorimeter. In the sections that

[5]For April 1998 data 4 cells did not have optimal filtering coefficients due to hardware problems. Cubic interpolation was used for these cells.

follow, the steps used in signal isolation and energy reconstruction are described in detail as are the final results of the analysis.

Trigger Cuts

In order to ensure that the electron sample is pure, several trigger requirements are imposed on the data set. This is done using several dedicated trigger detectors described in Section 2.4.1. The first condition is that there is a signal in the B1, F1 and F2 detectors upstream of the cryostat (pre-trigger, T). The second and third requirements are vetoes to remove other particle species from the data sample. One requires that there are no hits in the muon chambers downstream of the cryostat (muon tag trigger, M). The other ensures that there is no "halo", ie. particles from the periphery of the beam, striking the VM and hole counters (halo trigger, H). Finally, the events must not be recorded when two events overlap too closely in time (pileup, P) or when the recorded event is the result of a random trigger (R). Random trigger events are recorded between physics events or in data taking periods when there is no particle beam. These data are recorded to independently assess the electronic noise present in the detector.

These conditions can be summarized succinctly as:

$$T \bullet \overline{H} \bullet \overline{M} \bullet \overline{P} \bullet \overline{R} \tag{2.11}$$

where

$$T = B1 \bullet F1 \bullet F2, \qquad H = VM + hole, \qquad M = M1 \bullet M2 \tag{2.12}$$

and where $\bullet$ represents a coincidence, "AND", and $+$ represents an "OR".

Clustering

The energy of the incident electrons is reconstructed by summing the individual energies deposited in a cluster of 9 cells after applying hardware calibration constants. The cluster size and shape have been chosen so as to achieve full containment of

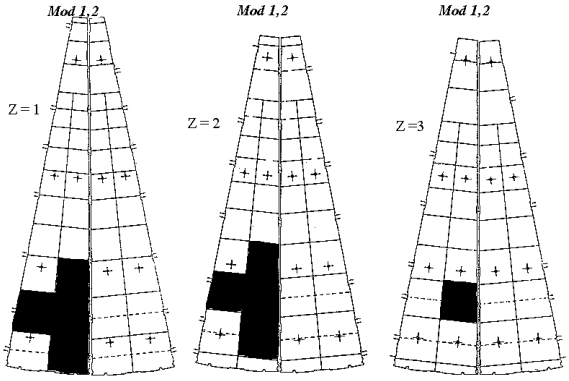

Figure 2.13: The three depth compartments for the tested modules. The darkened cells represent the cells included in the cluster to reconstruct electron energy for impact position H.

electromagnetic showers. Figure 2.13 shows the clusters chosen for 1 of the 4 impact positions.

The energy deposited in each cluster follows the expected normal distribution. Histograms and fits in a 2.5σ range about the mean for a representative impact position (H) are shown in Figure 2.14. The mean (μ) and width (σ) used in this analysis are taken from these histograms.

Global Electromagnetic Scale, α_{em}

A single constant, α_{em}, is used to convert the energies from nA to GeV. This global electromagnetic scale is determined for each impact position by simply dividing the beam energy by the mean reconstructed energy, μ (in nano-amperes), obtained from the histograms described in the previous section. An average over the beam energies at a given impact position is then used as the scale for the cluster. The error on this value is estimated from the rms deviation of the values at different energies for that beam position. The values of α_{em} for the four studied impact positions are presented in Table 2.2.

By applying α_{em} to the fit mean energy for each run, a response curve is obtained, Figure 2.15. The response is linear to within 1% over all impact positions in the studied energy range.

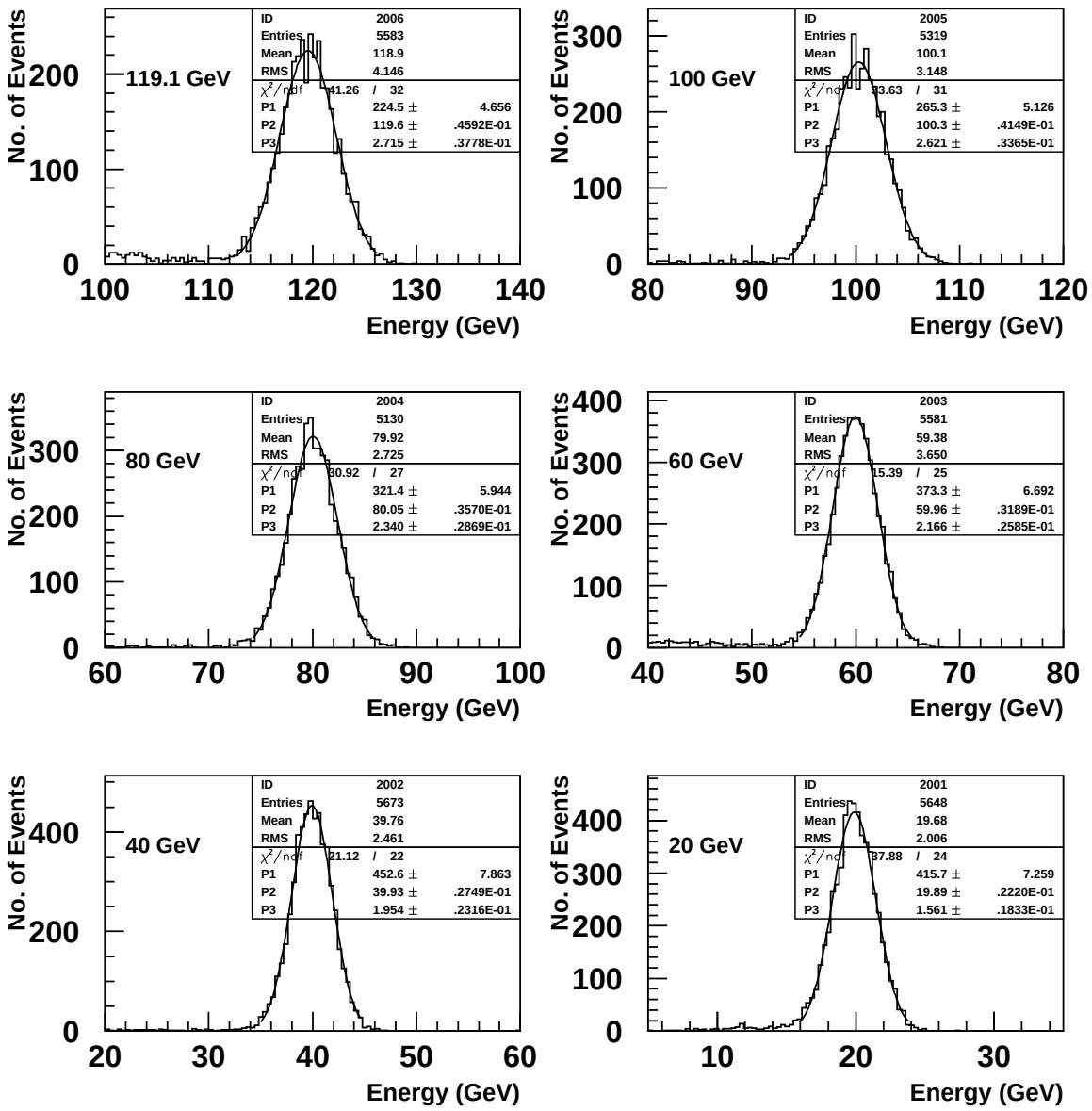

Figure 2.14: Electron cluster energy distribution for a typical impact point(H) for energies 119.1, 100, 80, 60, 40 and 20 GeV. A small amount of pion contamination can be seen in the 119.1 GeV data. The horizontal scale on these histograms is obtained using a global electromagnetic scale as described on page 44.

Impact Position	α_{em} (GeV/μA)
D	3.211 $\pm$ 0.008
E	3.171 $\pm$ 0.008
H	3.190 $\pm$ 0.010
I	3.211 $\pm$ 0.008

Table 2.2: The electromagnetic scale calculated for each of four beam impact positions.

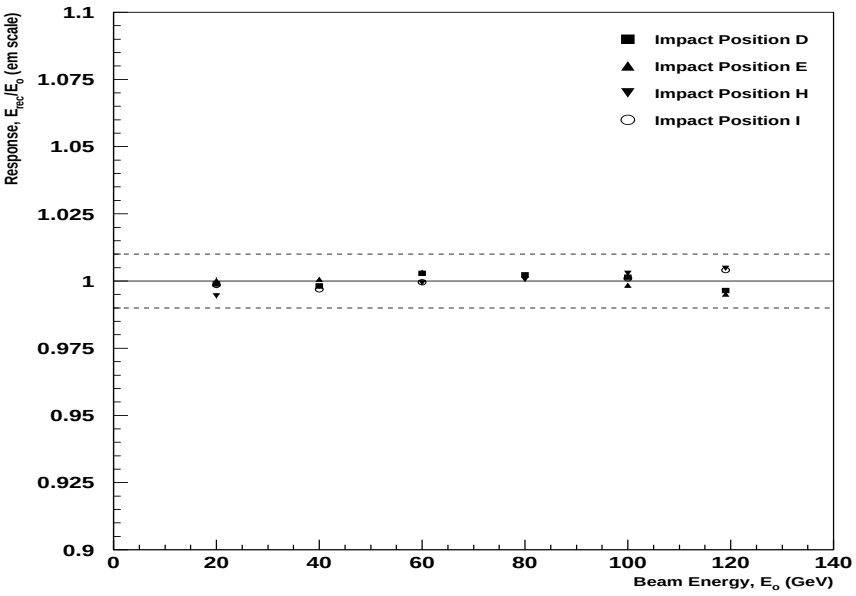

Figure 2.15: Electron response of calorimeter vs. beam energy. The dashed lines represent a variation of 1%. Response is shown to vary less than 1% over the studied energy range.

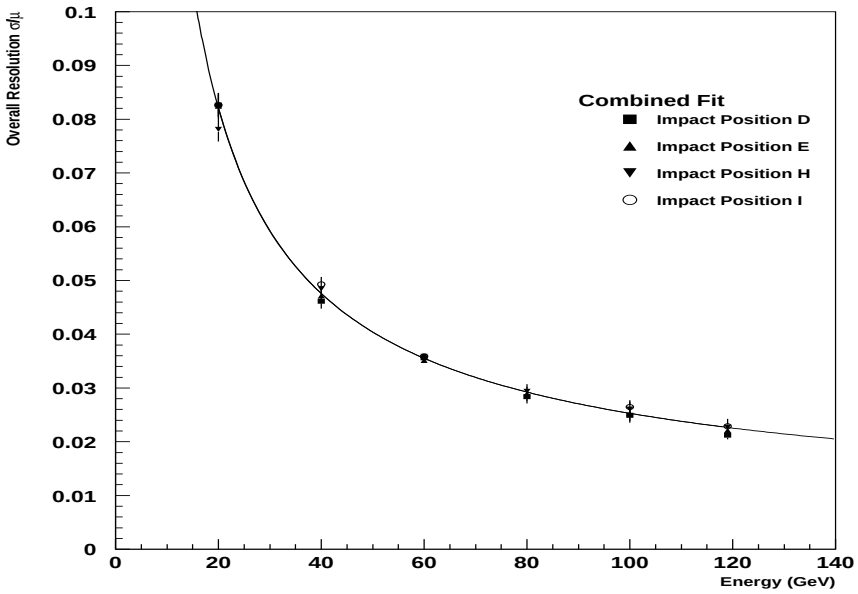

Figure 2.16: Electron energy resolution with 3 free parameters. This is a combined fit using data from 4 different beam impact positions. Error bars are calculated from RMS deviation of the resolution at the four impact positions.

Electron Energy Resolution

The energy resolution σ/E is plotted versus the beam energy in Figure 2.16. The resolution of the calorimeter is parameterized as:

$$\frac{\sigma}{E} = \frac{A}{\sqrt{E_0}} \oplus B \oplus \frac{C}{E}, \tag{2.13}$$

where σ is obtained from the fits presented in Figure 2.14, the first term on the right is the sampling term, the second is the constant term, and the third is the electronic noise term. The results of the fit for each impact position with all three parameters left free are presented in Table 2.3. For these individual fits the error bars at each energy are purely statistical. The results are consistent over all impact positions. A combined fit produces the following result:

$$\frac{\sigma}{E} = \frac{(21.5 \pm 0.4)\%}{\sqrt{E_0}} \oplus (0.0 \pm 0.4)\% \oplus \frac{1.33 \pm 0.04}{E}, \qquad \frac{\chi^2}{\text{ndf}} = 15.4/20 \tag{2.14}$$

Position	$A(\%\text{GeV}^{\frac{1}{2}})$	$B(\%)$	$C(\text{GeV})$	χ^2/ndf
Module 1				
D	20.2 ± 0.4	$0. \pm 0.4$	1.38 ± 0.03	12.6/3
H	22.8 ± 0.3	$0. \pm 0.3$	1.22 ± 0.03	10.1/3
Module 2				
E	20.9 ± 2.8	$0.2 \pm 3.$	1.35 ± 0.09	1.4/3
I	22.2 ± 0.4	$0. \pm 0.6$	1.34 ± 0.03	7.0/2

Table 2.3: Resolution results from fits to electron data from each of four beam impact positions.

where E_0 and E are expressed in GeV. The noise term is consistent with noise measurements made on the corresponding clusters using random trigger events. For this combined fit the total error on each point is calculated from the RMS deviation of the resolution at a given energy calculated from the 4 impact positions. This error accounts for systematic errors present in the analysis (statistical error is negligibly small relative to systematic effects).

2.4.5 Performance for Pions

Beam test data provides a unique opportunity to study the intrinsic performance of the hadronic endcap calorimeter. To this end, a detailed analysis of pion response and energy resolution is described herein. Large clusters have been used to achieve nearly full containment. The electronic noise from these clusters is independently evaluated and subtracted to reveal the intrinsic resolution of the calorimeter. A detailed measurement of the intrinsic e/h of the calorimeter is also presented.

Pion Sample

In order to remove impurities in the pion sample (eg. muons), several trigger cuts are used. These cuts have been described in detail for the electron analysis (Section 2.4.4) and include a physics trigger requirement and a muon, pileup and random veto. To reduce muon contamination in low energy pion data a signal shape cut is also used. This cut requires that at least one cell in the pion cluster contains a time

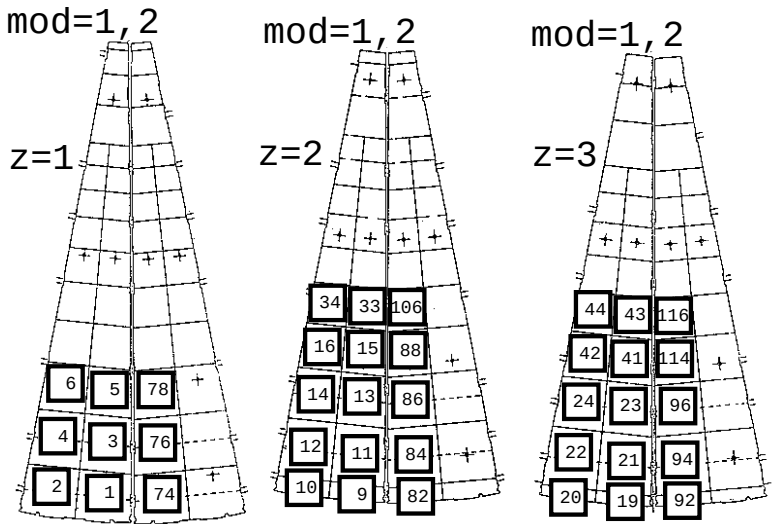

Figure 2.17: Map of 39 cell cluster used for pion data analysis at impact position H. Shown are the three readout depths. The outlined cells correspond to the 39 cell cluster used to reconstruct pion energy at this sample impact position. The numbers on the cells correspond to electronic channel numbers and are irrelevant for this discussion.

profile consistent with signal in that cell. The number of pion events satisfying these cuts ranges from approximately 4000 to 9500 for the 40 to 180 GeV runs, and 350 to 450 events for the 20 GeV runs. The 20 GeV runs were of low rate, so little data exists for this energy.

Energy Reconstruction

For the purpose of evaluating the intrinsic performance of the calorimeter, it is necessary to use clusters that achieve nearly full containment of hadronic showers. For this reason 39 cell clusters are used to reconstruct pion energy. The 39 cell clusters are chosen on a geometrical basis, though in general the chosen cells are those with the highest mean energy. A comparison of various cluster sizes is presented starting on page 56. A sample cluster for impact position H is shown in Figure 2.17.

The performance of the hadronic endcap calorimeter is evaluated using simple depth constants. These constants are not designed to optimize resolution, rather

readout segment	$C_{z,1}$	$C_{z,2}$
z=1	1	1
z=2	1	1
z=3	2	2.67

Table 2.4: Simple depth constants used to reconstruct pion energy are tabulated.

they are intended to provide a constant sampling fraction in the three readout segments of the calorimeter. This is necessary due to the increase in thickness in copper plates in the second wheel (third longitudinal readout segment) of the calorimeter. This change in copper thickness necessitates the application of a factor of two to the signal read out in the rear compartment. A small modification of this scheme is introduced for module 2 in order to correct a high voltage problem in the rear of that module. Since only 3/4 of the sub-gaps were functioning in the first half of the readout segment[6] a corrective factor of 4/3 is applied to the third readout segment of this module (ie. the depth constant is 2.67 times the first two constants).

The signal in each cell of the cluster is summed (weighted by the appropriate simple depth constant) to reconstruct the particle energy in nA for each event:

$$E_{\mathrm{cl}} = \sum_{z} \sum_{m} (C_{z,m} E_{z,m}) \tag{2.15}$$

where $E_{z,m}$ is the energy (in nA) in all cells in the chosen cluster that are in a particular depth (z) and module (m). The simple depth constants are shown in Table 2.4.

The hadronic scale constant (α_{had}) needed to convert E_{cl} to GeV is found by minimizing:

$$\sum_{\mathrm{i}} \frac{\left(\alpha_{\mathrm{had}} \left\langle E_{\mathrm{cl,i}} \right\rangle - E_{0,i}\right)^2}{\sigma_i^2} \tag{2.16}$$

where the sum is over data runs at different energies for a given impact position and $E_{0,i}$ is the known beam energy. $\left\langle E_{\mathrm{cl,i}} \right\rangle$ and σ_i are the mean and width obtained from a Gaussian fit to the distribution of E_{cl}.

[6]The second half of the readout segment contains little energy and so is ignored in this assumption.

Impact Position	Average Electronic Noise (GeV)
D	6.30 ± 0.08
E	5.81 ± 0.06
H	5.73 ± 0.07
I	5.52 ± 0.07

Table 2.5: The average electronic noise measured in the 39 cell clusters for each of four beam impact positions. The average noise is calculated from a weighted average of the noise found in each run at that position (each measurement is weighted by the number of events in that run).

The results of this energy reconstruction are shown in Figures 2.18 and 2.19. These distributions show the expected Gaussian shape.

Electronic Noise Evaluation

In order to evaluate the electronic noise in each cluster, the reconstructed energy of the cluster (including simple depth constants) is measured for random trigger events. Random trigger events are events which are recorded at random times when there should not be any signal in the detector. The distributions obtained from this method are centered on zero and the rms deviation is used as a measurement of electronic noise. This measurement implicitly includes all correlations between individual cells. For 39 cell clusters at impact positions D, E, H and I the average noise is listed in Table 2.5.

Response to Pions

The response to pions over the energy range 20 to 180 GeV is shown in Figure 2.20. The left axis shows the response plotted on an electromagnetic scale (α_{em}) which contains information about the degree of non-compensation in the calorimeter (i.e. intrinsic e/h). The right axis shows the response using a global hadronic scale obtained from Equation 2.16. The shape of the response curve is as expected for a non-compensating calorimeter with intrinsic e/h greater than one. A measurement of the e/h ratio for this calorimeter is presented in Section 2.4.6.

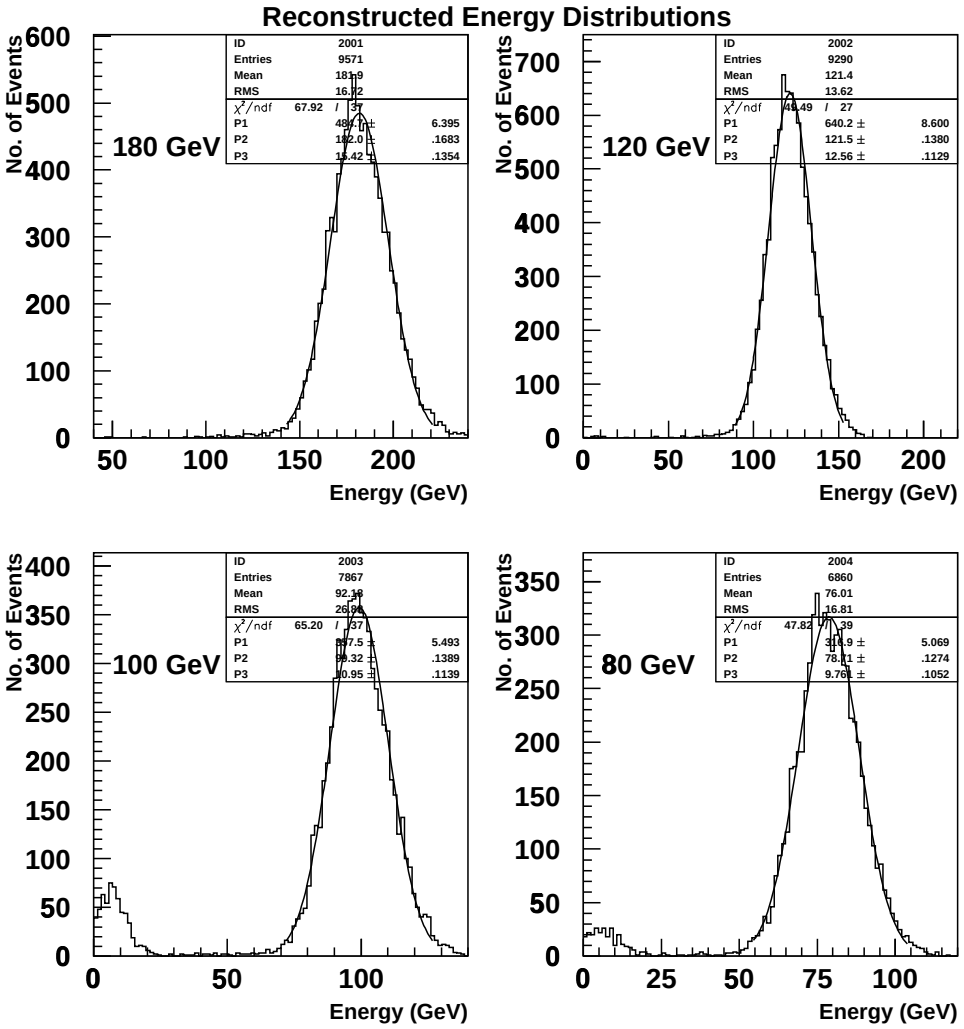

Figure 2.18: Pion cluster energy distributions for a typical impact point (H) after cuts and application of simple depth constants, beam energies 80 to 180 GeV. Muon contamination in the sample due to inefficiencies in the trigger and signal shape cuts can be observed at low energy, particularly for the 80 and 100 GeV runs.

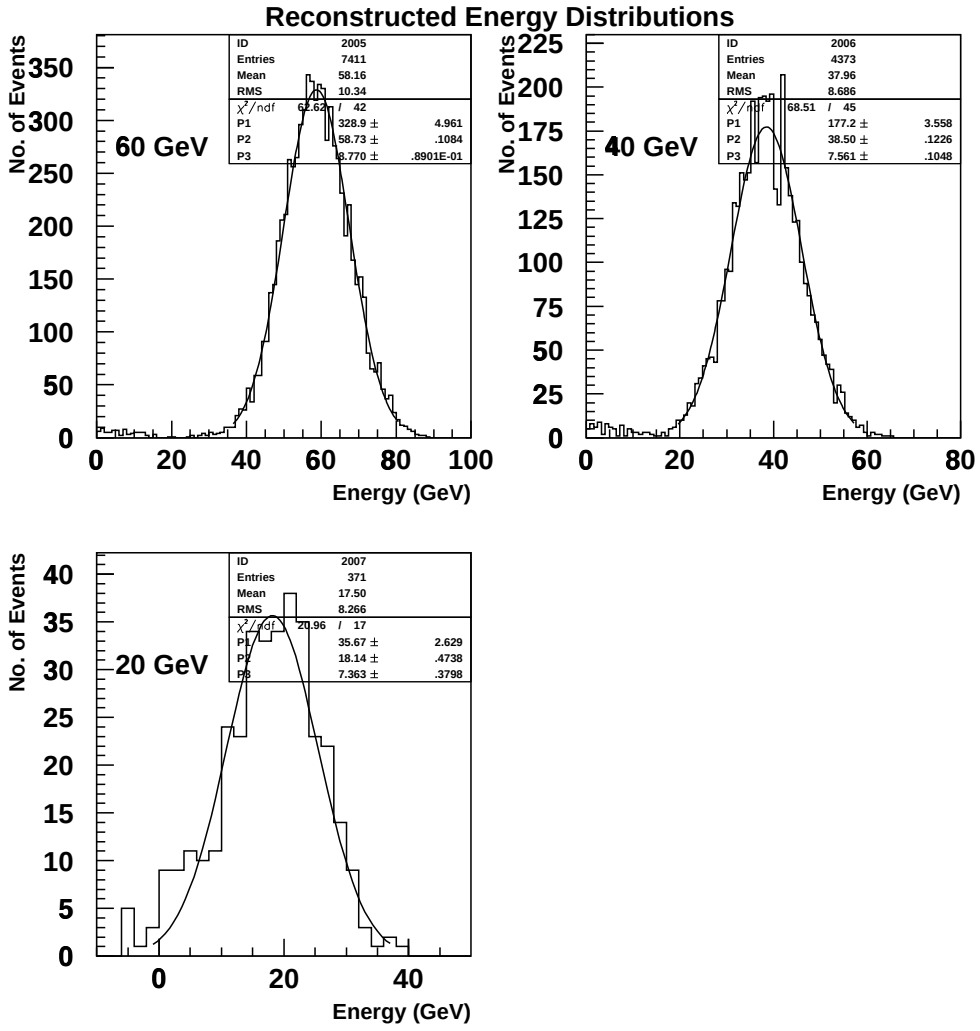

Figure 2.19: Pion cluster energy distributions for a typical impact point (H) after cuts and application of simple depth constants, beam energies 20 to 60 GeV. Muon contamination in the sample due to inefficiencies in the trigger and signal shape cuts can be observed at low energy for each distribution.

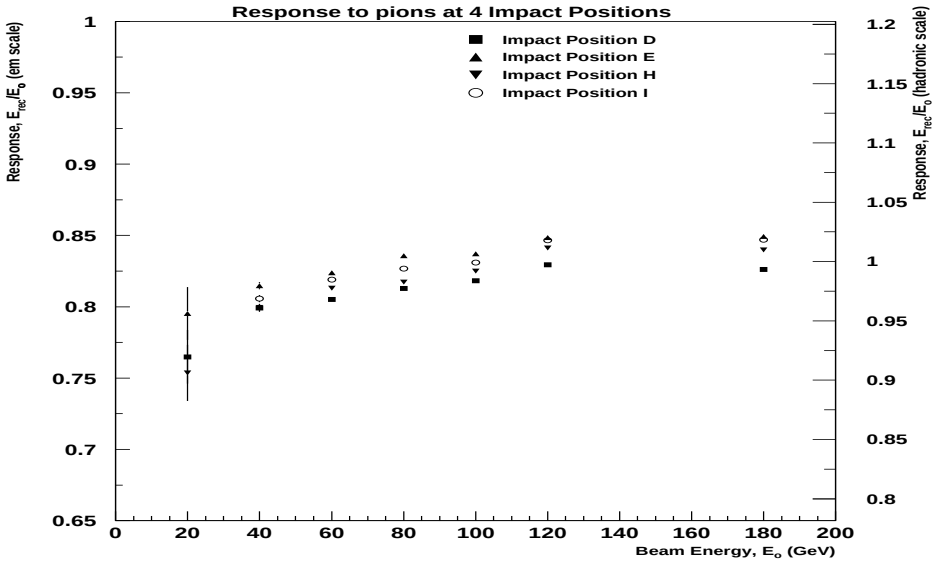

Figure 2.20: Pion response vs. energy is shown with two vertical scales. The scale on the left uses the electromagnetic scale constant (α_{em} as determined from electron data) while the scale on the right uses the hadronic scale constant (α_{had} as determined from pion data).

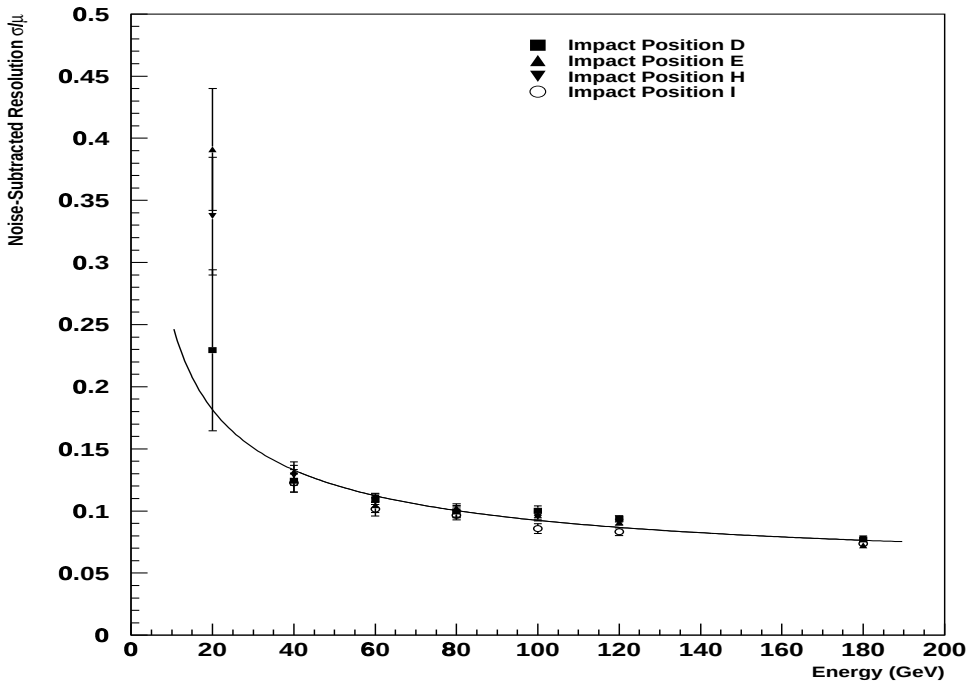

Figure 2.21: Intrinsic energy resolution for four impact positions for a 39 cell cluster and simple depth constants. The combined fit curve is shown.

Pion Energy Resolution

As discussed previously (Section 2.4.5), the electronic noise in a cluster of cells can be independently measured using random trigger events. Once this has been measured for a given cluster its influence can be removed and a parameterization of the intrinsic resolution can be obtained in the form:

$$\frac{\sigma}{E} = \frac{A}{\sqrt{E_o}} \oplus B \tag{2.17}$$

where the first and second terms can be interpreted as a sampling and constant term respectively.

Figure 2.21 shows the noise-subtracted resolution as a function of energy for 4 different impact positions for a 39 cell cluster and simple depth constants. Consistency between impact points is evident despite the high voltage problems in one of the modules. The adjustment of the simple depth constants effectively compensates for the loss of signal.

Position	$A(\%\ \mathrm{GeV}^{\frac{1}{2}})$	$B(\%)$	χ^2/ndf
Module 1			
D	76 ± 5	5.7 ± 0.5	9.5/5
H	77 ± 4	5.4 ± 0.4	13.4/5
Module 2			
E	85 ± 4	3.8 ± 0.7	26.3/5
I	70 ± 4	5.2 ± 0.4	0.9/4

Table 2.6: Resolution results of fits to pion data at each of four different beam impact positions.

The results of fits to data for each of the four impact positions are shown in Table 2.6. A combined fit of equation 2.17 to the energy resolution data for 4 impact positions yields the result

$$\frac{\sigma}{E} = \frac{(78 \pm 2)\%}{\sqrt{E_o}} \oplus (5.0 \pm 0.3)\%, \qquad \frac{\chi^2}{\mathrm{ndf}} = 74.5/25$$

where E_o is in GeV. The high value of the χ^2/ndf is driven by the data at impact position E. These results were obtained using a Gaussian fit which ranged $\pm 2.5\sigma$ from the mean. Results for 2σ and 3σ fits have also been obtained and lead to very similar resolutions at all beam energies with sampling and constant terms consistent with these results within error.

Effect of Cluster Size on Overall Resolution

The overall pion energy resolution of the calorimeter differs from the intrinsic resolution presented in the previous section in that it includes a contribution from electronic noise (ie. noise is not quadratically subtracted before resolution is calculated). The number of cells used in a cluster will influence the measured overall energy resolution of the calorimeter since increasing the cluster size will increase the electronic noise contribution. However, a cluster which is too small will exclude a significant fraction of the pion energy, effectively creating leakage and degrading the sampling and constant terms of the resolution. A compromise must be made which finds the optimum overall resolution.

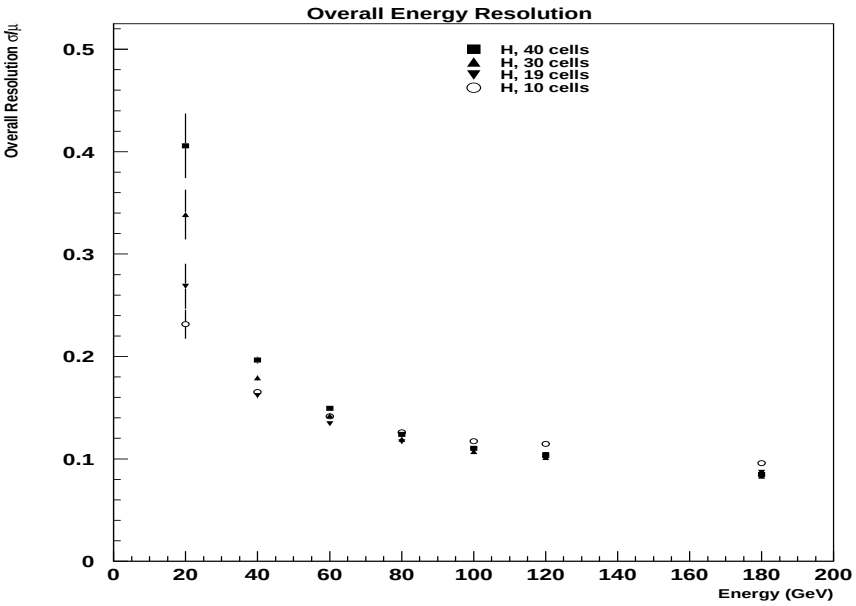

Figure 2.22: Comparison of overall energy resolution (ie. including electronic noise) for four different cluster sizes for pions at position H (simple depth constants).

Figure 2.22 shows a comparison of energy resolution for 4 different cluster sizes for position H. These clusters range from a small cluster of 10 cells to a large 39 cell cluster. The cells chosen for a particular cluster are those which contain the highest mean energy. The clusters for various impact positions are observed to follow the same basic geometrical pattern. The results show that the best overall resolution is obtained by a cluster containing 19 cells (18 for impact position I). Clusters larger than 19 cells do not improve the resolution at high energies. This implies that the reduction in the contribution from leakage is smaller than the added contribution from electronic noise for clusters of more than 19 cells. Reducing the cluster size below 19 cells (eg. 10 cells) does not improve the resolution at low energies where the noise term takes on added significance. A sample 19 cell cluster for impact position H is presented in Figure 2.23. If it were not possible to make an independent measurement of electronic noise a 19 cell pion cluster would be preferred to the 39 cell cluster used in the previous section.

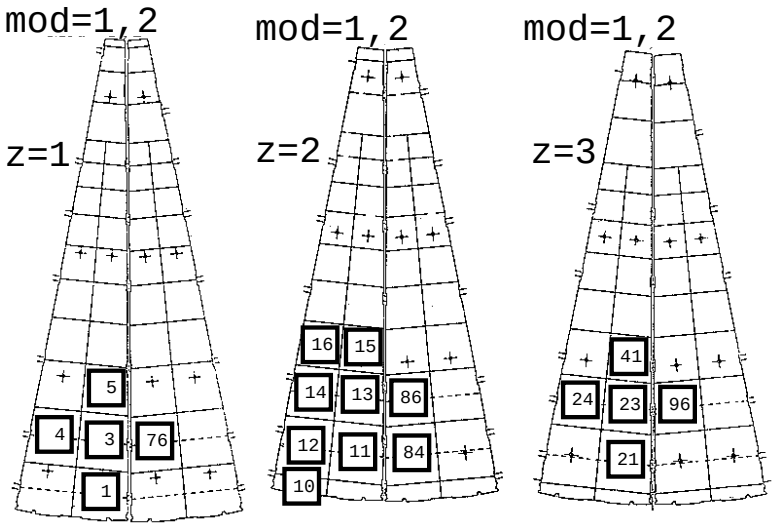

Figure 2.23: Map of optimized 19 cell cluster used for pion data analysis at impact position H. Shown here are the cells in each of the three readout depths. The outlined cells correspond to the cells used to reconstruct the pion energy. The numbers on the cells represent electronic channel numbers and are irrelevant to this discussion. The clusters for other impact positions follow the same basic pattern.

Optimization of Overall Resolution Using Energy Dependent Weights

The fraction of energy deposited electromagnetically (versus hadronically) varies with beam energy in a pion shower. Since the HEC is intrinsically non-compensating, the overall pion resolution can be improved by applying depth weights that vary with energy.

Energy dependent depth weights, w_z, for each impact point were obtained by minimizing the function:

$$\chi^2 = \frac{1}{\sigma^2} \sum_{\text{events}} \left(\alpha_{\text{had}} \sum_z w_z E^z_{\text{cl}'} - E_0 \right)^2 \tag{2.18}$$

where the outer summation is over all events that lie within 2.5σ of the mean, the inner summation is over the three readout segments of the calorimeter, α_{had} is the hadronic scale found for the 39 cell cluster, E_0 is the beam energy, $E^z_{\text{cl}'}$ is the energy in readout segment z with simple depth constants applied, and σ is the reconstructed width of the energy spectrum with energy dependent depth weights applied. The minimization procedure produces a χ^2 per degree of freedom near one for all impact

positions.

At low energies very little signal reaches the second and third readout segments making this procedure ineffective. Hence, this depth weighting procedure has not been used at 20 GeV.

The energy dependent depth weights can be scaled so as to produce a response of 1 at all energies. This scaling does not affect the resolution in any way. Figure 2.24 shows the effective depth weights (the energy dependent depth weights multiplied by the simple depth constants, with this product scaled to give a response of 1) for a representative impact point in each of modules 1 and 2. Note that the two modules share the same energy dependent depth weight for each readout segment for each energy, but the effective depth weight for each module may differ, since the simple depth constants for the two modules are not necessarily the same (i.e. due to HV problems in the 3rd readout segment).

It should further be noted that this procedure minimizes the *overall* resolution (ie. including electronic noise). It does not serve to minimize the individual parameters of a resolution parameterization such as equation 2.17. Thus, the overall resolution will improve with the application of energy dependent depth weights, but a parameter such as the sampling term *will not necessarily improve.*

The energy dependent depth weights can be used to check the validity of the simple depth constants. If these constants are incorrect, the minimization procedure would produce energy dependent depth weights which shift the effective depth weights significantly away from the original depth constants at all energies. From this minimization procedure factors of 1 are preferred for the first 2 readout segments of both modules, while a factor of 2 is preferred for the 3rd readout segment of module 1 and a factor of roughly 2.67 is preferred for the 3rd readout segment of module 2 (affected by HV problems). The effective depth weights follow the expected behavior, justifying the naive assumptions used to calculate the simple depth constants.

The overall resolution is evaluated using the optimized energy dependent depth

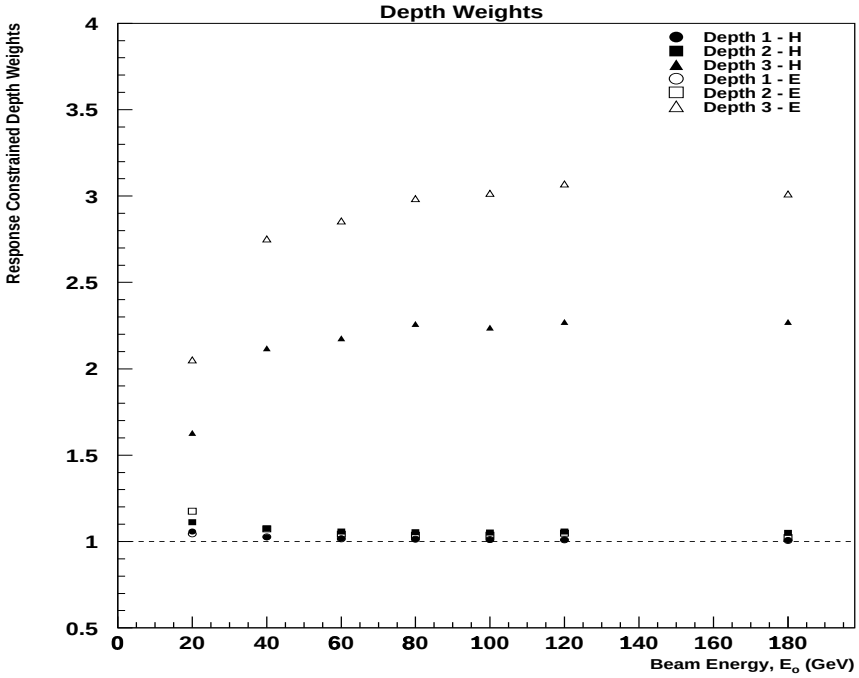

Figure 2.24: Effective depth weights (energy dependent depth weights multiplied by simple depth constants scaled to give unit response) for two representative impact points. The weights presented for impact point H(E) are for module 1(2). The difference between the third depth weight in module 1 and the third weight in module 2 (solid and empty triangles) is explained by the high voltage problems in module 2.

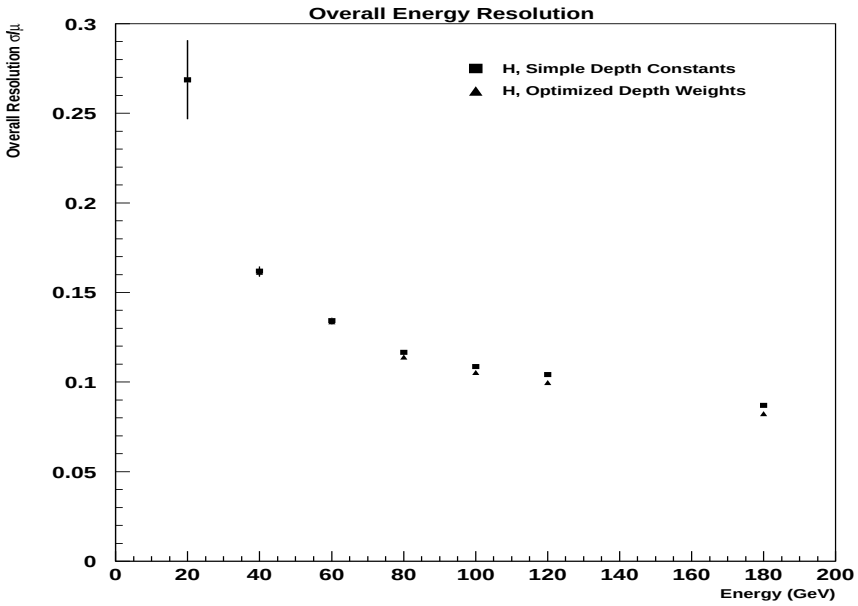

Figure 2.25: Overall resolution for 19 cell cluster using simple and optimized energy dependent depth weights.

weights and the optimized 19 cell cluster and is presented in Figure 2.25. A plot of the overall resolution using simple depth constants is superimposed. The use of optimized energy dependent depth weights produces a noticeable improvement in overall resolution at higher energies. However, the effect on the parameterization of the resolution is negligible. For simplicity, this method is not used to obtain final resolution results.

2.4.6 Measuring e/h

As described in Section 2.2, one of the fundamental parameters which defines the intrinsic performance of an hadronic calorimeter is the ratio of its electromagnetic to hadronic response. This is referred to as the e/h ratio of the calorimeter.

The e/h ratio of a calorimeter cannot be directly measured. Given measurements of the ratio of the pion and electron response as a function of energy (e/π curve),

its value can be extracted via the relation

$$\frac{e}{\pi} = \frac{\frac{e}{h}}{1 - (1 - \frac{e}{h}) f_{\pi_o}(E)} \tag{2.19}$$

where f_{π_o} is the fraction of shower energy dissipated through π_o production. As described in Section 2.1, π_o's will decay almost exclusively to two photons and are responsible for the creation of electromagnetic sub-showers within hadronic showers. Two common parameterizations of the energy dependence of this fraction are logarithmic [17]

$$k \log \frac{E}{E_h} \qquad \text{(Wigmans)} \tag{2.20}$$

and power law [18]

$$1 - (E/E_h)^{m-1} \qquad \text{(Groom)}. \tag{2.21}$$

It is also possible to extract the intrinsic e/h from data using only pion data, allowing the electromagnetic response to vary as a free parameter. This takes the form:

$$\pi = \frac{e}{e/h}(1 - (1 - e/h) f_{\pi_o}(E)) \tag{2.22}$$

Since good quality data exists for electrons in the HEC, the e/π method will be used to extract the intrinsic e/h of this detector.

Experimental Effects

The parameterizations of e/h provided in the previous section do not take into account certain experimental factors which will affect the measurement. The most important of these factors is that of containment. The formulae relating e/π to e/h assume that the shower being measured is fully contained by the calorimeter (ie. there is no leakage). In reality, the modules tested in the 1998 HEC beam tests did not provide full containment of hadronic showers. Monte Carlo simulations indicate that, although the modules provide good longitudinal containment of hadronic energy, the lateral leakage can be as high as 4% [29](see Figure 2.26). If this effect is not

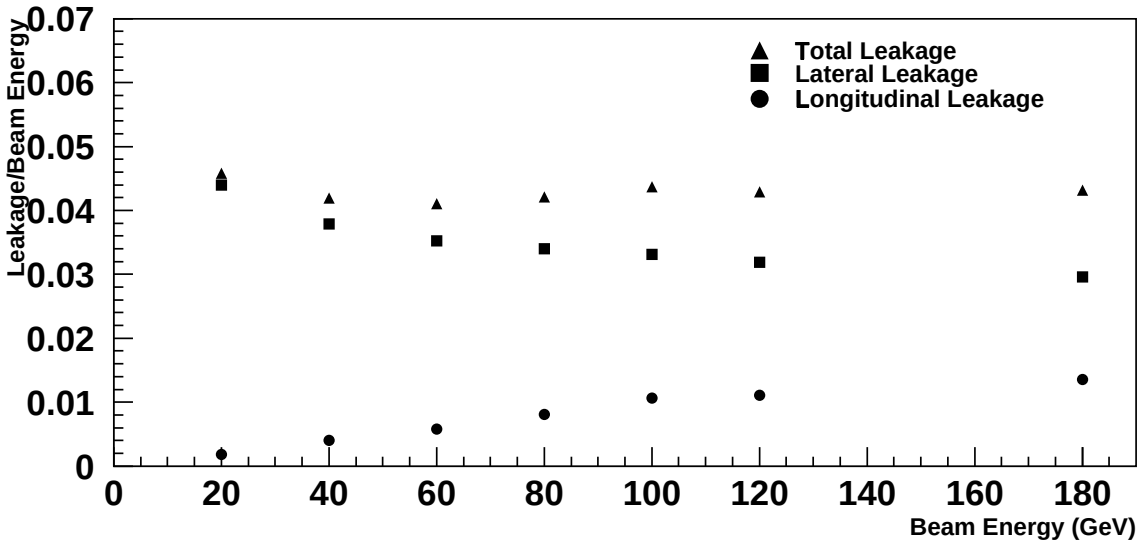

Figure 2.26: The energy dependence of the leakage of pion showers as a fraction of the total energy as predicted by the GEANT-GCALOR [30] Monte Carlo. As expected, the longitudinal leakage is small. The fractional lateral leakage decreases with energy due to the increase in the EM shower component with energy.

taken into account the measured e/π for the calorimeter will be an overestimate, as some energy from hadronic showers is lost while electron showers are fully contained. Figure 2.27 shows the data for module 1 without leakage correction. Fits using both the Groom and Wigmans parameterization (solid and dashed lines) illustrate that without correction the data does not obey the expected energy dependence. In the work that follows these Monte Carlo simulations will be used to estimate an energy dependent leakage correction to be applied to the hadronic response.

Other experimental effects which complicate the e/π (and hence e/h) measurements include effects of low energy cut-off and charge collection time [20]. The energy of hadronic showers is spread over a large number of cells, thus making the signal-to-noise ratio very poor in many of these cells creating an effective low energy cutoff. This cutoff produces an overestimate of the e/π ratio. The second effect is due to the fast-readout design of the HEC and most other hadron calorimeters. Since there is limited time available to readout the signal, the slow component of hadronic showers will be missed. Since no such slow component exists for EM showers this also produces an overestimate of the e/π ratio.

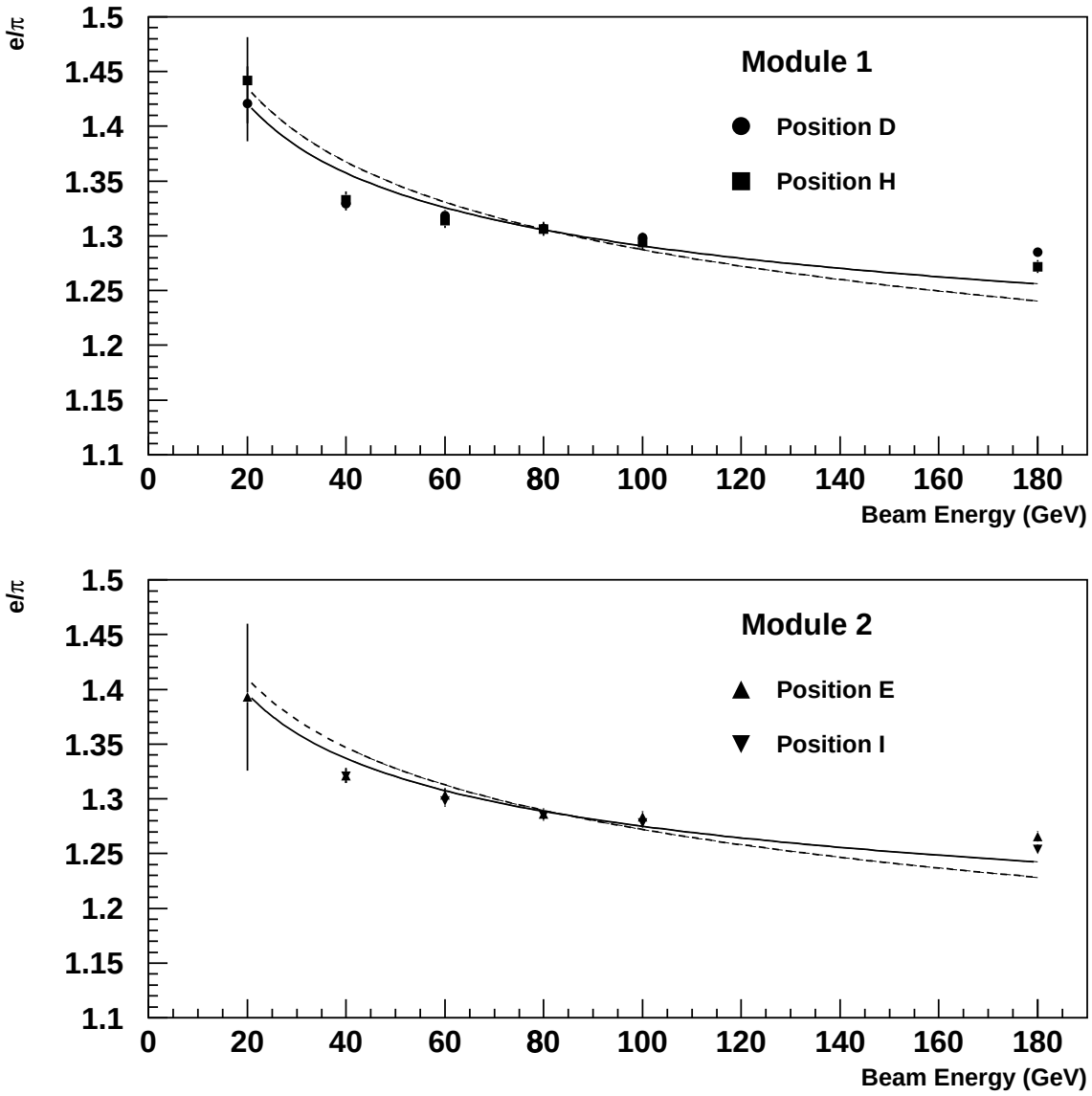

Figure 2.27: The energy dependence of the ratio of the electron to pion response before leakage correction. Data from two impact points within the same detector module are superimposed. The solid and dashed lines refer to fits using the Groom and Wigmans parameterization respectively. This plot shows that without leakage correction the theoretical curves do not fit the data. The χ^2/ndf for the Groom parameterization fits are 88.5/11 and 49.3/10 for modules 1 and 2 respectively. The χ^2/ndf for the Wigmans parameterization fits are 204.5/11 and 142.6/10 for modules 1 and 2 respectively.

Results

In order to calculate the e/π ratio the electron and pion responses are independently measured. The 9 cell electron cluster described in Section 2.4.4 is used to obtain the average electron response. Since the response to electrons is flat to within 1% it is possible to use the average to represent the electron response at all energies. The 39 cell pion cluster described in Section 2.4.5 is used to evaluate the pion response separately at each beam energy. The pion response is then corrected for leakage and the e/π is formed for each beam energy.

The pion shower leakage is estimated using a full simulation of the beam test setup [29]. This simulation keeps track of "leakage" by measuring all particles which escape the beam test modules. Also, the simulation is used to estimate the fraction of energy which leaks out of the 39 cell cluster but is contained within the calorimeter volume. The leakage was estimated with three different Monte Carlo hadronic shower packages (GHEISHA, GFLUKA and GCALOR [30]) and the results were found to be consistent between the three packages. For the results presented here the GCALOR hadronic shower package is used unless otherwise stated. The error on the leakage correction is estimated by comparing the fraction of the initial energy deposited in cells which are far removed from the impacted cell for data and Monte Carlo. The differences between the experimental data and simulation estimates for these distant cells was seen to vary within approximately 30%. Therefore a $\pm$15% error has been assigned to the overall leakage correction.

Since there are small differences between the two modules tested (eg. high voltage problems) the results for each module are fitted separately in Figure 2.28. The results of fits to both the Groom and Wigmans form are shown and good agreement between data and theory is observed. The results of fits with each parameterization are presented in Table 2.7. The results for the Groom parameterization are presented for three values of m, the exponent of the energy dependence of the electromagnetic fraction of hadronic showers. m is considered a constant which is usually measured to be in the range 0.8-0.9. The world-average value for this parameter is 0.83 [31],

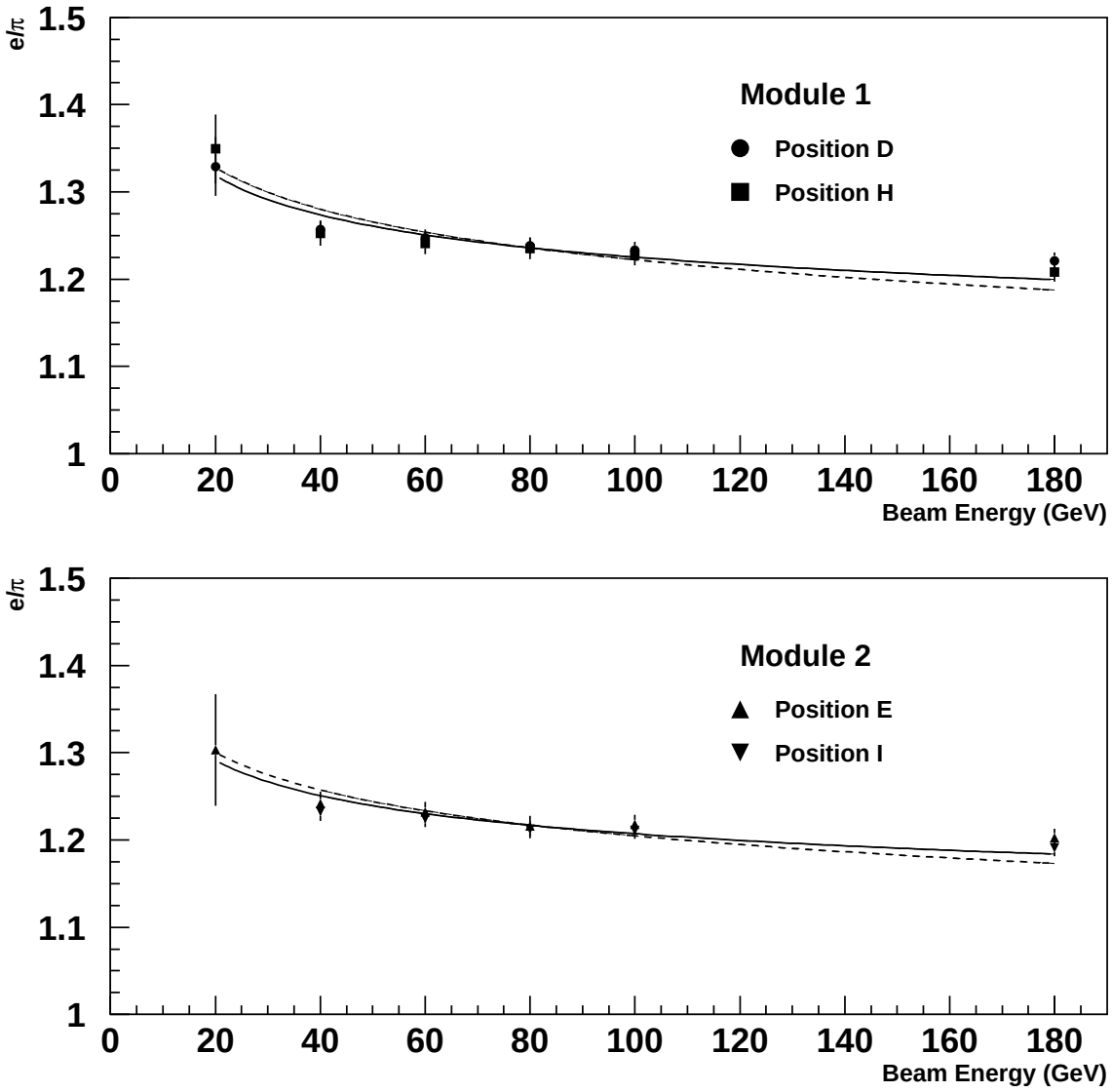

Figure 2.28: The leakage-corrected energy dependence of the e/π ratio is shown for impact positions in module 1 and module 2. Two fitted lines are present on each plot. The solid line represents the fit using the Groom parameterization with m=0.83. The dashed line represents the fit using the Wigmans parameterization with k=0.11. The chi-squared values for these fits are presented in Table 2.7.

		Module 1		Module 2	
		e/h	χ^2/ndf	e/h	χ^2/ndf
Groom	m=0.80	1.84±0.02	1.8	1.74±0.02	1.4
	m=0.83	1.67±0.01	1.1	1.60±0.01	0.77
	m=0.85	1.59±0.01	0.74	1.52±0.01	0.47
Wigmans	k=0.11	1.58±0.01	2.4	1.52±0.01	1.8

Table 2.7: Values of e/h and χ^2 extracted from fits to the Groom parameterization with three different values of m, and Wigmans with one value of k for each HEC module. The number of degrees of freedom in the fits are 11 for module 1 and 10 for module 2.

0.80 and 0.85 are presented to provide a range of values and to allow comparison with published results for other calorimeters. If this parameter is left free in the fit it tends to higher values (≈ 0.9) but this is highly correlated to the e/h ratio and cannot be used to extract a reliable value of e/h. Therefore, only results with fixed m are presented here.

Table 2.7 also shows that using the world-average value for m (0.83) there is a significant difference between the e/h values extracted from the two parameterizations. This difference disappears when the value of m is fixed to 0.85. Despite this, in order to compare with other experiments, the value obtained using m=0.83 is considered the standard result of the Groom fit. When the results from the two modules and two parameterizations are combined the value for e/h for the HEC is measured to be 1.6±0.1. This is in good agreement with the only existing Monte Carlo prediction for the HEC of 1.58 [32].

2.5 Conclusions

The ATLAS Hadronic Endcap Calorimeter (HEC) is a large copper and liquid argon calorimeter designed to operate in a high radiation environment. In 1998 the first modules of the HEC built to the final ATLAS design specifications were tested in particle beams at CERN. A thorough analysis of the performance of the calorimeter modules has been performed with an emphasis on the determination of intrinsic

calorimeter parameters.

The performance of the HEC modules for electrons has been evaluated. While the purpose of the calorimeter is to measure hadronic showers, the electron data allow the measurement of the intrinsic electromagnetic scale of the detector. The electron response was found to be uniform to within 1% over the studied energy range. The resolution for electron energy reconstruction is found to be

$$\frac{\sigma}{E} = \frac{(21.5 \pm 0.4)\%}{\sqrt{E_0}} \oplus (0.0 \pm 0.4)\% \oplus \frac{1.33 \pm 0.04}{E}$$

where E and E_0 are expressed in GeV. These results are in good agreement with expectations.

One of the main goals of this work is to evaluate the performance of the HEC for pion energy resolution and response. A detailed analysis has been performed using various cluster sizes and two depth weighting schemes. The chosen method uses large (39 cell) clusters to provide near-full containment of hadronic showers and simple depth weights to provide a constant sampling fraction over all three depth segments in the calorimeter. The measurement of the pion energy resolution produced by this method is found to be (after subtraction of electronic noise)

$$\frac{\sigma}{E} = \frac{(78 \pm 2)\%}{\sqrt{E_o}} \oplus (5.0 \pm 0.3)\%.$$

An important intrinsic parameter in defining the performance of an hadronic calorimeter is the ratio of its electromagnetic and hadronic responses (e/h). Using measured values of the electron-to-pion response ratio (e/π) the intrinsic e/h of the HEC is determined to be 1.6 ± 0.1 where the error arises primarily from errors in the leakage correction and from systematic errors from the choice of the parameterization of the energy dependence of the electromagnetic fraction (f_{π_0}) of hadronic showers.

Performance for electron and pion reconstruction has been evaluated using data from the April 1998 beam tests. Resolution and response results have been obtained as well as the first estimate of the intrinsic e/h of the calorimeter. It has been shown that the ATLAS Hadronic Endcap Calorimeter performs according to expectations [22].

Chapter 3

Physics of Single Top at ATLAS

3.1 Introduction

Since the discovery of the top quark in 1995 [33] much has been learned about its properties. In fact, as a fraction of its value the top quark mass has the smallest error of any quark mass [13]. To date our direct knowledge of top has come from proton-antiproton collisions at the Fermilab Tevatron [1] producing top quarks via the strong interaction. The production of single top quarks via electroweak interactions has yet to be observed, but promises to provide new opportunities to both test the Standard Model and search for new physics. At the LHC, the predicted cross-sections for such processes are high, making it an excellent laboratory in which to perform single top studies.

Electroweak single top production provides unique opportunities to test the Standard Model. The 3-generation Standard Model makes a precise prediction for the strength of the coupling at the W-t-b vertex ($|V_{tb}|$) from unitarity, given measurements of V_{ub} and V_{cb}. The measurement of the single top cross-section, which is proportional to $|V_{tb}|^2$, is the only way to make a direct measurement of this coupling at a hadron collider. Also, electroweak top production is a source of highly polarized top quarks. The Standard Model makes precise predictions of the polarization of these quarks and since top decays before it can hadronize, measurable effects of the

[1] The Tevatron collider located at Fermi National Accelerator Laboratory (Fermilab) is currently the only machine capable of producing top quarks. It is a proton-antiproton collider operating at a centre of mass energy of 1.8 TeV.

polarization are transmitted to its decay products. There is the potential to measure both $|V_{tb}|$ and top polarization at ATLAS.

There are three major production diagrams for single top at the LHC. A detailed discussion of cross-sections will be presented in Section 3.1.1. Separate measurements of $|V_{tb}|$ and polarization may be possible in each of these processes independently. Each measurement is sensitive to different types of "new physics" and is a valuable measurement on its own as well as a valuable cross-check of the other measurements.

This chapter considers the possibility of isolating each of the three single top signals from background in order to obtain independent measurements of $|V_{tb}|$ and top polarization at ATLAS. Each signal must be separated from large top-pair and non-top backgrounds as well as from other sources of single top.

The following sections provide an introduction to the motivation, methods and prospects for measurements of electroweak top production. Section 3.2 then presents a Monte Carlo study of the potential to measure the cross-sections of each single top signal at ATLAS. Section 3.3 describes a study to estimate the sensitivity of the ATLAS experiment to deviations in the expected Standard Model top polarization. Finally, Section 3.4 summarizes the results of the electroweak top studies.

3.1.1 Top Production at Hadron Colliders

The dominant mechanism for top production at the LHC is $t\bar{t}$ production via the strong interaction. Representative leading order diagrams for this process are shown in Figure 3.1. The first of these diagrams provides the dominant contribution to the cross-section at LHC energies, accounting for more than 90% of the cross-section [34]. The second diagram containing two quarks in the initial state dominates $t\bar{t}$ production at current colliders. At low luminosity ($10^{33}\text{cm}^{-2}\text{s}^{-1}$) each LHC experiment will collect $\sim$20000 $t\bar{t}$ events/day, corresponding to a cross-section of $\sim$830 pb (see Table 3.1). This means that the LHC is a "top factory", making possible the measurement of many properties of the top quark. Production of $t\bar{t}$ is also a major

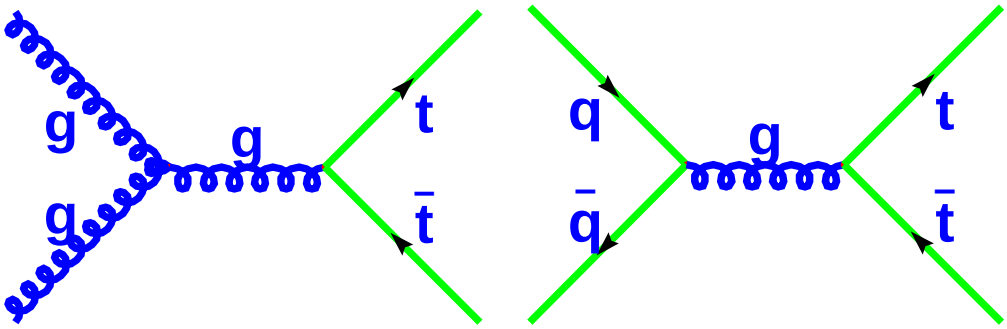

Figure 3.1: Two leading order Feynman diagrams for $t\bar{t}$ production at the LHC. The first diagram containing a 3-gluon vertex is responsible for the dominant contribution to the cross-section. It accounts for more than 90% of the cross-section.

process	total cross-section (pb)
$t\bar{t}$	830 [45]
Wg-fusion	244 [35]
Wt	60
W*	10 [36]

Table 3.1: The cross-sections for the top production processes at the LHC.

background for many physics searches at the LHC such as heavy Higgs boson production. As it will turn out, it is also a significant background for single top studies.

The second largest source of top quarks at the LHC is single top production via Wg-fusion. This process has a predicted rate which is almost 1/3 of the rate of $t\bar{t}$ (see Table 3.1). Due to this high rate the Wg-fusion process has generally been considered the source of most of the physics information which can be extracted from single top events. The tree-level Feynman diagrams responsible for the bulk of the Wg-fusion cross-section are presented in Figure 3.2. The second diagram (the $2\rightarrow2$ process) in Figure 3.2 is actually a subset of the first in which the second (low P_{T}) b-jet has been ignored[2]. The first (the $2\rightarrow3$ process) is more representative of the true physical process at the LHC, however, it suffers from theoretical problems which

[2]Throughout this chapter P_{T} is defined relative to the beam axis.

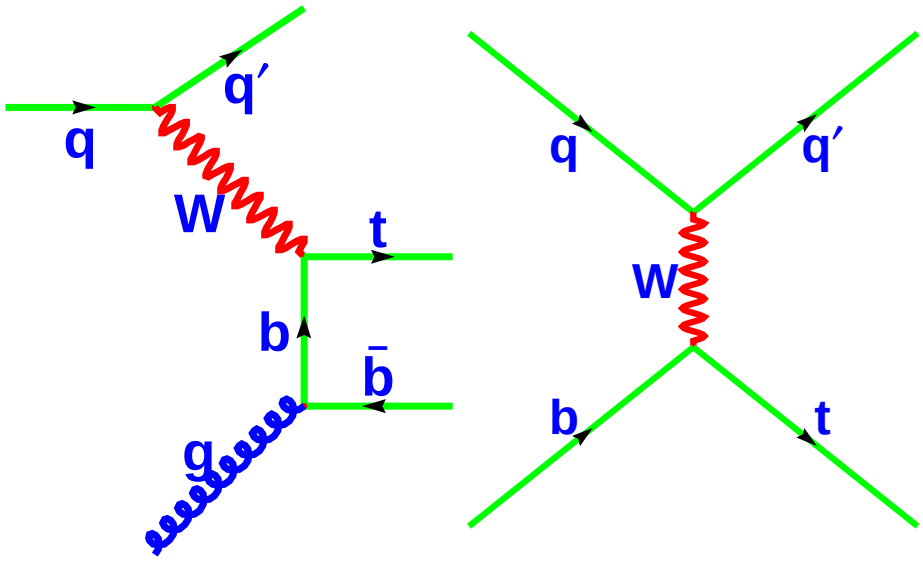

Figure 3.2: Two leading order Feynman diagrams for Wg-fusion production at the LHC. The second diagram is a subset of the first and must be used to calculate the cross-section for the processes in regions of low b-jet transverse momentum (see text for details).

make it difficult to calculate. The cross-section for the 2→3 process becomes infinite in regions of low transverse momentum of the b-quark produced in association with the top. This collinear divergence arises when the $b\bar{b}$ pair from gluon splitting is collinear. For this reason, the 2→2 diagram is often used in calculations and in Monte Carlo event generators. In principle, to get the correct kinematic distributions in Wg-fusion events at leading order it would be necessary to use both diagrams, the 2→2 process in regions of low P_{T} and the 2→3 process in regions of high P_{T} of the b. In practice the matching of these two regimes is very difficult and no Monte Carlo generator exists which properly combines the two. At next-to-leading order (NLO) these problems disappear. The NLO cross-section for this process has been calculated [35] to be 244 pb at the LHC (see Table 3.1).

The Wt process has been largely ignored in the literature because of its very small cross-section at Tevatron energies and topological similarity to $t\bar{t}$ at the LHC. A representative leading order diagram for this process is presented in Figure 3.3. In principle this process should also be drawn as 2→3 and could suffer from the

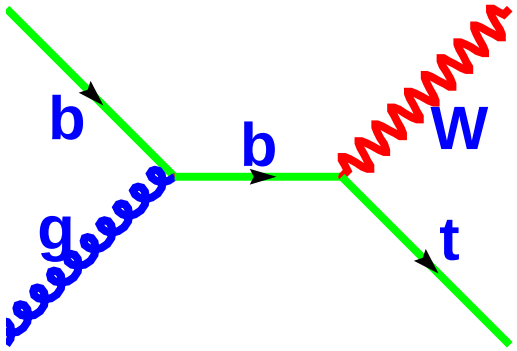

Figure 3.3: A leading order Feynman diagram for Wt production at the LHC.

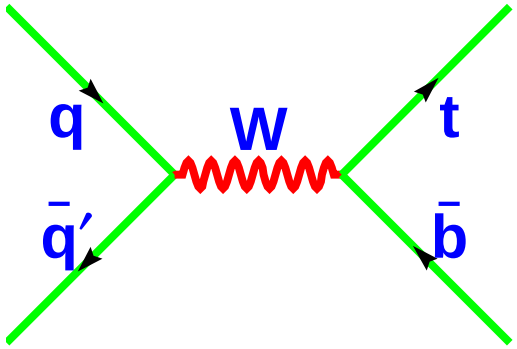

Figure 3.4: A leading order Feynman diagram for W* production at the LHC.

same problems as Wg-fusion for events in which the P_{T} of the b is low. However, for the purposes of this study it will be treated as a 2→2 process. The cross-section calculation for this process exists only to leading order. For this reason the theoretical error on the cross-section is large and for the purposes of this work the cross-section is assumed to be the leading order value of 60 pb at the LHC.

The final top production channel considered here is s-channel single top production, also known as the W* channel. The leading order diagram for this process is shown in Figure 3.4. This diagram does not contain a gluon in the initial state and so does not suffer from complications due to collinear divergences in gluon splitting. The NLO cross-section for this process has been calculated [36] to be 10 pb at the LHC.

Source	W*	W-g
pdf	4%	10%
μ (scale)	4%	10%
ΔM_t	5%	3%

Table 3.2: Sources and levels of theoretical error in the cross-sections of Wg-fusion and W*. The error due to imprecision in the mass of the top is calculated assuming the mass is known to 2 GeV (expected from LHC measurements). In this table pdf refers to the error calculated by choosing different parton density function sets. The μ (scale) refers to the error obtained by varying the renormalization scale at which the calculation is performed [37]. The error in the gluon pdf is from [38], all other numbers are taken from [39].

Sources of Theoretical Error

Table 3.2 shows the sources and levels of theoretical error in Wg-fusion and s-channel single top production. This table illustrates the advantage of the s-channel. Since the cross-section calculation for this process does not rely on gluon parton density functions (pdf) the errors due to pdf uncertainty are significantly lower than for Wg-fusion. The error on the cross-section due to an assumed 2 GeV error on the top mass is higher for W* than for Wg-fusion, but this is outweighed by the advantage in the other sources of error. Another theoretical advantage of W* is that its sources of error can be studied with high statistics at the LHC using Drell-Yan W production, a very similar process.

The theoretical sources of error for the Wt process are not treated here because they are not well known. The cross-section is only known at leading order and no systematic study of the sources of error exists. In this work the theoretical error is assumed to be 50%.

Decay of the Top Quark

The Standard Model prediction of the top quark width (Γ_t) is approximately 1.4 GeV for a 175 GeV top quark [13]. This leads to a prediction for the top lifetime of $\tau = 5 \times 10^{-25}$s. This is shorter than the hadronization time ($\sim 1/\Lambda_{QCD}$), hence the top decays as a "bare" quark.

The low values of V_{td} and V_{ts} will cause the top quark to decay to a W boson and a b-quark nearly 100% of the time. In the Standard Model the predicted branching ratio for t→Wb is 99.9%, for t→Ws is 0.1% and for t→Wd is 0.01%. The high mass of the top quark implies that it will couple to other heavy particles and hence rare top decays are a promising way to search for physics beyond the Standard Model (see for example [6]). For the purposes of this work it is assumed that t→Wb 100% of the time.

3.1.2 Theoretical Motivation

The primary motivation for studying single top is to measure the properties of the W-t-b vertex. Since each single top diagram contains a W-t-b vertex at both top production and decay an analysis of single top events has the potential to provide the best precision measurements of the properties of this vertex.

In order to perform these measurements it is first necessary to separate single top from its background. Furthermore, if it is possible to exploit kinematic or topological differences to statistically disentangle individual single top channels from each other independent measurements of W-t-b vertex properties can be obtained. One of the major goals of this work is to asses the possibility of making measurements in each of the three channels independently at ATLAS.

There are several advantages to studying the three single top channels as separate processes. Most importantly, the measured rates of the three channels are affected differently by physics beyond the Standard Model [37]. For example, the existence of a heavy vector boson (W′) will enhance the rate of the W* process due to the existence of extra s-channel diagrams proceeding through the W′. This heavy boson would have little effect on the rate of Wg-fusion since the contribution from new t-channel diagrams would be suppressed by $(1/m_{W'})^2$. Alternatively, diagrams involving flavour-changing neutral currents will usually contain only 1 b-jet in the final state and will primarily affect the observed rate of Wg-fusion (as explained in Section 3.2.6) but will not affect the rate of W*. With this information it is possible

to use single top both as a probe for physics beyond the Standard Model and as a discriminator between different models of the new physics. It has been suggested [37] that the most sensitive variable in determining the source of new physics is the ratio of the rate of Wg-fusion and W*. This ratio would allow the cancelation of several sources of theoretical and experimental error. Very little theoretical work has been done to understand sources of new physics which would be manifested in a change in the rate of the Wt process. The work that has been done so far indicates that it is relatively insensitive to physics beyond the Standard Model.

Previous theoretical studies [40, 41] have suggested that it will be possible at the LHC to obtain a sample of the highest rate single top process (Wg-fusion) with a signal-to-background ratio (S/B) of approximately 1. Unfortunately, these same studies have suggested that it is not possible to separate the s-channel process from background. If these studies are correct it is not possible to separately measure the properties of the W-t-b vertex in more than one production channel at the LHC. Until this work, no detailed experimental study had been performed to test these theoretical conclusions.

3.1.3 Single Top Measurements and Prospects at Fermilab

It should be possible to make electroweak top measurements before the completion of the LHC. The Fermilab Tevatron, where the top quark was discovered, also produces sufficient energy to create single top quarks in hadronic collisions. However, the number of events produced at Tevatron is very low and measurement possibilities will be limited by low statistics.

In the data-taking period referred to as "Run I", which took place from 1992 to 1996, the Tevatron delivered an integrated luminosity of $\sim$125 pb^{-1} per experiment at a centre of mass energy of 1.8 TeV [13]. At this energy the predicted cross-section for electroweak top production is approximately 2.4 pb [35, 36] for the combined Wg-fusion and W* signal. With this low cross-section and limited luminosity it was not possible to find evidence of an electroweak top signal in Tevatron Run I data.

However, the CDF experiment has placed 95% confidence level upper-limits on the cross-sections of both the Wg-fusion and W* processes. These limits are 15.4 pb and 15.8 pb for Wg-fusion and W*, respectively [42].

The Tevatron and the experiments which use it are currently undergoing major upgrades in preparation for taking new data at a centre of mass energy of 2.0 TeV. This energy upgrade leads to an increase in the overall single top cross-section to 3.32 pb, a nearly 40% increase in rate. In addition to the upgrade in energy the instantaneous luminosity is being increased from a peak of $2 \times 10^{31}\text{cm}^{-2}\text{s}^{-1}$ in Run I to $10^{32}\text{cm}^{-2}\text{s}^{-1}$ in "Run II" [43]. This leads to a predicted integrated luminosity of 2 fb^{-1} and a predicted significance $(S/\sqrt{B})$ of greater than 4 [42]. This implies that the production cross-section of single top will be measured to a precision of less than 30%.

Though the Tevatron experiments have the potential to confirm the existence of a single top signal in upcoming data-taking periods, they lack the statistical power to disentangle the individual single top channels. They will also be unable to measure top polarization, which requires enough statistics for a detailed analysis of angular distributions. Nevertheless, the analyses made from Tevatron Run II data should produce valuable measurements of the W-t-b vertex.

3.2 Measurement of $|\text{V}_{\text{tb}}|$

3.2.1 The CKM Matrix

$|\text{V}_{\text{tb}}|$ is an element of the Cabibbo-Kobayashi-Maskawa (CKM) matrix. This matrix describes the mixing between quark generations. It is necessary because the weak interaction does not couple quark pairs in the straightforward manner

$$\begin{pmatrix} u \\ d \end{pmatrix}, \quad \begin{pmatrix} c \\ s \end{pmatrix}, \quad \begin{pmatrix} t \\ b \end{pmatrix}. \tag{3.1}$$

Instead, it couples

$$\begin{pmatrix} u \\ d' \end{pmatrix}, \quad \begin{pmatrix} c \\ s' \end{pmatrix}, \quad \begin{pmatrix} t \\ b' \end{pmatrix} \tag{3.2}$$

where d',s' and b' are the weak eigenstates which are linear combinations of the three physical quarks (mass eigenstates). In other words, the quark mass eigenstates are not the same as their weak eigenstates. The linear combinations of physical states is given by the following relation

$$\begin{pmatrix} d' \\ s' \\ b' \end{pmatrix} = \begin{pmatrix} \mathrm{V_{ud}} & \mathrm{V_{us}} & \mathrm{V_{ub}} \\ \mathrm{V_{cd}} & \mathrm{V_{cs}} & \mathrm{V_{cb}} \\ \mathrm{V_{td}} & \mathrm{V_{ts}} & \mathrm{V_{tb}} \end{pmatrix} \begin{pmatrix} d \\ s \\ b \end{pmatrix} \tag{3.3}$$

where the matrix relating the mass states to the weak states is the CKM matrix.

The value of the CKM matrix elements are not predicted by the Standard Model and must be measured through experiment. If, however, it is assumed that there are only three generations of quarks then unitarity conditions may be invoked to constrain an element of the matrix given measurements the other two elements in the same row or column.

3.2.2 Measuring $|\mathrm{V_{tb}}|$ at Hadron Colliders

The value of the CKM matrix element $|\mathrm{V_{tb}}|$ has never been directly measured. Despite this fact it is, as a fraction of its value, the most highly constrained element of the matrix [13,44]. This value for $|\mathrm{V_{tb}}|$ relies on a unitarity constraint with three quark generations (ie. $|\mathrm{V_{td}}|^2 + |\mathrm{V_{ts}}|^2 + |\mathrm{V_{tb}}|^2 = 1$). If this assumption is invalid the value of $|\mathrm{V_{tb}}|$ is virtually unconstrained. A measurement of $|\mathrm{V_{tb}}|$ different from the predicted value would imply the existence of physics beyond the Standard Model.

There are several ways to obtain indirect information on $|\mathrm{V_{tb}}|$. The dominant mechanism for producing top quarks at the LHC is $\mathrm{t\bar{t}}$ production. Though this source of top quarks contains two W-t-b vertices in its decay it cannot be used to make a direct measurement of $|\mathrm{V_{tb}}|$. Measurements from $\mathrm{t\bar{t}}$ can provide a ratio of matrix elements:

$$\frac{BR(t \to Wb)}{BR(t \to Wq)} = \frac{|\mathrm{V_{tb}}|^2}{|\mathrm{V_{td}}|^2 + |\mathrm{V_{ts}}|^2 + |\mathrm{V_{tb}}|^2}$$

and hence can constrain $|\mathrm{V_{tb}}|$ in a 3-generation model, but cannot be used to predict $|\mathrm{V_{tb}}|$ directly. $|\mathrm{V_{tb}}|$ can also be constrained by comparing precision electroweak measurements to loop corrections containing the W-t-b vertex.

process	total cross-section (pb)	$\sigma\times$ BR (pb)
W*	10 [36]	2.22
Wg-fusion	244 [35]	54.2
Wt	60	17.8
$t\bar{t}$	830 [45]	246
$Wb\bar{b}$	300 [40]	66.7
Wjj	18000	4000

Table 3.3: This table shows the cross-sections for the processes considered in this study and the cross-section $\times$ branching ratio needed to study only electron and muon final states. The cross-section for the Wjj process is obtained by normalizing the cross-section obtained from HERWIG [46] with cuts requiring at least 2 jets above 15 GeV with $|\eta| < 3.2$ to the cross-section from VECBOS [47] for these cuts. HERWIG is then used to estimate the cross-section when the jet region is extended to $|\eta| < 5$ to obtain 18000 pb.

Electroweak top production is the only way to produce a direct measurement of $|V_{tb}|$ at a hadron collider. Each single top production diagram contains a W-t-b vertex which contributes a factor

$$\frac{-ig_w}{2\sqrt{2}}|V_{tb}|\ \gamma^\mu(1-\gamma^5)$$

to the matrix element. This means that each single top process has a cross-section which is directly proportional to $|V_{tb}|^2$. By measuring the rate of single top processes and combining this information with t$\rightarrow$Wb branching ratio and top mass measurements from the $t\bar{t}$ channel, the absolute value of $|V_{tb}|$ can be extracted.

3.2.3 Common Backgrounds to Single Top Processes

Single top production at the LHC is plagued by several high rate backgrounds including $t\bar{t}$ and Wjj production. The Wjj process refers to W's produced in association with at least 2 jets. In this analysis Wjj does not include the case in which both jets are b-jets, this case is treated separately. The cross-sections[3] for the processes of interest are shown in Table 3.3. This table illustrates the size of the backgrounds

[3]Throughout this document the mass of the top is assumed to be 175 GeV

relative to the electroweak top signal.

In order to separate $t\bar{t}$ and Wjj from single top events, topological differences in the signals must be exploited. For example, $t\bar{t}$ events are generally characterized by higher jet multiplicities and higher average transverse momentum than single top events. However, jet identification is not perfectly efficient and some of these events will fake a single top signal. The fact that this background contains real top quarks means that it is not possible to search for a top mass peak to identify single top signals. The Wjj background is essentially Drell-Yan W production with at least 2 radiated jets. The major features which distinguish this background from electroweak top production are the lack of high P_{T} b-jets and the lack of a top mass peak. However, some Wjj events will contain charm or light quark jets which will be mistagged as b's and cause a fake single top signal. Wjj events which contain real b-jets are treated as a separate background in this study.

Due to these large rate differences extracting single top signals from background is expected to be a challenge. These backgrounds are particularly difficult in the W* channel for which the other single top channels are also serious backgrounds. The rate of non-top backgrounds is almost 2000 times the rate of s-channel single top. The $t\bar{t}$ background has a rate almost 100 times larger than that of s-channel single top.

These high-rate backgrounds are shared with several other interesting physics channels and will need to be thoroughly understood at ATLAS. In particular, the $t\bar{t}$ events will be thoroughly studied as a signal as it will be the source for much of the top physics planned for ATLAS.

3.2.4 Monte Carlo Single Top Production

In this study all of the processes containing top quarks are generated using the ONETOP [48] generator. This is a parton-level[4] leading-order generator which keeps

[4]Parton-level refers to the generation of the process without hadronization or the addition of initial or final state radiation. Once hadronization and radiation has been added the simulation is referred to as particle-level.

all helicity information and hence produces the correct angular distributions of top decay products. The particles from ONETOP are then passed to PYTHIA [49] which fragments the final state particles, adds initial and final state radiation and simulates the underlying event. Finally, events are passed into the ATLAS fast-simulation program (ATLFAST) [50] in order to apply detector smearing effects, b-tagging efficiencies and jet calibration. ATLFAST will be described in more detail in the next section.

The non-top backgrounds considered in this study are generated using HERWIG [46] and are also passed through the ATLAS fast detector simulation. The $Wb\bar{b}$ background is generated using non-standard HERWIG code which is modified to use the $Wb\bar{b}$ matrix element from [51]. The Wjj process is a standard HERWIG process. Since the quark jets in the Wjj process are assumed massless, the cross-section for this process becomes infinite at low jet transverse momentum (collinear divergence). To avoid this problem the cross-section for this process is defined only when 2 jets above 15 GeV P_{T} are found within $|\eta| < 5$ using the standard ATLFAST cone-based jet finding algorithm. The cross-section has been normalized using the value from the VECBOS Monte Calo generator, which has been developed and used at Fermilab to simulate vector boson production in association with jets in hadron collisions.

ATLAS Fast Detector Simulation (ATLFAST)

The ATLAS fast detector simulation program (ATLFAST) provides a particle-level (jet-level) simulation of the smearing effects of the ATLAS detector. It is an intermediate step between parton-level generator studies and full detector simulation. It includes most crucial detector aspects: jets reconstruction in the calorimeter, momentum and energy smearing for leptons and photons, magnetic fields effects and missing transverse energy. It also provides a set of routines which simulate efficiencies for tagging and rejection of b-jets, c-jets and tau-jets. It does not simulate effects related to the detailed shapes of particle showers and energy isolation of

Parton Type	Efficiency
u-quark	83%
b-quark	76%
gluon	74%

Table 3.4: Efficiency for jet reconstruction at low luminosity for different types of initial partons with cones of R=0.4 and P_{T}>15 GeV. This table is taken from [50].

leptons is simulated only in a crude way.

The simulated energy resolution for jets in ATLFAST at low luminosity is $50\%/\sqrt{E}$ + 3% [5] for $|\eta| < 3.0$ and $100\%/\sqrt{E}$ + 7% for the forward region ($3.0 < |\eta| < 5.0$) in accordance with the ATLAS design requirements [7]. A standard cone algorithm [50] with cone size R=0.4 is used to reconstruct jets[6]. The efficiency for jet reconstruction is listed in Table 3.4 for three different types of jets. Jets are required to have at least 15 GeV P_{T} and may be found out to a pseudorapidity of $\pm$5.

The parameterization of the smearing of leptons is more complicated than that for jets. In the region $|\eta| < 1.4$ the resolution is $12\%/\sqrt{E}$ plus a P_{T}-dependent term plus a constant term. In the region $|\eta| > 1.4$ the resolution is parameterized as a continuous function of pseudorapidity and energy plus a small constant term. Leptons are identified (ie. separated from jets) using isolation criteria. Electron isolation requires P_{T}>5 GeV, separation of $R > 0.4$ from other clusters and E_{T}<10 GeV in an $R = 0.2$ cone. Electron isolation can only be established in the region $|\eta| < 2.5$ as this is the extent of the ATLAS inner tracking. These chosen criteria have an efficiency of approximately 95% for isolated electrons.

For the purposes of this study b-tagging is done without imposing a P_{T} dependence. b-jets are simply tagged as such with 60% efficiency. The charm quark mistag rate is 10% while the rate for light quark mistags is only 1%. b-jets can only be identified in the ATLAS central region ($|\eta| < 2.5$) since inner tracking is required.

[5] In all of the energy resolution parameterizations presented in this document the units of energy are GeV.

[6] R is a measure of the lateral spread of the jet in $\eta - \phi$ space: $R = \sqrt{(\Delta\eta)^2 + (\Delta\phi)^2}$

3.2.5 Kinematics of Signal and Background

In order to understand the differences between the single top signals and their major backgrounds it is necessary to compare a variety of kinematic variables. Distributions of several useful variables are presented in this section. Each distribution has been normalized to unit area in order to emphasize kinematic rather than rate differences. All of the plots displayed herein are created after detector smearing has been applied. All observables must meet the following definitions:

- isolated electrons: $|\eta| < 2.5, P_{\mathrm{T}} > 5$ GeV, separation of $R > 0.4$ from other clusters of energetic cells and $E_{\mathrm{T}}<$ 10 GeV in an R =0.2 cone, where R = $\sqrt{(\Delta\eta)^2 + (\Delta\phi)^2}$
- jet: $|\eta| < 5, P_{\mathrm{T}} > 15$ GeV;
- b-jet: jet and $|\eta| < 2.5$, 60% tagging efficiency, 10% c-mistag rate and 1% light-quark mistag rate.

Pre-selection cuts have also been applied before the distributions in this section were created. These cuts should mimic the effect of a single top trigger selection. The cuts used are:

- at least 1 b-jet above 50 GeV P_{T};
- at least 1 lepton above 20 GeV P_{T};
- at least 2 jets above 30 GeV P_{T}.

The first variable of interest is the number of jets in the event. Figure 3.5 shows the number of reconstructed jets in an event for the single top signals and each of their backgrounds. These distributions clearly illustrate that, on average, $t\bar{t}$ events produce more jets than single top events. In fact, a cut requiring the presence of exactly 2 jets in each event is a major rejector of the $t\bar{t}$ background.

The second kinematic variable considered here is the number of b-jets tagged in an event, presented in Figure 3.6. As mentioned previously, in this sample of events

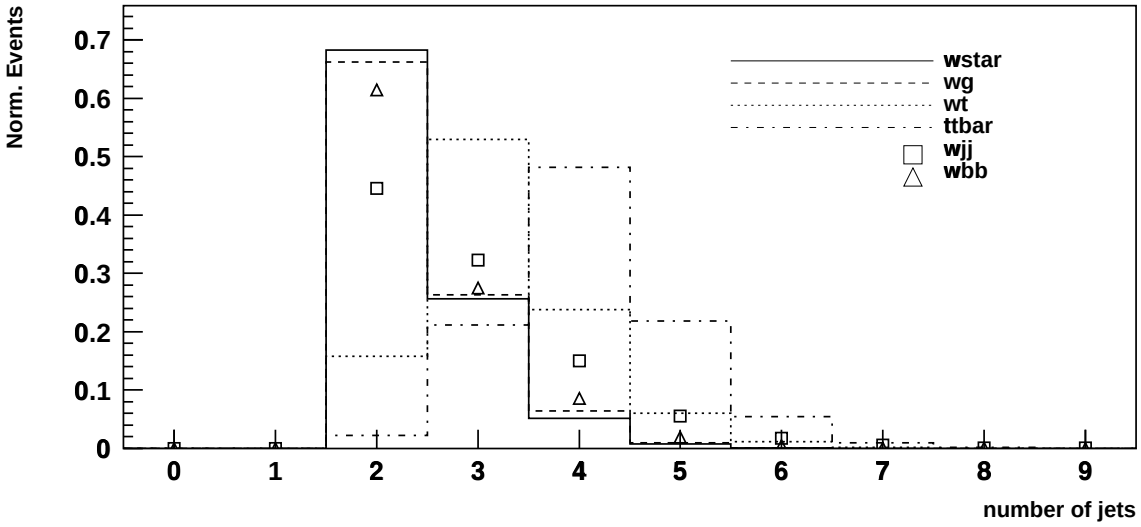

Figure 3.5: Number of jets found in signal and background after detector simulation. The area of the histogram has been normalized to 1. Refer to text for description of pre-selection cuts.

there is already a requirement that there be at least one tagged b-jet (hence the absence of events in the zero-jet bin). It can be seen from this figure that requiring more than one b-tagged jet will further enhance the W* signal with respect to Wjj and W-g fusion. Though in principle W-g fusion events contain as many b-jets as W* events, in practice one of the jets will quite often be missed (ie. not tagged) because it has low transverse momentum and will not meet the minimum b-tag requirements.

Another variable which can be used to separate signal from background is the reconstructed top mass (since there is no top quark in the Wjj background). In order to reconstruct the top mass the 4-momentum of its decay products must be measured. Since the top decays to Wb, these must be reconstructed from their decay products. The W's considered in this study decay to a charged lepton (e or μ) and a neutrino. Since the momentum of the neutrino can only be measured as missing transverse momentum the 4-vector of the W cannot be fully reconstructed. However, using the known W mass as a constraint it is possible to estimate the neutrino's z-momentum within a 2-fold ambiguity as shown in Appendix B. Then,

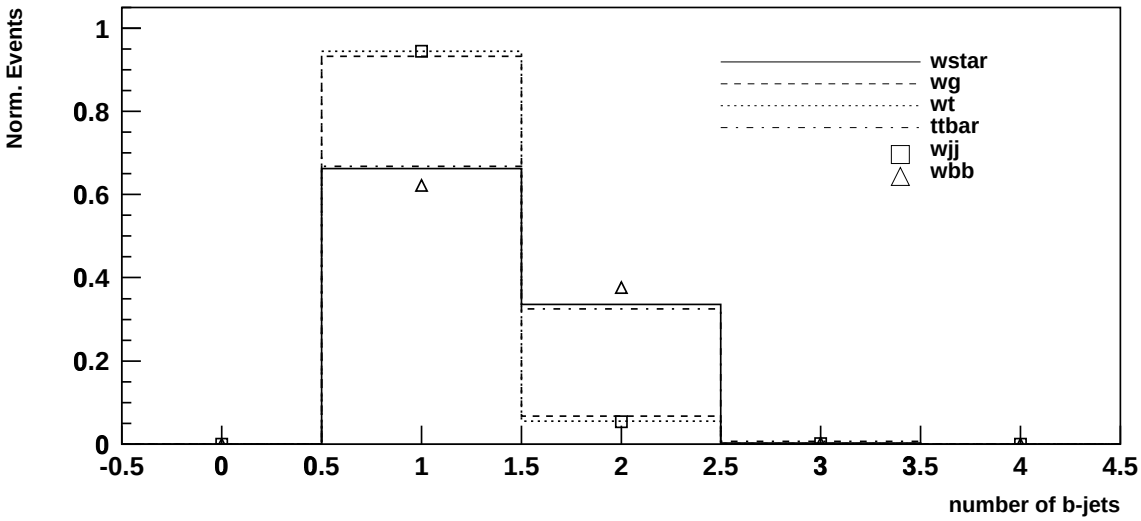

Figure 3.6: Number of b-jets found in signal and background events after detector simulation. The area of the histogram has been normalized to 1. Refer to text for description of pre-selection cuts.

the solution which gives the reconstructed top mass closest to the known mass is chosen as the correct one. If the event contains more than one b-jet this also introduces an ambiguity. Again the choice is made based on which solution gives the best top mass. This method of resolving these ambiguities leads to a shaping of the non-top backgrounds to look like the signal. Figure 3.7 shows the top mass reconstructed by choosing the b-jet and the neutrino z-momentum which give the best top mass. Though the distributions for the non-top backgrounds are peaked in the region of the top mass, it is still evident that a top mass window cut will remove relatively more background than signal.

Another kinematic variable which proves useful in distinguishing signal from background is the scalar sum of the P_{T} of all of the jets in an event. Figure 3.8 illustrates the wide range of P_{T} that exists between the different processes. Clearly the P_{T} in $\mathrm{t\bar{t}}$ is much higher on average (as expected) than in the signal while the Wjj background has quite low average P_{T}.

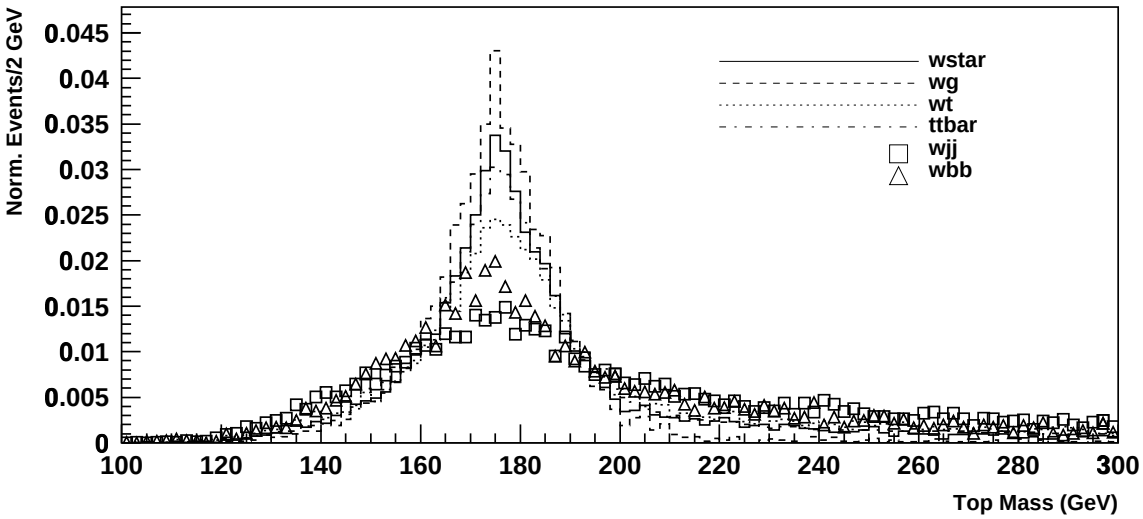

Figure 3.7: l-b-ν combination that gives the best top mass. The area of the histogram has been normalized to 1. Refer to text for description of pre-selection cuts.

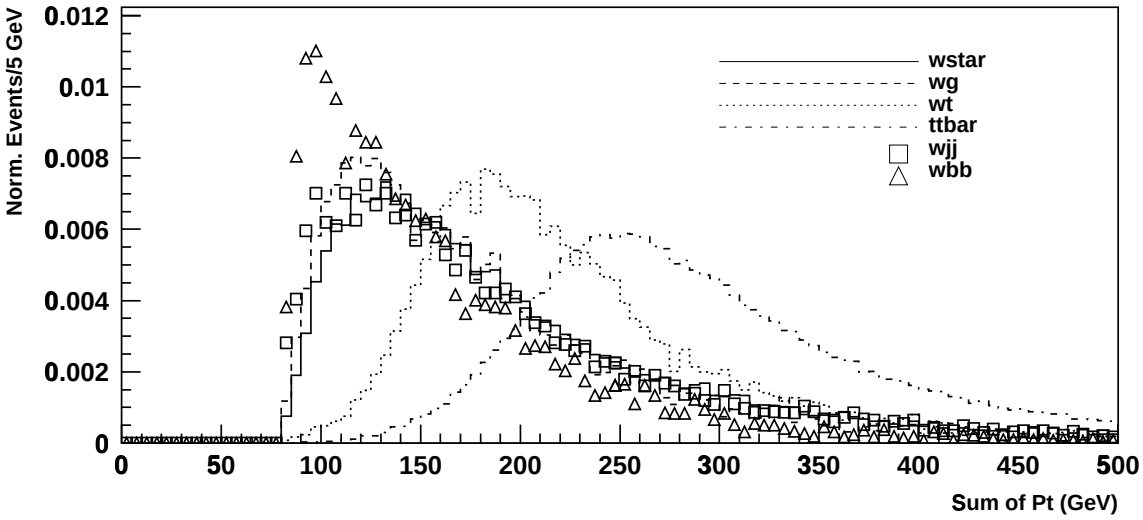

Figure 3.8: Scalar sum of jet P_{T} in each event for signal and background after detector simulation. The area of the histogram has been normalized to 1. Refer to text for description of pre-selection cuts.

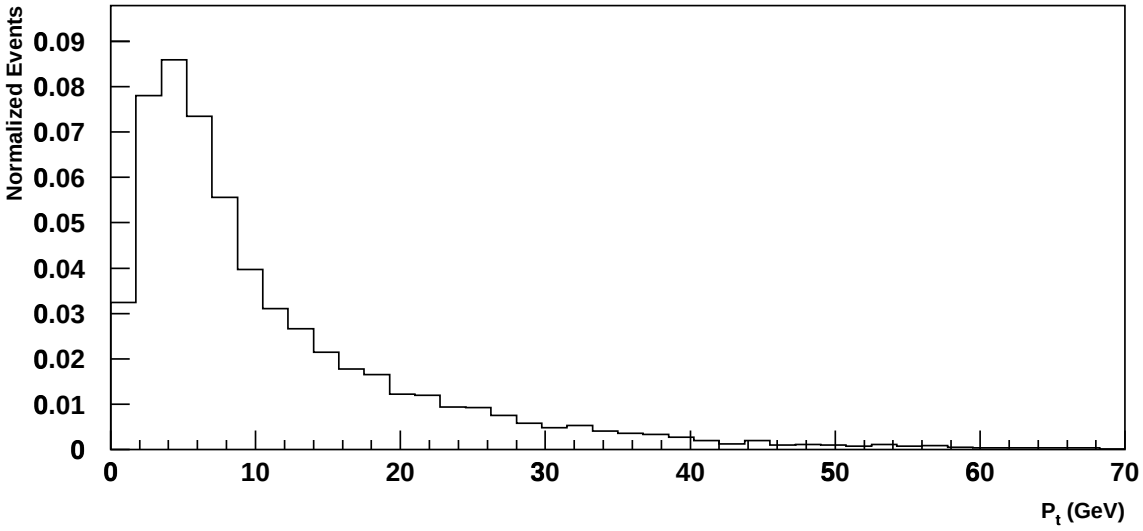

Figure 3.9: The distribution of transverse momentum of the b produced in association with the top quark in Wg-fusion events.

3.2.6 Measurement of Wg-fusion Cross-Section

The Wg-fusion channel is the largest source of single top events at the LHC with a cross-section of approximately 244 pb (more than 6000/day at $10^{33}\text{cm}^{-2}\text{s}^{-1}$). For this reason it will be the source of much of the physics extracted from single top at ATLAS.

Wg-fusion events contain kinematic features which distinguish it from its backgrounds and from other types of single top events. One of these features is the presence of a spectator quark jet which emerges in the forward direction. Requiring the presence of a forward jet with $|\eta| > 2.5$ and P_{T}>50 GeV is an important cut to reduce background. A second distinguishing feature is the low transverse momentum of the b-jet produced in association with the top quark (see Figure 3.9). This low P_{T} b-jet will often not be tagged as a b simply because it is outside the b-tagging volume ($|\eta| < 2.5$) or because it does not meet minimum jet P_{T} requirements. This means that a large fraction of Wg-fusion events will appear to contain only one b-quark jet. This is useful in distinguishing Wg-fusion events from other types of single top or from $t\bar{t}$ which each contain 2 high P_{T} b-jets.

In addition to these special distinguishing features of the Wg-fusion signal there

cut	Wg-fusion eff(%)	$t\bar{t}$ eff(%)	$Wb\bar{b}$ eff(%)	Wjj eff (%)	S/B
pre-selection	26.8	43.4	2.5	0.67	0.07
njets=2 P_T>30 GeV	12.0	0.85	1.6	0.29	0.44
fwd jet $\|\eta\| > 2.5$ P_T>50 GeV	4.1	0.035	0.064	0.044	1.2
$\sum^{jets} P_T$ >200 GeV	1.1	0.012	0.010	0.0086	1.6
$M_{l\nu b}$ 150-200 GeV	0.70	0.0045	0.00029	0.0017	4.9
events/ $3 \times 10^4 pb^{-1}$ (before cuts)	1.63×10^6	7.2×10^6	2.0×10^6	6.8×10^7	0.021
events/ $3 \times 10^4 pb^{-1}$ (after cuts)	11532 ± 71	332 ± 108	≈ 0	2000 ± 260	4.9 ± 0.8

Table 3.5: Cumulative effect of cuts on Wg-fusion signal and backgrounds. The first 6 rows of this table refer to cumulative efficiencies of various cuts. The last two rows refer to the number of events for $3 \times 10^4 pb^{-1}$. Only events in which W$\rightarrow$ eν or $\mu\nu$ are considered in this table. Errors quoted in this table are due entirely to Monte Carlo statistics.

are several simple kinematic requirements which can be employed to reduce non-single-top backgrounds. A jet multiplicity requirement of exactly 2 jets in each event is an important cut to reduce $t\bar{t}$ background. Requiring that one of these jets be tagged as a b-jet above 50 GeV P_T reduces the Wjj background. Further reduction of the "soft" Wjj backgrounds can be obtained by requiring the sum of the P_T of all jets in the event to be above 200 GeV. Finally, an allowed window 150-200 GeV on the reconstructed top mass aids in reducing contributions from non-top backgrounds (Wjj and $Wb\bar{b}$).

Table 3.5 presents the cumulative effect of all of these cuts on the Wg-fusion signal and on its significant backgrounds, Wjj, $Wb\bar{b}$ and $t\bar{t}$. From this table the

signal-to-background ratio predicted for the Wg-fusion channel is calculated to be 4.9. After three years of running at low luminosity ($10^{33}\text{cm}^{-2}\text{s}^{-1}$) this implies a signal significance ($S/\sqrt{B}$) of 239. It is also possible to calculate the expected statistical error on the Wg-fusion cross-section after an integrated luminosity of $3 \times 10^4\text{pb}^{-1}$ (3 years). The statistical precision on the cross-section, calculated from $\sqrt{S+B}/S$, is 1.02%. Since the cross-section is proportional to $|\text{V}_{\text{tb}}|^2$ this implies a statistical precision on $||\text{V}_{\text{tb}}||$ of 0.51% in this channel.

From Section 3.1.1 the theoretical error on the Wg-fusion cross-section is estimated to be 11% (combining theoretical errors in quadrature). Combining this with the statistical error on the cross-section yields a precision on $|\text{V}_{\text{tb}}|$ of 11%. Clearly, at this time the estimated theoretical error would dominate the measurement.

3.2.7 Measurement of Wt Cross-Section

The Wt channel is the second largest source of single top events at the LHC with a cross-section of approximately 60 pb (more than 1500/day at $10^{33}\text{cm}^{-2}\text{s}^{-1}$). Since this process has a negligibly small cross-section at the Tevatron (due to the two high-mass particles in the final state) it has not received much theoretical attention. The theoretical error on the cross-section prediction is estimated at 50% as it is only known to leading order.

The strategy for measuring the Wt cross-section is similar to that for Wg-fusion as they share the same backgrounds. However, the nature of Wt events makes them relatively easy to separate from Wjj and difficult to separate from $\text{t}\bar{\text{t}}$ events. Despite this difficulty in removing the $\text{t}\bar{\text{t}}$ background, this does not preclude obtaining a precise measurement of $|\text{V}_{\text{tb}}|$ in this channel assuming the rate for $\text{t}\bar{\text{t}}$ can be well measured at ATLAS.

What distinguishes the Wt signal from backgrounds other than $\text{t}\bar{\text{t}}$ is the presence of a second W in the final state. Since the presence of a single isolated high-P_{T} lepton is one of the pre-conditions of this study, the second W must decay to two jets to be accepted by the event selection. Therefore requiring a 2-jet invariant mass within

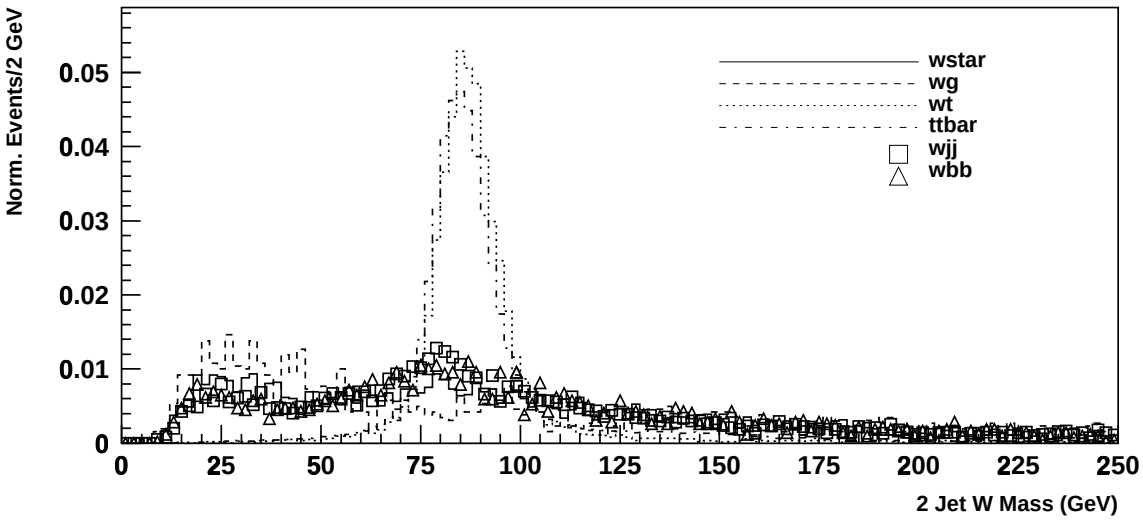

Figure 3.10: The distribution 2-jet invariant mass. For each event the 2-jet combination with mass closest to the W-mass is plotted. This clearly shows a peak in the distribution for Wt and $t\bar{t}$ which is not present for the other backgrounds.

a window around the W-mass peak will serve to eliminate most events that do not contain a second W. The 2-jet invariant mass distribution is shown in Figure 3.10 and clearly demonstrates the presence of a sharp peak in the Wt and $t\bar{t}$ signals. This effectively leaves $t\bar{t}$ as the only background to Wt events.

In addition to these special distinguishing features of the Wt signal there are several simple kinematic requirements which can be employed to reduce the $t\bar{t}$ background. By choosing events with exactly 3 jets with exactly one of them tagged as a b-jet some rejection of the $t\bar{t}$ background is possible. Some further rejection is obtained by limiting the selection to events with invariant mass less than 300 GeV, where the invariant mass of an event is defined as the invariant mass obtained by adding the 4-vectors of all reconstructed jets and leptons ($e^{\pm}$ and μ). However, even with these cuts the $t\bar{t}$ background is significantly larger than the Wt signal.

Table 3.6 presents the cumulative effect of all cuts on the Wt signal and on the $t\bar{t}$ background. The $Wb\bar{b}$ and Wg-fusion backgrounds are virtually eliminated by the cuts and so are not included in the table. From this table the predicted signal-to-background ratio for the Wt signal is calculated to be 0.24. After three years of running at low luminosity ($10^{33}\text{cm}^{-2}\text{s}^{-1}$) this implies a signal significance

cut	Wt eff(%)	$t\bar{t}$ eff(%)	Wjj eff(%)	S/B
pre-selection	25.5	44.4	0.66	0.04
njets=3 P_T>50 GeV	3.41	4.4	0.030	0.05
nbjet=1 P_T >50 GeV	3.32	3.24	0.028	0.07
Invariant Mass <300 GeV	0.55	0.36	0.00051	0.1
65<M_{jj} <95	0.49	0.14	8.5×10^{-5}	0.24
events/ $3\times10^4 pb^{-1}$ (before cuts)	534000	7.2×10^6	6.8×10^7	0.007
events/ $3\times10^4 pb^{-1}$ (after cuts)	2608 $\pm$166	10616 $\pm$625	102 59	0.24 $\pm$0.03

Table 3.6: Cumulative effect of cuts on Wt signal and backgrounds. The first 5 rows of this table refer to cumulative efficiencies of various cuts. The last two rows refer to the number of events for $3\times10^4 pb^{-1}$. Only events in which W$\rightarrow$ eν or $\mu\nu$ are considered in this table. Errors quoted in this table are due entirely to Monte Carlo statistics.

$(S/\sqrt{B})$ of 25. It is also possible to calculate the expected statistical error on the Wt cross-section after an integrated luminosity of $3 \times 10^4 \text{pb}^{-1}$ (3 years). The statistical precision on the cross-section, calculated from $\sqrt{S+B}/S$, is 4.4%. Since the cross-section is proportional to $|\text{V}_{\text{tb}}|^2$ this implies a statistical precision on $|\text{V}_{\text{tb}}|$ of 2.2% in this channel.

The theoretical error on the Wt cross-section is estimated to be 50%. Clearly, at this time the estimated theoretical error would completely dominate the measurement. It is hoped that this work will incite further theoretical study of the Wt signal in order to reduce these errors.

3.2.8 Measurement of W* Cross-Section

The s-channel single top process (W*) has a cross-section of approximately 10 pb at the LHC. Though this is a rate of a few hundred events per day at low luminosity, it was previously assumed to be negligible compared to the large Wg-fusion and $\text{t}\bar{\text{t}}$ backgrounds at the LHC [40]. If it were possible to make this measurement at ATLAS it would be a particularly interesting channel due to the low theoretical error involved in estimating its cross-section. This low theoretical error is due in part to the well-known initial state parton density functions used in the calculation and in part to the similarity of the process to Drell-Yan W production which can be well measured at ATLAS.

Measuring the cross-section of the W* signal is more difficult than other single top channels since the other channels must be considered as background. In particular, the Wg-fusion channel is a large and difficult background to separate from W*. The most important topological difference between the two signals relates to the P_{T} spectrum of the second highest P_{T} b-jet in the event. As mentioned previously, in Wg-fusion events the second b-jet tends to be "soft" (ie. low P_{T}) and is often not tagged as a b. Therefore, requiring 2 b jets above 75 GeV P_{T} will eliminate most of the Wg-fusion background to W* events.

In addition to suppressing the Wg-fusion background it is also necessary, as in

cut	W* eff(%)	Wg fusion eff(%)	Wt eff(%)	$t\bar{t}$ eff(%)	$Wb\bar{b}$ eff(%)	Wjj eff (%)	S/B
pre-selection	27.0	20.0	25.5	44.4	2.49	0.667	0.004
njets=2	18.4	13.7	4.03	0.996	1.55	0.297	0.017
nbjet=2 P_{T} >75 GeV	2.10	0.05	0.018	0.023	0.038	0.0005	0.35
$\sum^{\mathrm{jets}} P_{\mathrm{T}}$ >175 GeV	1.92	0.036	0.016	0.021	0.031	0.0004	0.38
$M_{l\nu b}$ 150-200 GeV	1.36	0.023	0.006	0.012	0.0097	0.00014	0.55
events/ $3 \times 10^4 \mathrm{pb}^{-1}$ (before cuts)	66600	1.63 $\times 10^6$	534000	7.2 $\times 10^6$	2.0 $\times 10^6$	6.8 $\times 10^7$	.0008
events/ $3 \times 10^4 \mathrm{pb}^{-1}$ (after cuts)	908 ± 35	375 ± 13	32 ± 18	885 ± 181	194 ± 34	169 ± 76	0.55 ± 0.14

Table 3.7: Cumulative effect of cuts on W* signal and backgrounds. The first 5 rows of this table refer to cumulative efficiencies of various cuts. The last two rows refer to the number of events for $3 \times 10^4 \mathrm{pb}^{-1}$. Only events in which W$\rightarrow$ eν or $\mu\nu$ are considered in this table. Errors quoted in this table are due entirely to Monte Carlo statistics.

other single top signals, to design cuts to reduce the Wjj and $t\bar{t}$ backgrounds. In order to reduce contamination by Wjj events the reconstructed top mass in each event must fall within a window about the known top mass (150-200 GeV) and the events must have a total transverse jet momentum above 175 GeV. Only events containing exactly 2 jets are kept in order to reduce $t\bar{t}$ background.

Table 3.7 presents the cumulative effect of all cuts on the W* signal and on the backgrounds. From this table the predicted signal-to-background ratio for the W* signal is calculated to be 0.55. After three years of running at low luminosity ($10^{33}\mathrm{cm}^{-2}\mathrm{s}^{-1}$) this implies a signal significance ($S/\sqrt{B}$) of 22. It is also possible to calculate the expected statistical error on the W* cross-section after an integrated

luminosity of $3 \times 10^4 \text{pb}^{-1}$ (3 years). The statistical precision on the cross-section, calculated from $\sqrt{S+B}/S$, is 5.6%. Since the cross-section is proportional to $|V_{tb}|^2$ this implies a statistical precision on $|V_{tb}|$ of 2.8% in this channel.

The theoretical error on the W* cross-section is estimated to be 7.5%. Combining this with the statistical error yields a precision of 4.7% on the measurement of $|V_{tb}|$.

This study indicates that, despite previous published predictions to the contrary, it is possible to measure $|V_{tb}|$ independently in the s-channel at the LHC. When theoretical errors are taken into account, the level of precision in this channel is comparable to that in the Wg-fusion channel.

3.2.9 Sources of Systematic Error

Though it is difficult to perform detailed systematic error estimates for these analyses in advance of the construction of ATLAS, it is worthwhile to consider sources of error which could affect these measurements.

One of the most important tools used to identify top quark events at ATLAS will be b-tagging. The tagging of high P_T b-jets is essential in order to isolate top signals from non-top backgrounds such as Wjj. The efficiency of the b-tagging algorithm and its mistag rate for light quark and charm-quark jets will determine the observed level of non-top background in the sample. As an example, the results presented in this section illustrate that after cuts the most significant remaining background to the Wg-fusion signal comes from Wjj events in which one light-quark jet has been mistagged as a b-jet. This suggests that the charm and light-quark mistag rate at ATLAS has to be well-understood as a source of systematic error in this measurement. In order to estimate the effect of the charm mistag rate on the error in $|V_{tb}|$ in the Wg-fusion channel the rate was systematically varied from 5% to 15%. This variation causes the number of Wjj background remaining after 3 years to vary from 1559 to 2475 respectively. The precision on the cross-section varies from 1.00% to 1.04%. This means that a 50% uncertainty in the charm mistag rate will lead to a systematic error of 0.01% on the measurement of $|V_{tb}|$ (1.9% relative

error).

In any cross-section measurement at a hadron collider the precision in measuring the luminosity must be considered as a source of systematic error. Typical estimates of the luminosity precision at ATLAS range from 5-10% [6], but there is hope that this can be improved below the 5% level. When a realistic estimate of this error exists it should be added in quadrature with the other sources of error.

3.3 Measurement of Single Top Polarization

Among known quarks the top is unique in that its lifetime is shorter than its hadronization time. For this reason, any polarization present in its production is transmitted to its decay products. These effects are evident in several observables including the angular distribution of the charged lepton emitted from the W decay. The top quark may therefore provide the only means to measure the polarization of a "bare" quark.

The following section provides a brief introduction to concepts and techniques relevant to the measurement of top polarization. This is followed by a detailed simulation study of the sensitivity of the ATLAS experiment to the measurement of top polarization in the Wg-fusion single top channel.

3.3.1 Theory and Techniques

Spin

The angular momentum of a particle is composed of two parts, the orbital angular momentum and the spin angular momentum. While a particle can be put in any allowed orbital momentum state each particle has an "intrinsic" spin angular momentum which cannot be changed. The spin of the top quark (and any other fermion) is 1/2. The implications of the spin-1/2 nature of the top quark are discussed in the following section.

The spin of a particle is an intrinsically quantum mechanical property. Due to the uncertainty principle it is impossible to know all three components of the

spin vector (s_x,s_y and s_z) simultaneously. Only the overall magnitude $|\vec{S}|$ and one component, conventionally chosen as s_z, can be known at the same time. If the squared magnitude of the spin vector is measured it will yield values of the form

$$\vec{S}^2 = s(s+1)\hbar \tag{3.4}$$

where

$$s = 0,\ \frac{1}{2},\ 1,\ \frac{3}{2},\ 2,\ \frac{5}{2},\ \ldots \tag{3.5}$$

Such a particle is said to have spin s. For a given value of s, a measure of s_z will yield

$$s_z = m_s\hbar \tag{3.6}$$

where

$$m_s = -s, -s+1, \ldots, s-1, s \tag{3.7}$$

All particles with half-integer spin are known as fermions. All baryons, leptons and quarks are fermions. All leptons and quarks have spin s = 1/2.

A particle which has spin s = 1/2 can exist in one of two possible states, spin up ($m_s = +1/2$) or spin down ($m_s = -1/2$). These states can be represented as two-component spinors

$$\text{up} = \begin{pmatrix} 1 \\ 0 \end{pmatrix}, \quad \text{down} = \begin{pmatrix} 0 \\ 1 \end{pmatrix} \tag{3.8}$$

The most general state of a spin-1/2 particle is a linear combination of the two allowed spin states

$$\begin{pmatrix} \alpha \\ \beta \end{pmatrix} = \alpha \begin{pmatrix} 1 \\ 0 \end{pmatrix} + \beta \begin{pmatrix} 0 \\ 1 \end{pmatrix} \tag{3.9}$$

where α and β are two complex numbers such that $|\alpha|^2 + |\beta|^2 = 1$. Until s_z is measured, a spin-1/2 particle can be viewed as existing in this combination of states. Once a measurement is made the value of s_z will be either $\hbar/2$ or $-\hbar/2$. However, a measurement need not yield either state with equal probability. The probability that it will be measured as $\hbar/2$ is given by $|\alpha|^2$ while the probability that it will be measured as $-\hbar/2$ is given by $|\beta|^2$. If a statistical ensemble of s = 1/2 particles

is measured with respect to some chosen "z" axis and these two probabilities ($|\alpha|^2$ and $|\beta|^2$) are not equal then the ensemble is said to have a "net polarization", $P = |\alpha|^2 - |\beta|^2$.

From this point onward the convention $\hbar = 1$ will be followed in all descriptions of spin-related quantities.

Helicity, Chirality and Handedness

In the literature, the definition of particles as either left- or right-handed can refer to either their chiral or helicity state. For massless or relativistic particles helicity and chirality are equivalent and there is no conflict between these two definitions. For massive particles left-handed chirality and left-handed helicity are not equivalent. In this work handedness refers to helicity states, left-handed means helicity-left and right-handed means helicity-right. Chiral states will be referred to as chiral-left and chiral-right.

Electroweak theory is described as a "chiral" theory because it contains different couplings for particles which are chiral-left than for particles which are chiral-right. In the charged weak interaction this difference arises from the presence of a $\gamma_\mu(1-\gamma^5)$ term in the vertex. This vector-axial (V-A) coupling projects out only the chiral-left states of particles, ie. the W only interacts with particles which are chiral-left.

The helicity of a particle of spin s = 1/2 is determined by the direction of the projection of its spin vector on its direction of motion. For massive particles, helicity is not a Lorentz invariant quantity and hence its value depends on the frame of reference in which it is measured. In a particular frame a particle has an helicity of -1 if its spin projection is opposite to its direction of motion and an helicity of +1 if the spin projection is along its direction of motion. If the particle is massless or highly relativistic its helicity eigenstates correspond to its chirality eigenstates and helicity is conserved. This implies, for massless particles, only left-handed particles (and right-handed anti-particles) will experience the charged weak interaction. This correspondence does not hold for massive particles.

Polarization

The polarization of an ensemble of particles is the average of the projections of the spin vector onto a given axis.

$$P \equiv -2 < \vec{S} \cdot \hat{n} > \tag{3.10}$$

It has a value between -1 and 1, where 1 represents the case in which all spin projections are anti-aligned with the chosen axis, and -1 represents the case in which all spin projections are aligned with the chosen axis. A sample of top quarks with a negative polarization will be referred to as left-polarized while a right-polarized sample refers to positive polarization.

The measured value of the polarization of a sample of particles can depend both on how the particles were produced and on the axis chosen to measure it. Top quarks produced via the strong interaction will be unpolarized (to first order) regardless of the chosen polarization axis, whereas top quarks produced via the weak interaction may be highly polarized along some axis. The actual value obtained by the measurement depends on what polarization axis is chosen. If the top quark were massless, an obvious choice for the polarization axis would be the top flight direction (the helicity basis). In this massless limit the chirality and helicity eigenstates are equivalent and a 100% chiral-left sample of top quarks is also a 100% helicity-left sample. However, since the top is massive its chirality eigenstates do not correspond to its helicity eigenstates and a measurement of polarization with respect to this axis may yield less than 100%.

Polarization of the Top Quark at the LHC

Top quarks produced via the dominant $t\bar{t}$ process are, to first order, unpolarized. Higher order diagrams will induce some polarization in the $t\bar{t}$ sample at the LHC, but the effects are predicted to be small [6]. Fortunately, top quarks produced via the charged weak interaction, such as single top production in hadron colliders, are highly polarized.

Since the top quark is massive, it is not obvious that using the top direction of motion in the rest frame of the incoming partons as the polarization axis (the helicity basis) is the optimum basis in which to perform the polarization measurement. Recent theoretical work [52] has shown that the polarization of the top is 100% when measured along the direction of the d-type quark for single top events in the W* and Wg-fusion channels. In W* events the d-type quark is present in the initial state. At the LHC it is likely not possible to determine this direction. If it were possible and a non-standard polarization is found in W* events it has been shown that measuring the polarization in both the helicity and d-quark bases can give some discrimination between theoretical models [53]. For Wg-fusion the d-type quark is the spectator quark responsible for producing a forward jet in these events. At the Tevatron this "spectator" basis has been shown to be the optimum basis in which to measure the top polarization. Work is currently underway to evaluate the viability of using this basis at the LHC [54].

As demonstrated in previous sections it should be possible to isolate samples of single top at the LHC in each production channel. In particular, the Wg-fusion channel provides a sample of top quarks which are highly polarized. This channel also provides high statistics and a good signal-to-background ratio. Due to these advantages, estimates of the ATLAS sensitivity to top polarization will focus on this channel. The other two single top channels also provide samples of highly polarized top quarks but suffer from low statistics and will not be considered in this work.

In this study the polarization of the top quark produced in Wg-fusion events will be measured in the helicity basis. If Wg-fusion is treated as a $2\rightarrow2$ process the helicity basis is equivalent to the spectator basis and the fraction of events in which the top is left-handed is approximately 97% [53][7]. However, the theoretical prediction for the polarization in the helicity basis is different depending on whether the Wg-fusion process is treated as $2\rightarrow2$ or as $2\rightarrow3$. No published theoretical calculation yet exists to predict the polarization resulting from a mixture of these treatments.

[7]The polarization is not 100% due to a small cross-section contribution from a diagram with the d-type quark in the initial state rather than the final state

The other single top signals are also expected to provide highly polarized samples of top quarks. A preliminary theoretical calculation predicts 85% left-handed tops from W* production at the LHC [54]. No such prediction yet exists for the Wt channel. These theoretical predictions for the fraction of tops which are left-handed (N_-) or right-handed (N_+) can be related to the observed polarization (P) via

$$\begin{aligned} P &= N_- - N_+ \\ &= 2N_- - 1 \end{aligned} \tag{3.11}$$

yielding a polarization of 70% for W*.

The effects of spin polarization can be observed by measuring the angular distribution of the decay products in the parent particle's rest frame. In this frame the lepton produced in top decay is preferentially emitted along the top quark spin projection for tops and against the spin projection for anti-tops (as shown in Figure 3.11). Therefore a measurement of the angle between the charged lepton and the top quark direction will produce an asymmetric distribution favouring events in which the lepton is emitted opposite to the top quark momentum. The same distribution will be obtained for anti-tops as the lepton will be emitted preferentially against the anti-top spin direction. Since the anti-top is predominantly right-handed, this is again opposite to the top quark momentum. The next section describes how these angles can be reconstructed from experimentally available information. Throughout the rest of this analysis only top quarks will be discussed, but the analysis applies equally well to anti-tops.

Top Polarization Observables

The experimental measurement of the polarization of the top quark is essentially a measurement of the angular distribution of its decay products in the top quark rest frame. In the decay $t \to l\nu b$ there are three particles requiring 2 angles each to be completely specified. However, using kinematic constraints the number of angles needed to uniquely specify the directions of these three particles can be reduced to

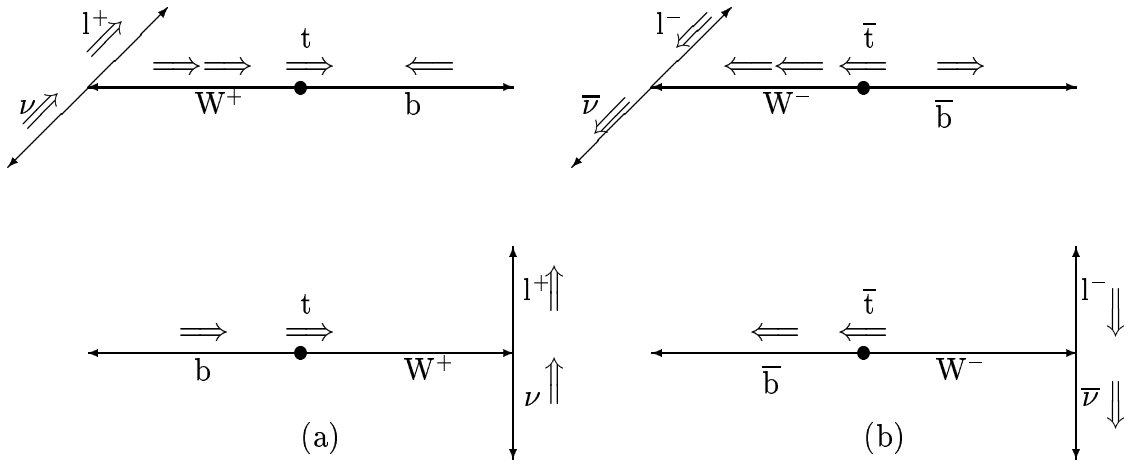

Figure 3.11: Mnemonic to illustrate that the charged lepton from top decay is preferentially emitted against the top direction of motion. The top boost is right-to-left, single lines represent particle momentum, double lines represent spin projection and all particles are drawn in the rest frame of their parent particle. (a) When top decays to a transverse polarized W the lepton is emitted preferentially along the W spin (hence along the top spin). This emission is opposite to the direction of the W boost which leads to softened lepton kinematics but does not destroy the asymmetry. The lepton from longitudinal W decay will be boosted along the W flight direction (again in the direction of the top quark spin). This boost is responsible for the observed asymmetry in the longitudinal case. (b) shows the corresponding diagrams for anti-top decay.

four [55]. It can be shown that the top polarization imposes structure on only two of these 4 angles (see Appendix C):

- θ_l : angle between the spin projection of the top along its direction of motion in the rest frame of the initial partons, and the direction of the charged lepton in the rest frame of the top quark;
- ψ_l^*: angle between the boost direction of the W in the top rest frame and the charged lepton in the W rest frame.

In terms of these angles the Standard Model prediction of the angular distribution of the top quark decay products can be written as

$$F(\cos\theta_l, \cos\psi_l^*) = K \; g(\cos\psi_l^*) \; f(\cos\theta_l) \tag{3.12}$$

where K is a combination of Standard Model parameters (masses of top, W, etc.), $g(\cos\psi_l^*)$ is the angular distribution in ψ_l^* and $f(\cos\theta_l)$ is the angular distribution in θ_l. The derivation of this functional form is presented in Appendix C. An important feature of this form is the factorization of the angular dependence. $f(\cos\theta_l)$ is sensitive solely to the spin polarization of the top quark and not to the properties of the W-t-b vertex present in the top decay. Conversely, $g(\cos\psi_l^*)$ is sensitive to the properties of the W-t-b vertex present in the top quark decay, but not to its initial polarization [8]. This allows a measurement of the effects of top polarization which is free of the influence of the W-t-b decay vertex.

The angular distribution $f(\cos\theta_l)$ is given by

$$f(\cos\theta_l) = \frac{1}{2}(1 + \cos\theta_l) \tag{3.13}$$

(see Appendix C). Since the direction of the top spin projection is not known, in this analysis the direction of the top is used. We redefine θ_l to be the angle between the

[8] The measurement of $g(\cos\psi_l^*)$ is related to the fraction of left-handed, right-handed and longitudinal W's produced in Standard Model top decay. A measurement of this angular distribution is an interesting study in its own right and will be performed from $t\bar{t}$ decays at ATLAS. Since it is not a specific feature of single top events, it is not considered in this work.

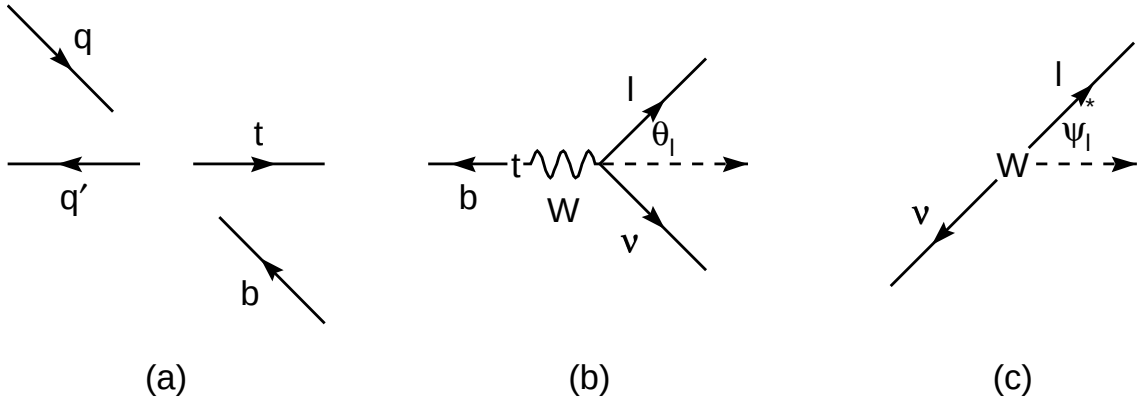

Figure 3.12: Diagram of three frames used to measure top polarization. (a) The centre-of-mass of the incoming partons (q and b). The top and q′ are produced back-to-back in this frame. (b) The rest frame of the top quark. The W and the b are back to back in this frame. The dashed line represents the top direction from the frame in (a). θ_l is the angle between the top direction in (a) and the lepton direction in (b). (c) The rest frame of the W produced by top decay. The charged lepton and neutrino are back-to-back in this frame. The dashed line represents the W direction from (b). ψ_l^* is the angle between the W direction in (b) and the lepton direction in (c).

boost direction of the top quark in the rest frame of the incoming partons and the charged lepton direction in the top rest frame. Figure 3.12 is provided to illustrate the angles and frames needed to describe this system. Using this definition of θ_l leads to an angular distribution given by [55]:

$$f(\cos\theta_l) = \frac{1}{2}(1 - P\cos\theta_l) \tag{3.14}$$

where P is the polarization of the sample. This distribution is a simple, linear function of $\cos\theta_l$ and is drawn in Figure 3.13 for the case in which $P = 1$.

Experimentally, in order to measure the angular distribution of the charged lepton it is necessary to first reconstruct the momentum of the top in the rest frame of the initial state partons. In the case of Wg-fusion events this means adding the reconstructed 4-momenta of the top and the spectator quark jet to reconstruct the initial frame. However, the reconstruction of the top quark 4-momentum suffers from an ambiguity due to the unknown z-momentum of the neutrino produced in

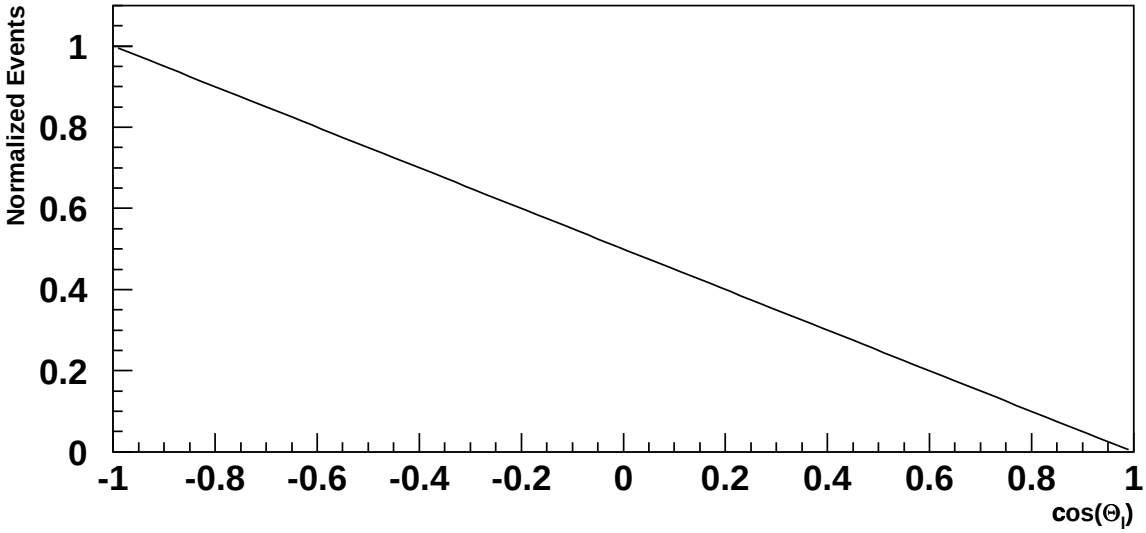

Figure 3.13: Shown is the theoretically predicted distribution of the angle between the charged lepton from top decay and the top direction for 100% polarized top quarks.

the top decay. Using the W and top masses as constraints[9] it is possible to reconstruct the top momentum, but the quality of the reconstruction is degraded by this ambiguity. Once the top 4-vector in the rest frame of the initial state partons has been obtained, it can be used in the top rest frame since it is not rotated by a boost along its 3-vector direction. This allows it to be compared to the direction of the lepton in the top rest frame to measure the angle θ_l.

Once the angle θ_l has been measured a common way to quantify the spin polarization in terms of an observable quantity is using the forward-backward asymmetry (A_{FB}):

$$A_{\mathrm{FB}} = \frac{N(\cos\theta_l < 0) - N(\cos\theta_l > 0)}{N(\cos\theta_l < 0) + N(\cos\theta_l > 0)} \tag{3.15}$$

where $N(\cos\theta_l > 0)$ is the number of events with $\cos\theta_l > 0$ and $N(\cos\theta_l < 0)$ is the number of events with $\cos\theta_l < 0$. The polarization is related to the forward-backward asymmetry simply via

$$A_{\mathrm{FB}} = \frac{1}{2}P. \tag{3.16}$$

[9]The W mass can be used to calculate the neutrino z-momentum to within a two-fold ambiguity. Of these two solutions the one which produces the best top mass is chosen. See Appendix B.

In practice, the relation between the angular distribution and the polarization is complicated by background and detector effects. The next section presents a method of extracting the top polarization in the presence of these effects.

Method for Experimental Measurement of Polarization

The goal of this analysis is to estimate how sensitive the ATLAS experiment will be to deviations from the predicted Standard Model polarization of the top quark. Since the polarization arises from the W-t-b vertex present at production, one way to test this sensitivity would be to alter the vertex from the Standard Model norm and determine if the effects of the change in the vertex can be seen in the angular distributions as measured at ATLAS. Another strategy to evaluate this sensitivity is to reweight the simulated events to effectively alter the initial polarization produced by the generator. The reweighting strategy has been chosen for this analysis.

In order to introduce an effective change of top polarization into the generated event sample it is necessary to compare the parton-level angular distribution to the theoretical distribution for the desired polarization. This comparison can be used to generate event-weights to change the generated distribution to match the theoretically predicted distribution for a different initial top polarization. For example, the first histogram in Figure 3.14 shows the theoretical angular distributions for 100% left-polarized and 100% right-polarized top quarks overlayed with the output of the Monte Carlo generator for Wg-fusion events. By dividing the bin content of the generated curve by the value of the theoretical function at the centre of the bin it is possible to create a set of weights which can be applied to the signal histogram to produce the distributions shown in the second and third histograms in Figure 3.14.

Once the weights have been calculated they can be applied event-by-event to the signal distribution after detector and event selection effects have been applied. Mixing in an appropriate level of background produces distributions corresponding to what should be seen at ATLAS for 100% left- or right-polarized top quarks. These

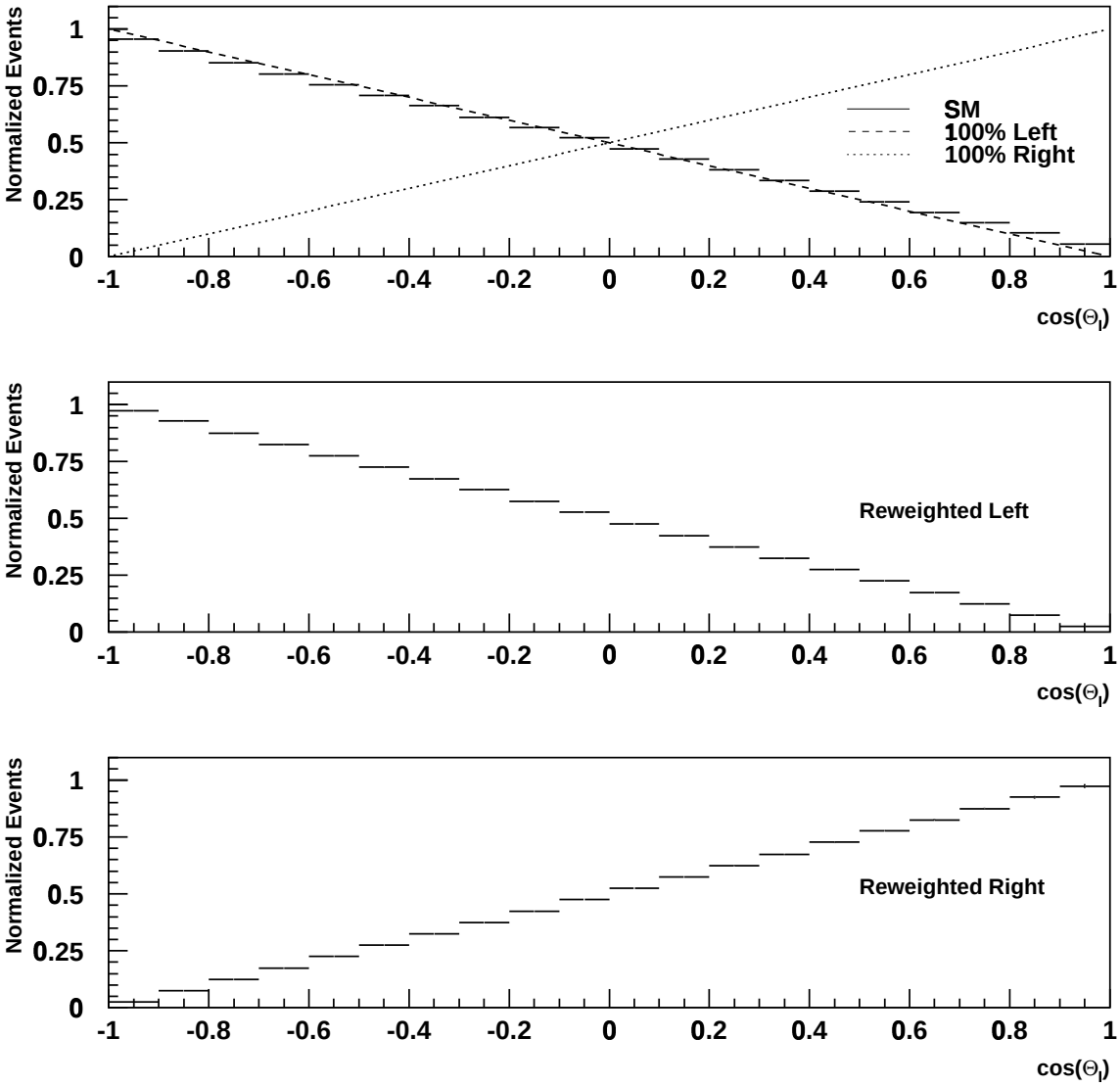

Figure 3.14: The first histogram shows the theoretical angular distribution for 100% left-polarized (dashed line) and 100% right-polarized (dotted line) top quarks overlayed with the Standard Model polarization. The second and third histograms show the distributions for 100% left and right polarization, respectively, obtained by applying weights to the generated events.

distributions can be created using a large number of events creating Monte Carlo reference distributions with small statistical error. These functions can be compared to a statistically independent sample of signal and background and the polarization of the sample can be estimated by minimizing

$$\chi^2 = \sum_{\cos\theta_i} \frac{(f_{\rm th}(\cos\theta_l)_i - f_{\rm d}(\cos\theta_l)_i)^2}{\sigma^2_{{\rm th}_i} + \sigma^2_{{\rm d}_i}} \tag{3.17}$$

where the subscript d represents quantities calculated for the data distribution and the subscript th refers to the generated reference distribution.The theoretical value $f_{\rm th}(\cos\theta_l)_i$ is calculated via

$$f_{\rm th}(\cos\theta_l) = \frac{1}{2}((1+P)f_L(\cos\theta_l) + (1-P)f_R(\cos\theta_l)) \tag{3.18}$$

where f_L and f_R refer to the value of the generated theoretical distribution for the 100% left-handed and the 100% right-handed tops respectively and P is the polarization of the top sample. The procedure returns an estimate of the top polarization and an error on that estimate. In this way the sensitivity to changes in top polarization can be quantified.

3.3.2 Measurement of Top Polarization in Wg-fusion Events

Though single top quarks produced from any of the three production channels at the LHC will be highly polarized, the most promising channel in which to perform a polarization measurement is Wg-fusion, due to the high statistics in this channel. The goal of this analysis is to estimate the sensitivity of ATLAS to the polarization of the top.

First the output of the parton-level generator is used to estimate the Standard Model polarization input to the analysis. Then the effect of detector simulation, event selection criteria and background addition on the measurement is examined. Finally, the sensitivity of the ATLAS experiment to deviations from the expected polarization of top quarks in Wg-fusion events is evaluated.

Parton-Level Polarization

The single top signals used in this study have all been produced using the ONETOP [48] parton-level Monte Carlo as described in Section 3.2.4. First we examine the angular distribution produced before hadronization or detector effects have been added. This provides the value of the top polarization as predicted by the Standard Model.

The first histogram in Figure 3.15 shows the angular distribution of the charged lepton from the top quark decay as reconstructed from parton-level information. Fitting this distribution to the functional form given in Equation 3.14 yields a value for the polarization of $94.6\pm0.1\%$. Therefore, using Equation 3.11 the fraction of events which are left-handed in this sample is $97.3\pm0.1\%$. The analysis which follows attempts to extract this number in a realistic ATLAS environment.

Effect of Detector and Data Selection on Signal

Moving from the parton-level simulation to a simulation which includes both hadronization and detector effects is certain to complicate the measurement of the polarization of the top quark. In addition, the signal could be biased by an event selection designed to eliminate background and will be contaminated by residual background events. This section examines the effect of detector simulation and event selection criteria on signal alone (ie. no background is present).

The second histogram in Figure 3.15 shows the angular distribution of the charged lepton after detector effects have been simulated. In addition to effects associated with detector energy smearing, jet and cluster definitions, etc. this distribution includes the effects of ambiguities in reconstructing the top quark due to the absence of information about the neutrino z-momentum. It does not, however, contain the effects of any event selection in order to separate signal from background. This histogram demonstrates that the effect of hadronization and detector resolution changes the shape of the angular distribution but still produces a highly asymmetric distribution.

In addition to the effects introduced by the detector resolution, the effect of applying the event selection criteria can be evaluated by applying them one at a time and observing the change in shape of this distribution. For the purposes of the polarization analysis the event selection criteria developed in the Wg-fusion cross-section measurement (Section 3.2.6) are relaxed slightly in order to increase the signal efficiency. This leads to a worse signal-to-background ratio and would lead to a less precise measure of $|V_{tb}|$ than obtained in Section 3.2.6, but is beneficial for increasing signal statistics in the polarization measurement. The criteria used in this analysis are:

- Pre-selection (trigger) cuts as in previous sections;
- number of jets = 2;
- forward jet ($|\eta| > 2.5$) with P_T>50 GeV;
- 150 GeV $< M_t <$ 200 GeV.

This set of criteria leads to a signal efficiency of 3.0%, corresponding to 48795 events after an integrated luminosity of $3 \times 10^4 \text{pb}^{-1}$. Figure 3.15 demonstrates the effect of applying these cuts in a cumulative manner. Again the asymmetry of the Wg-fusion angular distribution is preserved, though more degradation is clearly evident, in particular near $\cos\theta_l = -1$. The degradation is worse at these values of $\cos\theta_l$ because the leptons from these events are emitted in the direction opposite to the top boost. This reduces the momentum of the leptons causing more of them to fail P_T-based selection criteria.

Effect of Detector and Cuts on Background

As shown in Section 3.2.6, after cuts have been applied the most significant background to the Wg-fusion signal is Wjj. In fact, it is nearly a factor of 10 larger than the next largest background ($t\bar{t}$). For this reason, the Wjj background will be treated as the only background of importance in this analysis.

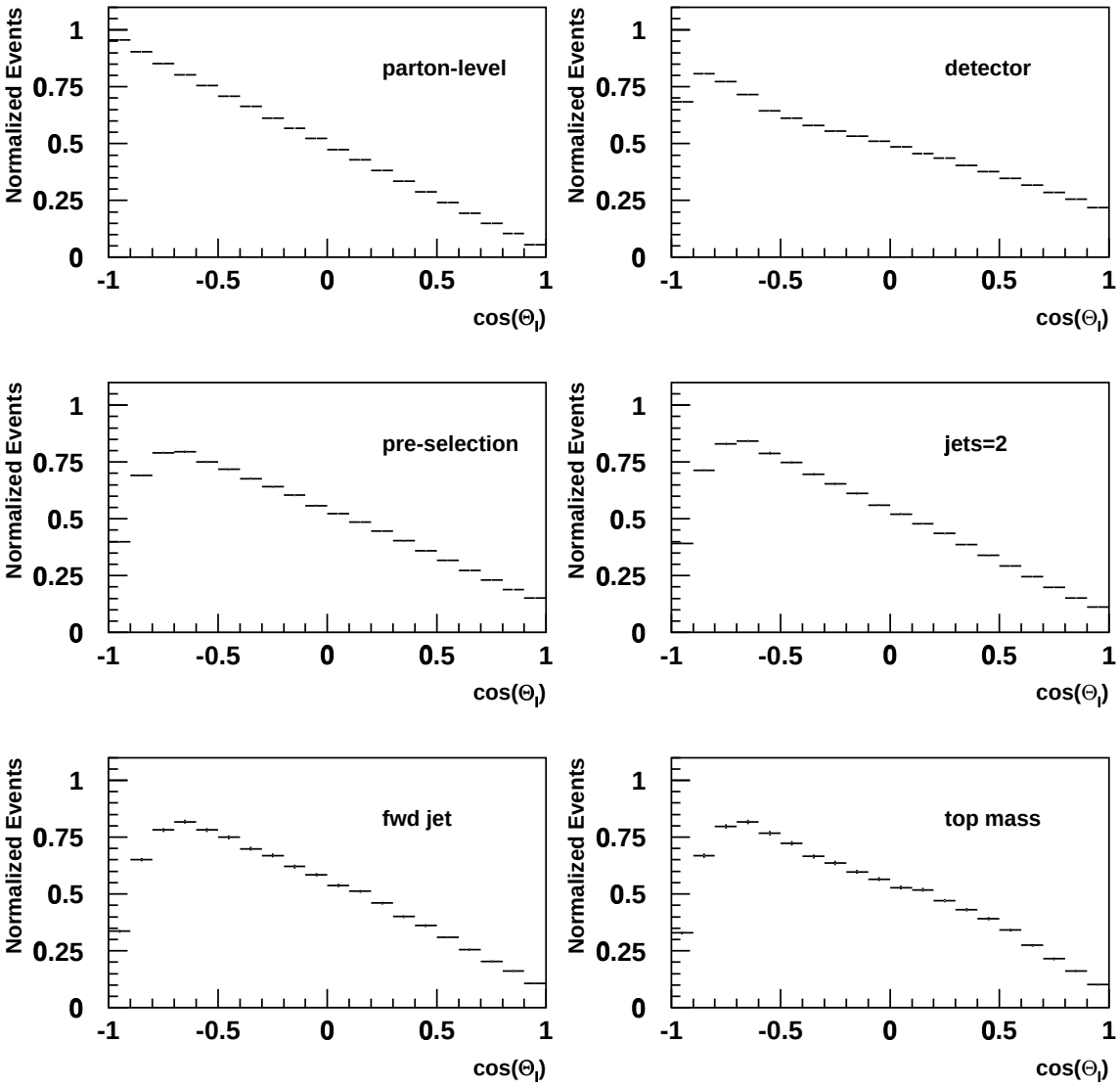

Figure 3.15: Angular distribution of charged-lepton in top rest frame for various data samples. The histograms progress from left-to-right, top-to-bottom. The first histogram shows the parton-level distribution. The second histogram is after the simulation of detector and reconstruction effects. The final 4 histograms illustrate the influence of event selection criteria on the angular distribution. The effects of the cuts are cumulative and are the result of adding pre-selection cuts, a jet multiplicity requirement, a forward jet tag and a top mass window respectively.

The Wjj background cannot easily be studied at parton level since the jets produced in association with the W are created by initial and final state radiation which is added at the particle-level of the simulation. In fact, the cross-section which must be used to normalize this process is only defined after a jet-finding algorithm with minimum P_{T} requirements have been applied to the data sample. For this reason, detector effects and the pre-selection requirements have been applied to all angular distributions from Wjj events.

Figure 3.16 shows the cumulative effect of cuts on the angular distribution of the charged lepton from Wjj events. A peculiar feature of these events is evident in all of these distributions. This is the tendency for events to be grouped near $\cos\theta_l = -1$. The events which populate this region tend to be the highest $\sum^{\mathrm{jets}} P_{\mathrm{T}}$ events. This shows that even basic jet and isolated lepton definitions and pre-selection cuts bias the angular distribution of Wjj events.

ATLAS Sensitivity Including Background and Data Selection

When the event selection criteria described in the previous sections are applied, the signal-to-background ratio (treating Wjj as the only background) is found to be 2.6. This is ratio is worse than the one obtained in the $|\mathrm{V_{tb}}|$ analysis, but the signal efficiency of the analysis is higher.

Using the methods described in Section 3.3.1 it is possible to estimate the polarization of a mixed sample of Wg-fusion signal and Wjj background. The reference distributions for 100% left and right-polarized top quarks mixed with background in a ratio of 2.6:1 are shown in Figure 3.17. Also shown is the angular distribution corresponding to a statistically independent data sample with Standard Model polarization mixed with background in the ratio 2.6:1. The chi-squared function presented in Equation 3.17 is minimized to obtain an estimate of the polarization of the top. When this fit is performed for a generated Standard Model data sample of 36340 signal events and 1345 background events renormalized to the proper S/B ratio the polarization obtained is $P = 95.8\% \pm 3.0\%$, which is compatible with the

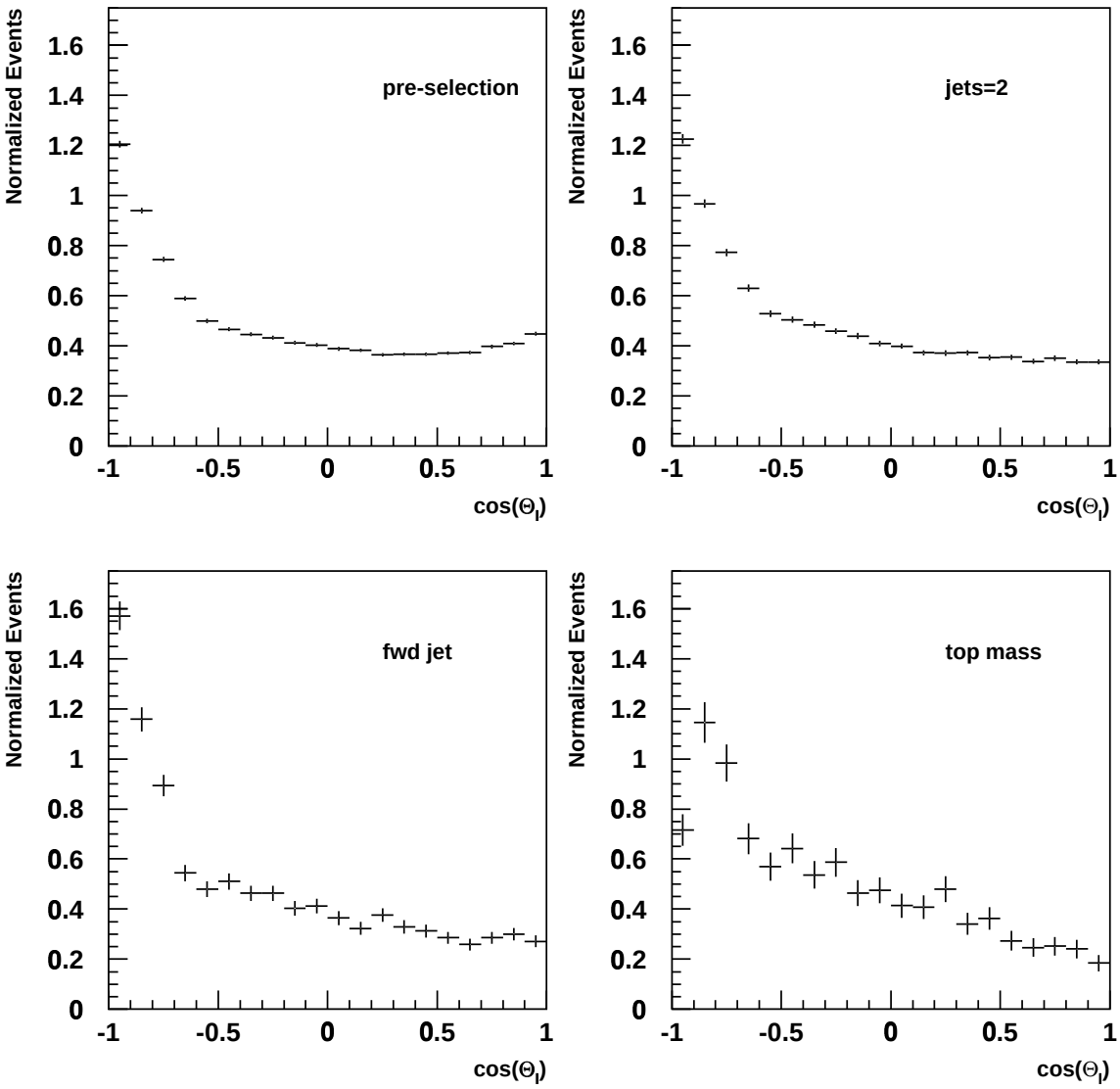

Figure 3.16: The effect of event selection cuts on the angular distribution of the charged lepton in Wjj events. The effects of the cuts are cumulative. The first distribution is the result of applying the pre-selection (trigger) cuts only and cuts are applied cumulatively from left-to-right, top-to-bottom.

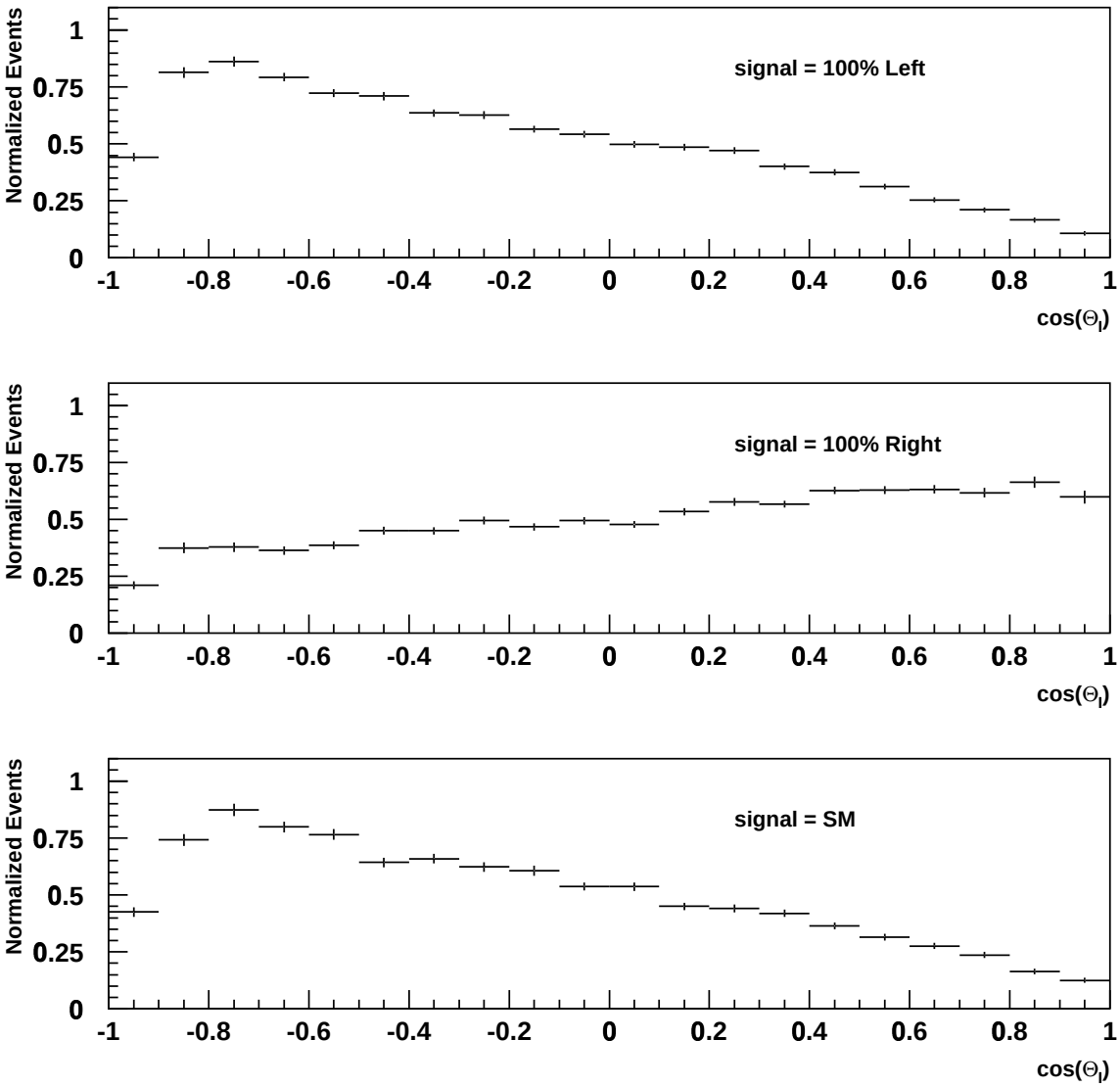

Figure 3.17: The first histogram shows the reference distribution for 100% left-handed top quarks after detector effects and event selection criteria have been applied and the appropriate level of background has been mixed in. The second histogram shows the reference distribution for 100% right-handed top quarks. The third histogram represents the expected Standard Model distribution for a statistically independent sample of signal and background.

amount of background	polarization precision(%)
none	1.0
expected	3.0
double expected	5.7
5 times expected	14.9

Table 3.8: Effect of level of background contamination on polarization measurement. The errors quoted here use the maximum available Monte Carlo statistics and do not correspond to a particular integrated luminosity at ATLAS.

parton-level Standard Model estimate of 94.6±0.1% shown earlier.

To estimate the precision for one year of data-taking at ATLAS, the fit was first redone with 3456 signal events and 1345 background events corresponding to 0.2×10^4 pb^{-1} of integrated luminosity at ATLAS ($\sim 1/5$ of a year). For this integrated luminosity the error on the polarization measurement is 4.0%. Then, assuming the statistics on the reference distributions, $f_L(\cos\theta_l)$ and $f_R(\cos\theta_l)$, will lead to a negligible source of error at ATLAS, this precision improves to 3.5%. Projecting these results to one year of data-taking at low luminosity (1×10^4pb^{-1}), assuming the errors scale as the square root of the number of events, yields a predicted precision of 1.6% on the measurement of the top polarization after one year of data-taking at ATLAS.

The dominant source of systematic error in this measurement comes from the modeling of the Wjj background. Since the rate of this background at the LHC is not well known, the sensitivity of the polarization to a change in the overall background rate has been evaluated. The same analysis described above has been performed in the absence of background, in the presence of the expected level of background, and in the presence of double and 5 times the expected level of background. The results are presented in Table 3.8 where the quoted errors are obtained using the maximum available Monte Carlo statistics and do not correspond to a particular integrated luminosity at ATLAS. These results indicate that doubling the expected background rate effectively doubles the error on the top polarization measurements.

signal	S/B	$S/\sqrt{B}$	$\Delta\|V_{tb}\|/\|V_{tb}\|$
Wg-fusion	4.9	239	0.51%
Wt	0.2	25	2.2%
W*	0.6	22	2.8%

Table 3.9: Summary of electroweak top $|V_{tb}|$ measurement results from the three channels.

3.4 Conclusions

It has been shown that it should be possible to use single top production to make valuable tests of the W-t-b vertex at ATLAS. These results indicate that it is possible to measure both top polarization and $|V_{tb}|$ during the low luminosity running period in the first three years of the LHC.

The three different sources of electroweak top production may be statistically disentangled to provide independent measurements of the CKM matrix element $|V_{tb}|$. The signal-to-background ratio and estimated statistical precision on $|V_{tb}|$ in each of these three channels is summarized in Table 3.9. Previous studies [40, 41] have concluded that the Wg-fusion signal should be visible at the LHC with a signal-to-background ratio of approximately 1. They assumed that it was not worthwhile attempting to measure $|V_{tb}|$ in either of the other single top channels as they would be swamped by $t\bar{t}$ and Wg-fusion backgrounds. The results of this study are clearly more optimistic. The main reason for the improved results for Wg-fusion is a more aggressive event selection strategy, in particular with regard to the P_T spectrum of the forward jet. Analysis in the other channels had not been attempted previously. Though the event selection could not suppress backgrounds to these processes to the extent that is possible in the Wg-fusion channel, this does not preclude precise measurement of $|V_{tb}|$ in these channels. For all three channels the error on $|V_{tb}|$ should be dominated by theoretical and systematic errors. The dominant systematic error is expected to arise from the precision on the measured luminosity.

All three sources of electroweak top production provide samples of highly polarized top quarks. Of these, the Wg-fusion production mode holds the most promise

for a precise measure of top polarization due to its high rate and high signal-to-background ratio. It has been shown in this work that the polarization of the top quark in the Wg-fusion process should be measurable to a precision of 1.6% after 1 year of running at low luminosity ($1 \times 10^4 \text{pb}^{-1}$). This precision depends on the absolute rate of the Wjj background. A doubling of the background rate leads to an approximate doubling of the error on the top polarization measurement.

In discussions of the top-physics potential of ATLAS, the electroweak top production channels have traditionally been neglected in favour of studies which can be performed with high statistical precision using $t\bar{t}$ events. This work illustrates that electroweak top production is a rich source of physics at ATLAS.

Chapter 4

Conclusions

Performance of the ATLAS detector has been evaluated in two independent studies. The first is an examination of the data from beam tests of Hadronic Endcap Calorimeter modules built to the final ATLAS design specifications. The second is a simulation study to determine the sensitivity of the ATLAS experiment to several different aspects of electroweak top measurement.

The performance of two modules representing 1/16 of one hadronic endcap has been measured with respect to electron and pion energy resolution and response and the intrinsic e/h ratio of the calorimeter. The energy resolution for electrons can be parameterized as $\sigma/E = 21.5 \pm 0.4\%/\sqrt{E_0} \oplus 0.0 \pm 0.4\% \oplus 1.33 \pm 0.04/E$ while for pions it is $\sigma/E = 78 \pm 2\%/\sqrt{E_o} \oplus 5.0 \pm 0.3\%$. Both of these values meet the expectations for this detector. Using measured values of the electron-to-pion response ratio (e/π) the intrinsic e/h of the HEC is determined to be 1.6±0.1. This is the first measurement of this quantity for the HEC. The dominant source of error in the measurement is due to lateral leakage of pion showers.

It has been shown, contrary to general expectation, that three different sources of electroweak top events can be statistically disentangled at ATLAS to provide three independent probes of the W-t-b vertex. Since the rate of each single top production channel is proportional to $|V_{tb}|^2$, the expected relative error on $|V_{tb}|$ is related to the error in measuring the cross-sections of each single top process. The three measurements yield 0.52%, 2.2% and 2.8% relative statistical error on $|V_{tb}|$

in the three channels. Currently the measurements would be completely dominated by theoretical errors in calculating the cross-sections. Sources of systematic error include the precision of the ATLAS luminosity measurement and the error in the knowledge of the b-tagging efficiency and charm-quark mistag rate.

In addition to measuring the rate of single top events it is possible to use these events to measure the polarization of the top quarks produced in the interaction. It was determined that after $1 \times 10^4 \text{pb}^{-1}$ the statistical precision on the measurement of a sample of top quarks with Standard Model polarization (94%) will be 1.6%. An error in the overall normalization of the background will affect the precision of the polarization measurement.

Bibliography

[1] Glashow, S.L., "Partial Symmetries of Weak Interactions",*Nuclear Physics* 22:579 1961.

[2] Weinberg, S., "A Model of Leptons", *Physical Review Letters* 19:1264-1266, 1967.

[3] Salam, A., *Elementary Particle Theory*, N. Svartholm, ed. (Stockholm: Almquist and Wiksell, 1968).

[4] Gelmini, G., Beyond the Standard Model, *Proceedings of the Eighth Lake Louise Winter Institute*, Lake Louise, Alberta, Canada, February, 1993.

[5] The LEP Working Group for Higgs Boson Searches, "Limits on Higgs Boson Masses from Combining the Data of the 4 LEP Experiments at $\sqrt{s} =$ 183 GeV",CERN-EP/99-060, April 1999.

[6] *ATLAS Detector and Physics Performance Technical Design Report*, Volumes I and II CERN/LHCC/99-14 and CERN/LHCC/99-15, May 1999.

[7] ATLAS Technical Design Report, CERN/LHCC/94-43, December 15, 1994.

[8] ATLAS Inner Detector Technical Design Report, CERN/LHCC/97-16, April, 1997.

[9] ATLAS Muon Spectrometer Technical Design Report, CERN/LHCC/97-22, May, 1997.

[10] ATLAS Liquid Argon Calorimeter Technical Design Report, CERN/LHCC/96-41, December 1996.

[11] ATLAS Tile Calorimeter Technical Design Report, CERN/LHCC/96-42, December 1996.

[12] Aubert, B. et al. (RD3 Collaboration), "Performance of a Liquid Argon Electromagnetic Calorimeter with and Accordion Geometry", *Nuclear Instruments and Methods in Physics Research* A309:438, 1991.

[13] Particle Data Group, "Review of Particle Physics". *European Physical Journal* C3:1-794, 1998.

[14] Huston, J., "Particle Detectors". This is an Appendix of *The Fundamental Particles and their Interactions* by Rolnick, W.B., Addison-Wesley, 1994.

[15] Amaldi, U., "Fluctuations in Calorimetry Measurements", *Physica Scripta*, 23:409-424, 1981.

[16] *Introduction to Experimental Particle Physics*, Fernow, Richard, C., Cambridge University Press, 1986.

[17] Wigmans, R., "On the Energy Resolution of Uranium and Other Hadron Calorimeters", *Nuclear Instruments and Methods in Physics Research* A259:389-429, 1987.

[18] Gabriel, T. et al., "Energy Dependence of Hadronic Activity". *Nuclear Instruments and Methods in Physics Research* A338:336-347, 1994.

[19] Loch, P., "A Brief Introduction into Principles of and Data Analysis for Sampling Calorimeters in High Energy Physics Experiments". Unpublished.

[20] Juste, A., "Analysis of the Hadronic Performance of the TILECAL Prototype Calorimeter and Comparison with Monte Carlo",*ATLAS internal note, TILECAL-95-069.*

[21] Andrieu, B. et al., "The H1 Liquid Argon Calorimeter System", *Nuclear Instruments and Method in Physics Research* A336:460, 1993.

[22] ATLAS Calorimetry Performance Technical Design Report, CERN/LHCC/96-40, December 1996.

[23] Colas, J., Pripstein, M. and Wenzel, W.A., "The Electrostatic Transformer". *Nuclear Instruments and Methods in Physics Research* A294:583-590, 1990.

[24] ATLAS HEC Collaboration, "Electron and Pion Test Beam data Analysis of the Hadronic Endcap Prototype Calorimeter". *ATLAS Internal Note ATL-LARG-98-095*, April 14, 1998.

[25] Dobbs, M., Lefebvre, M., O'Neil, D., "Hadronic Endcap Modules Zero Pion and Electron Energy Scan Analysis from April 1998 Testbeam Data". *ATLAS Internal Note: ATL-LARG-99-001*, November 23, 1998.

[26] Lefebvre, M. and O'Neil, D., "Endcap Hadronic Calorimeter Offline Testbeam Software: The hec_adc Package Version 3.6". *ATLAS Internal Note: ATL-LARG-99-002*, January 22, 1999.

[27] Cleland, W.E. and Stern, E.G., "Signal processing considerations for liquid ionization calorimeters in a high rate environment",*Nuclear Instruments and Methods in Physics Research*, A 338(1994) 467-497.

[28] Kurchaninov, L., Levitsky, M., "Optimal Weighting of signal Samples for LAr Calorimeters", *ATLAS Liquid Argon Note No. 44*, July 14, 1996.

[29] See results presented at CERN HEC testbeam meetings by A. Kiryunin.

[30] R. Brun et al., GEANT3, CERNDD/EE/84-1 (1986).

[31] *Proceedings of the Seventh International Conference on Calorimetry in High Energy Physics*, editors: Cheu, E. et al., "Energy Flow in a Hadronic Cascade: Application to Hadron Calorimetry" by Groom, D.E., pages 507-521.

[32] Graugés, Eugeni, "A Fast Simulation of Hadronic Showers in Sampling Calorimeters". *ATLAS Internal Note: ATL-TILECAL-98-158*, May 15, 1998.

[33] Abe, F. et al., The CDF Collaboration, "Observation of Top Quark Production in p-bar p Collisions with the Collider Detector at Fermilab", *Physical Review Letters* 74:2626, 1995. Abachi, S. et al., The D0 Collaboration, "Observation of the Top Quark", Physical Review Letters 74:2632, 1995.

[34] Parke, S., "Top Quark Physics: Overview", Presented at the International Symposium on QCD Corrections and New Physics held in Hiroshima, Japan, on October 27-29, 1997, hep-ph/9712512.

[35] Stelzer, T., Sullivan, Z., Willenbrock, S., "Single-Top-Quark Production via W-Gluon Fusion at Next-to-Leading Order". *Physical Review* D56:5919-5927, 1997.

[36] Smith, M. and Willenbrock, S., "QCD and Yukawa corrections to single top production via $q\overline{q} \to t\overline{b}$". *Physical Review D*, Volume 54, page 6696, 1996.

[37] Tait, T. and Yuan, C.P., "The Phenomenology of Single Top Quark Production at the Fermilab Tevatron", hep-ph/9710372, October 1997.

[38] Tait, T., private communication and Huston, J. et al. "Study of the Uncertainty of the Gluon Distribution", hep-ph/9801444, January 29, 1998.

[39] Willenbrock, S., "Overview of Single Top Theory - Measuring the Cross-section, Theoretical Uncertainties, $|V_{tb}|$, etc.", Talk presented at the "Thinkshop, Top-Quark Physics for Run II" at Fermi National Laboratory, Batavia, Illinois, October 16-18th, 1998.

[40] Seltzer, T., Sullivan, Z. and Willenbrock, S., "Single-top-quark Production at Hadron Colliders". hep-ph/9807340, July 1998.

[41] Belyaev, A.S., Boos, E.E. and Dudko, L.V., "Single Top Quark at Future Hadron Colliders. Complete Signal and Background Study". hep-ph/9806332

[42] Savard, P. for the CDF Collaboration, "Single Top and Top Quark Properties with CDF", The CDF Collaboration, FERMILAB-CONF-99/174-E. Published Proceedings 34th Rencontres de Moriond: QCD and Hadronic Interactions, Les Arcs, France, March 20-27, 1999.

[43] Amidei, D. and Brock, R., "Future ElectroWeak Physics at the Fermilab Tevatron: Report of the tev_2000 Study Group", FERMILAB-PUB-96/082, April, 1996.

[44] Willenbrock, S., "Top Quark Physics for Beautiful and Charming Physicists". hep-ph/9709355, 15 September 1997.

[45] Bonciani, R., Catani, S., Mangano, M. and Nason, P., "NLL Resumation of the Heavy-Quark Hadroproduction Cross-Section". *Nuclear Physics* B529:424-450, 1998.

[46] G. Marchesini, B.R. Webber, G. Abbiendi, I.G. Knowles, M.H. Seymour and L. Stanco, *Computer Physics Communications* 67:465, 1992.

[47] Berends,F.A., Kuijf, H., Tausk, B. and Giele,W.T., "On the Production of a W and Jets at Hadron Colliders",*Nucl.Phys.B357:32-64,1991.*

[48] D.O. Carlson, Michigan State U. Ph.D. Thesis, UMI-96-05840-mc (microfiche), 1995. 126pp.

[49] Sjostrand, T., "High-Energy Physics Event Generation with PYTHIA 5.7 and JETSET 7.4", *Computer Physics Communications* 82:74, 1994.

[50] Richter-Was, E., Froidevaux, D., Poggioli, L., "ATLFAST 2.0 a fast simulation package for ATLAS", ATLAS Internal Note: ATL-PHYS-98-131.

[51] Mangano, M., "Production of W Plus Heavy Quark Pairs in Hadronic Collisions",*Nuclear Physics*, b405:536-554, 1993.

[52] Mahlon, G. and Parke, S., "Improved Spin Basis for Angular Correlation Studies in Single Top Production at the Fermilab Tevatron", *Physical Review* D55:7249-7254, 1997.

[53] Tait, T., "Signals of the Electroweak Symmetry Breaking Associated with the Top Quark", Ph.D. Dissertation, Michigan State University, 1999.

[54] Gregory Mahlon and Stephen Parke, private communication.

[55] Guillian, G, Campbell, M. and Amidei, D., "The Choice of Measurements for Studying the Top Quark Decay Product Angular Distribution",CDFNOTE 4262, October 1, 1997.

[56] Guillian, G., "Top Quark Decay Kinematics in Fully Reconstructed $t\bar{t}$ in the e or μ + missing $E_{\mathrm{T}} + \geq 4$ jet decay channel", Ph.D. Dissertation, University of Michigan, 1999.

Appendix A

Beam Test Data Runs

This appendix contains the list of run numbers corresponding to the pion and electron data used in the study of the performance of the ATLAS hadronic endcap calorimeter. The numbers are only meaningful to HEC experts who wish to reproduce the results presented in this work.

Electron Data				
Energy (GeV)	point D Run #	point E Run #	point H Run #	point I Run #
20	7353	7350	7352	7351
40	7298	7291	7295	7294
60	7255	7259	7253	7260
80	7299	7311	7303	
100	7334	7341	7330	7342
119.1	7065	7088	7071	7079
Pion Data				
Energy (GeV)	point D Run #	point E Run #	point H Run #	point I Run #
20	7354	7371	7369	
40	7297	7292	7296	7293
60	7281	7287	7280	7285
80	7300	7312	7304	7310
100	7335	7340	7331	7343
120	7196	7154	7182	7146
180	7355	7359	7356	7360

Appendix B

Obtaining the Longitudinal Neutrino Momentum Using a W-mass Constraint

The reconstruction of the top quark from its leptonic decay channel (t$\rightarrow l\nu b$) is complicated by the inability to measure the neutrino momentum. While the transverse momentum of the neutrino can be estimated from missing transverse energy, the longitudinal momentum is unknown. This appendix shows how it is possible to obtain the longitudinal momentum component to within a 2-fold ambiguity using the W mass as a constraint.

The 4-momentum of the W is related to its mass via:

$$P_w^2 = (P_l + P_\nu)^2 = M_w^2. \tag{B.1}$$

Assuming the charged lepton and neutrino are massless, such that $P_l^2 = P_\nu^2 = 0$ gives

$$M_w^2 = 2P_l \cdot P_\nu = 2E_l E_\nu - 2\vec{P_l} \cdot \vec{P_\nu}. \tag{B.2}$$

Expressing 3-momenta as a sum of longitudinal and transverse components (eg. $\vec{P_l} = \vec{P_{Tl}} + \vec{P_{Ll}}$) gives

$$M_w^2 = 2E_l E_\nu - 2(\vec{P_{Tl}} \cdot \vec{P_{T\nu}}) - 2(\vec{P_{Ll}} \cdot \vec{P_{L\nu}}). \tag{B.3}$$

Rearranging we obtain

$$E_l E_\nu = \frac{M_w^2}{2} + \vec{P_{Tl}} \cdot \vec{P_{T\nu}} + P_{Ll} P_{L\nu}. \tag{B.4}$$

Squaring and using the relation $E_\nu^2 = |\vec{P_\nu}|^2 = P_{T\nu}^2 + P_{L\nu}^2$ gives

$$E_l^2(P_{T\nu}^2+P_{L\nu}^2) = \left(\frac{M_w^2}{2} + \vec{P_{Tl}}\cdot\vec{P_{T\nu}}\right)^2 + 2\left(\frac{M_w^2}{2} + \vec{P_{Tl}}\cdot\vec{P_{T\nu}}\right)P_{Ll}P_{L\nu} + P_{Ll}^2P_{L\nu}^2. \quad \text{(B.5)}$$

Rearranging for $P_{L\nu}$ gives

$$\begin{aligned}(E_l^2 - P_{Ll}^2)P_{L\nu}^2 \quad &- \quad \left[2\left(\frac{M_w^2}{2} + \vec{P_{Tl}}\cdot\vec{P_{T\nu}}\right)P_{Ll}\right]P_{L\nu} \\ &+ \quad \left[E_l^2P_{T\nu}^2 - \left(\frac{M_w^2}{2} + \vec{P_{Tl}}\cdot\vec{P_{T\nu}}\right)^2\right] = 0. \qquad \text{(B.6)}\end{aligned}$$

The possible values of the z component of the neutrino momentum are obtained from

$$P_{L\nu} = \frac{-b \pm \sqrt{b^2 - 4ac}}{2a} \qquad \text{(B.7)}$$

where

$$\begin{aligned} a &= (E_l^2 - P_{Ll}^2) \\ b &= 2\left(\frac{M_w^2}{2} + \vec{P_{Tl}}\cdot\vec{P_{T\nu}}\right)P_{Ll} \\ c &= E_l^2P_{T\nu}^2 - \left(\frac{M_w^2}{2} + \vec{P_{Tl}}\cdot\vec{P_{T\nu}}\right)^2 \end{aligned} \qquad \text{(B.8)}$$

and the choice between the two possible solutions is made on the basis of which one gives the best top mass.

Appendix C

Angular Distributions of Top Decay Products

The purpose of this appendix is to justify the choice of angle used to probe the top polarization. Most of the calculations and arguments presented herein are taken from references [55, 56]. The derivation that follows uses the matrix element for top decay including all helicities to predict the angular distribution of the charged lepton from top decay. It also demonstrates the important factorization property of the angular distribution.

C.1 Derivation of Charged Lepton Angular Distribution

It will be shown that the decay product angular distribution for the $t \to W^+ b \to l^+ b$ decay can be written in terms of only two angles:

- θ_l : angle between the spin projection of the top along its direction of motion in the rest frame of the initial partons, and the direction of the charged lepton in the rest frame of the top quark;
- ψ_l^*: angle between the boost direction of the W in the top rest frame and the charged lepton in the W rest frame.

The "factorization property" of this angular distribution refers to the fact that the angular distribution may be written as:

$$F(\cos\theta_l, \cos\psi_l^*) = K \times g(\cos\psi_l^*) \times f(\cos\theta_l) \tag{C.1}$$

where $f(\cos\theta_l)$ and $g(\cos\psi_l^*)$ are independent functions of the two angles and K is a combination of constants.

In order to derive the angular distribution in this factorized form it is necessary to start with the spin-dependent matrix element:

$$\begin{aligned} M_{st,sb,sl,sv} &= i\left(\frac{-ig}{2\sqrt{2}}\right)|\mathrm{V_{tb}}|\overline{u}(b,s_b)\gamma^\mu(1-\gamma^5)u(t,s_t)\frac{i(g_{\mu\nu}-W_\mu W_\nu/M_W^2)}{W^2-M_W^2+i\Gamma_W M_W} \\ &\quad\times\left(\frac{-ig}{2\sqrt{2}}\right)\overline{u}(\nu,s_\nu)\gamma^\nu(1-\gamma^5)v(l,s_l) \end{aligned} \tag{C.2}$$

where the 4-momentum of each particle is specified by its symbol (eg. W = momentum of W) and the spin of each particle is represented by the 4-vector s with the particle symbol as a subscript. The numerator in the W propagator can be written as a sum over W helicity states:

$$\sum_\alpha \not{\epsilon}_\alpha^* \not{\epsilon}_\alpha = -(g_{\mu\nu} - W_\mu W_\nu/M_W^2), \tag{C.3}$$

where ϵ_α are the polarization vectors of the W and α spans the three helicity states of the W. $\not{\epsilon}_\alpha$ is a shorthand notation for $\gamma^\mu\epsilon_{\mu\alpha}$. The three polarization vectors are:

$$\begin{aligned} \epsilon_R^\mu &= \tfrac{1}{\sqrt{2}}(0,1,i,0) \qquad \epsilon_L^\mu = \tfrac{1}{\sqrt{2}}(0,1,-i,0) \\ \epsilon_S^\mu &= \tfrac{1}{M_W}(|p|,0,0,E) = (0,0,0,1) \end{aligned} \tag{C.4}$$

Where R,L and S refer to right, left and longitudinally polarized Ws. ϵ_S^μ may be simplified to (0,0,0,1) because it is evaluated in the W rest frame.

Rewriting C.2 using the explicit W helicity summation:

$$\begin{aligned} M_{st,sb,sl,sv} &= -\left(\frac{g^2}{8}\right)|\mathrm{V_{tb}}|\frac{1}{W^2-M_W^2+i\Gamma_W M_W}\times \\ &\quad\sum_\alpha \overline{u}(b,s_b)\gamma^\mu(1-\gamma^5)u(t,s_t)\not{\epsilon}_\alpha^*\not{\epsilon}_\alpha\overline{u}(\nu,s_\nu)\gamma^\nu(1-\gamma^5)v(l,s_l) \end{aligned} \tag{C.5}$$

If the spin of the top is fixed in an arbitrarily chosen z direction and the matrix element is squared and summed over the spins of the b, ν and l it gives:

$$|M|^2 \sim \sum_{\alpha,\beta} Tr[(\not{t} - m_t \not{s}_t)\not{\epsilon}_\beta \not{b} \not{\epsilon}^*_\alpha (1-\gamma^5)] Tr[\not{l}\not{\epsilon}^*_\beta \not{\nu} \not{\epsilon}_\alpha (1-\gamma^5)] \tag{C.6}$$

The summation over W helicity states present in Equation C.6 means that the cross-section for the top decay will receive contributions from several possible combinations of W helicity. The fact that α and β can be different provides the possibility of interference between W helicity states. Physically this occurs because each different W helicity state is represented by a Feynman diagram with the same final state. This causes the processes to interfere and contributions from interference terms must be taken into account [1]. To take into account all possible contributions to the cross-section, each helicity combination can be evaluated separately.

As an example, consider the case in which $\alpha = \beta = S$ and both helicities are longitudinal. The trace corresponding to the W decay part of the matrix element:

$$Tr[\not{l}\not{\epsilon}^*_S \not{\nu} \not{\epsilon}_S (1-\gamma^5)]$$

can be rewritten as

$$Tr[\not{l}\gamma^\mu \not{\nu} \gamma^\nu (1-\gamma^5)] \epsilon_{\mu S} \epsilon^*_{\nu S}. \tag{C.7}$$

Solving the trace and setting the masses equal to zero yields

$$[l^\mu \nu^\nu + l^\nu \nu^\mu - g^{\mu\nu} l \cdot \nu - i l_\phi \nu_\lambda \epsilon^{\phi\mu\lambda\nu}] \epsilon_{\mu S} \epsilon^*_{\nu S}. \tag{C.8}$$

Assuming $l^\mu = \frac{M_W}{2}(1, \sin\psi^*_l \cos\phi_l, \sin\psi^*_l \sin\phi^*_l, \cos\psi^*_l)$ and that ν^μ is back-to-back with l^μ in the W rest frame it can be seen that

$$l \cdot \nu = \frac{M_W^2}{2} \tag{C.9}$$

Computing the scalar products

$$l^\mu \cdot \epsilon_{\mu S} = -\frac{M_W}{2} \cos\psi^*_l = l^\nu \cdot \epsilon^*_{\nu S} \tag{C.10}$$

[1] When two diagrams do not interfere their amplitudes can be squared, then added to obtain the final squared matrix element. If they interfere the amplitudes must be added, then squared (eg. $(A+B)^2$) giving rise to cross-terms (or "interference" terms).

and

$$\nu^{\mu} \cdot \epsilon_{\mu S} = \frac{M_W}{2} \cos\psi_l^* = \nu^{\nu} \cdot \epsilon^*_{\nu S} \tag{C.11}$$

the trace becomes

$$-\frac{M_W^2}{2} \cos^2\psi_l^* - \frac{M_W^2}{2} \epsilon_S \cdot \epsilon_S - i l_{\phi} \nu_{\lambda} \epsilon^{\phi\mu\lambda\nu} \epsilon_{\mu S} \epsilon^*_{\nu S}. \tag{C.12}$$

Since $\epsilon_S \cdot \epsilon_S = -1$ the second term in this expression becomes $\frac{M_W^2}{2}$. The third term vanishes since the polarization vector components are only non-zero when $\mu = \nu$ and the anti-symmetric tensor $\epsilon^{\phi\mu\lambda\nu}$ is zero when any two indices are the same. This leads to a final expression for the SS helicity state:

$$\frac{M_W^2}{2}(1 - \cos^2\psi_l^*). \tag{C.13}$$

Similarly, terms can be calculated for all combinations of W helicities for both the top and the W decay. A complete listing of these terms is given below.

α	β	1st trace (top decay)	2nd trace (W decay)
S	S	$M_t E_b (\frac{M_t}{M_W})^2 (1 + \cos\theta_W)$	$\frac{M_W^2}{2}(1 - \cos^2\psi_l^*)$
L	L	$2 M_t E_b (1 - \cos\theta_W)$	$\frac{M_W^2}{4}(1 - \cos\psi_l^*)^2$
R	R	$\simeq 0$	$\frac{M_W^2}{4}(1 + \cos\psi_l^*)^2$
S	R	$\simeq 0$	$-\frac{e^{i\delta}}{\sqrt{2}}(\frac{M_W^2}{2}) \sin\psi_l^* (1 + \cos\psi_l^*) e^{-i\phi_l}$
S	L	$2i\frac{e^{i\delta}}{\sqrt{2}} M_t E_b (\frac{M_t}{M_W})(\sin\theta_W)$	$\frac{e^{-i\delta}}{\sqrt{2}}(\frac{M_W^2}{2}) \sin\psi_l^* (1 - \cos\psi_l^*) e^{i\phi_l}$
R	S	$\simeq 0$	$-\frac{e^{-i\delta}}{\sqrt{2}}(\frac{M_W^2}{2}) \sin\psi_l^* (1 + \cos\psi_l^*) e^{i\phi_l}$
L	S	$-2i\frac{e^{-i\delta}}{\sqrt{2}} M_t E_b (\frac{M_t}{M_W})(\sin\theta_W)$	$\frac{e^{i\delta}}{\sqrt{2}}(\frac{M_W^2}{2}) \sin\psi_l^* (1 - \cos\psi_l^*) e^{-i\phi_l}$
R	L	0	$-e^{-2i\delta}(\frac{M_W^2}{2}) \sin^2\psi_l^* e^{2i\phi_l}$
R	L	0	$-e^{2i\delta}(\frac{M_W^2}{2}) \sin^2\psi_l^* e^{-2i\phi_l}$

where, as previously mentioned, R,L and S refer to right, left and longitudinal polarization respectively, E_b is the energy of the b in the top rest frame, θ_W is the angle between the W momentum and the top spin in the top rest frame, ψ_l^* is the angle between the charged lepton and the W boost vector in the W rest frame, ϕ_l is the azimuthal angle of the charged lepton in the plane perpendicular to the W boost direction and δ is an arbitrary phase factor from the freedom to choose the azimuthal coordinates in the W rest frame.

When these terms are added together the expression for the charged lepton angular distribution is given by

$$\begin{aligned} F(\cos\theta_W, \cos\psi_l^*, \phi_l) &= 2M_t E_b (\frac{M_W}{2})^2 [\\ & (1-\cos\theta_W)(1-\cos\psi_l^*)^2 \\ & +(\frac{M_t}{M_W})^2 (1+\cos\theta_W)(1-\cos^2\psi_l^*) \\ & -2\frac{M_t}{M_W}\sin\theta_W \sin\psi_l^* (1-\cos\psi_l^*)\sin\phi_l] \end{aligned} \quad \text{(C.14)}$$

Converting all angles into their counterparts in the top rest frame (ie. $\psi_l^* \to \psi_l$) and using the vectors

$$\hat{s} = (0, -\sin\theta_W, \cos\theta_W) \quad \text{(C.15)}$$

$$\hat{l} = (\sin\psi_l\cos\phi_l, \sin\psi_l\sin\phi_l, \cos\psi_l) \quad \text{(C.16)}$$

allows Equation C.14 to be rewritten as

$$G(\cos\theta_W, \cos\psi_l, \phi_l) = \frac{M_W^4}{2}(x^2-1)\frac{8x^4}{(x^2+1)^2}\frac{1-\cos\psi_l}{(1-\beta_W\cos\psi_l)^2}(1+\hat{l}\cdot\hat{s}). \quad \text{(C.17)}$$

where $x = m_t/M_W$ and β_W is the relativistic velocity of the W in the top rest frame. Defining the angle θ_l as the angle between $\hat{\mathrm{l}}$ and $\hat{\mathrm{s}}$, this expression becomes

$$G(\cos\theta_l, \cos\psi_l) = \frac{M_W^4}{2}(x^2-1)\frac{8x^4}{(x^2+1)^2}\frac{1-\cos\psi_l}{(1-\beta_W\cos\psi_l)^2}(1+\cos\theta_l). \quad \text{(C.18)}$$

Therefore, the angular distribution can be written in terms of two independent functions. If the conversion is made from a function of $\cos\psi_l$ to $\cos\psi_l^*$ it can be shown that the distribution can be written as

$$F(\cos\theta_l, \cos\psi_l^*) = K \times g(\cos\psi_l^*) \times f(\cos\theta_l) \quad \text{(C.19)}$$

where

$$f(\cos\theta_l) = (1+\cos\theta_l). \quad \text{(C.20)}$$

This demonstrates that the angular distribution can be written in terms of functions of only two angles. For 100% polarized top quarks the angular distribution in θ_l is given by Equation C.20.

Title of Dissertation:

Performance of the ATLAS Hadronic Endcap and the Physics of Electroweak Top Quark Production at ATLAS

Author: _____

Dugan Clive O'Neil
November 30, 1999

VITA

Surname:	O'Neil	Given Names:	Dugan Clive
Place of Birth:	Newcastle, New Brunswick		
Date of Birth:	December 16, 1972		

Educational Institutions Attended:

University of New Brunswick	1990 to 1994
University of Alberta	1994 to 1996
University of Victoria	1996 to 1999

Degrees Awarded:

B.Sc. (Math-Physics) University of New Brunswick	1994
M.Sc. (Particle Physics) University of Alberta	1996

Honours and Awards:

Natural Sciences and Engineering Research Council Post-Graduate Scholarship	1997-1999
University President's Scholarship	1997-1999
R.M. Pearce Memorial Fellowship	1996-1997
University of Victoria Fellowship	1996-1997
University of Alberta Graduate Scholarship	1995-1996
Canada Science Scholarship	1990-1994
Tom and Parker Hickey Memorial Scholarship	1990-1994
Natural Sciences and Engineering Research Council Undergraduate Research Scholarship	1992,1993